Doctor's Thesis

Numerical and Experimental Analysis on the Water Harvester using Peltier Effect

Supervisor: Professor. Jung, Hyung Ho

August 2019

Department of Mechanical Engineering
Graduate School of Korea Maritime
and Ocean University

ANWUR ALENEZI

Numerical and Experimental Analysis
on the Water Harvester using Peltier Effect

by Anwur H A F Alenezi

A dissertation submitted to

the Graduate School of Korea Maritime & Ocean University

in partial fulfillment of the requirements for the degree of

Doctor of Mechanical Engineering
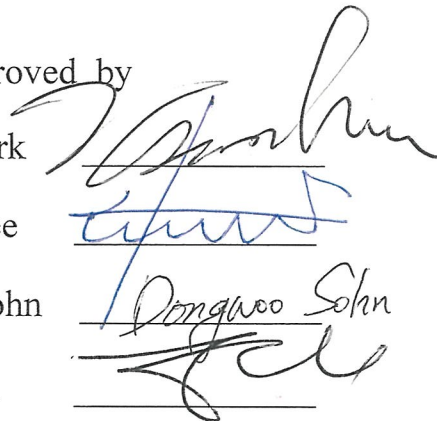
Written under the supervision of

Ph.D.,Hyung Ho Jung

and approved by

Ph.D.,Kweon Ha Park

Ph.D.,Young Ho Lee

Ph.D.,Dong Woo Sohn

Ph.D.,Jin Seok Oh

31, May 2019

Department of Mechanical Engineering

Graduate School of Korea Maritime & Ocean University

Table of Content

List of Figures

List of Tables

Numerical and Experimental Analysis on the Water Harvester using Peltier Effect

ANWUR ALENEZI

Department of Mechanical Engineering

Graduate School of Korea Maritime and Ocean University

Abstract

Condensation of water vapor from humid air is a promising technique to produce water for drinking, cleaning, and other purposes. Several techniques can be used to cool hot and humid air and obtain water from it. For this purpose, Water Harvester is proposed in this study. The process of humid air condensation in this study depends on the performance of experimental and numerical analyses of the fluid flow and condensation performance.

The experimental was performed in different operation conditions of working time, air temperature, and relative humidity. The condensation starts and sustains as the surface temperature maintains less than the dew-point temperature. As the relative humidity (RH) of air increased, the amount of condensed water also increased. There is a proportional relation between the condensation rates and the temperature difference. There is also a proportional relation between the cooling surface and air temperatures. It was found that the amount of heat rejected by the system increased as the condensation rate increased. As more heat was rejected, more water vapor was cooled and converted to water.

Numerical predictions of the mass fraction of water and air on the cooling surface and condensation rate were performed. Before conducting these analyses, a 3D model of a condensation system to obtain water vapor from humid air through a

thermoelectric cooler was built using SolidWorks software and then tested with ANSYS software. The obtained results of numerical analyses showed that the maximum value of the water fraction over the surface was measured as 98.7%, which indicates that 98.7% of the surface was wet. However, the maximum mass fraction of air was measured as only 1.4%. The Sherwood and Reynolds numbers are linearly related; as one increases, so does the other. Good agreement among the two analytical methods was observed during a comparison. Moreover, there was also good agreement between these results and those found in a literature review.

Key words: Water Harvester, Experimental Analyses, Numerical Analyses, Condensation, Computational Fluid Dynamics

Nomenclature

$C_{A,\infty}$	Flow molar concentration (kmol/m^3)
CA	Molar concentration
$C_{A,s}$	Surface molar concentration (kmol/m^3)
c_p	Specific heat at constant pressure
D_{AB}	Binary mass diffusivity, m^2/s
E	Energy
g	Gravity
Gr	Grashof number
$\overline{h}$	Average convection heat-transfer coefficient
h_{tot}	Total enthalpy
k-ε	Convective diffusion, production (by deformation and viscous shear), and dissipation (model)
K	Thermal conductivity
m	Mass flow rate
$\overline{Nu}$	Average Nusselt number
Nu	Nusselt number
Nu$_F$	Nusselt number of pure forced convection
Nu$_N$	Nusselt number for natural (free) convection

P_{kb}, $P_{\varepsilon b}$	Buoyancy forces
P	Pressure
Pr	Prandtl number
P_s	Saturation pressure
q/s	Humidity/salinity
R	Gas constant
Re	Reynolds number
RH%	Relative humidity
$\overline{Sh}$	Average Sherwood number
Sh	Sherwood number
Sc	Schmidt number
T	Temperature
U	Internal energy
u	Velocity on x axis
v	Velocity on y axis
w	Velocity on z axis
ρ	Density
τ_x	Shear stress
α	Thermal diffusivity
β	Volumetric thermal expansion coefficient

Abbreviations

CAD	Computer-aided Design
CFD	Computational Fluid Dynamics
CAM	Crassulacean Acid Metabolism
COP	Coefficient of Performance
DEH	Dehumidification
TEC	Thermoelectric Cooler
ICEM	ANSYS ICEM CFD
TFWG	Thermoelectric Freshwater Generator
WHO	World Health Organization

Chapter 1 . Introduction

1.1   Background

In nature, a shortage of water is not a new problem. Impure drinking water is hazardous to human health. Various studies have shown that every eight seconds, a child dies because of diseases caused by unsafe water, and that every year, approximately five million or more people die from illnesses associated with dangerous drinking water or insufficient sanitation. The water filters utilized in homes cannot eliminate all heavy metals, bacteria, viruses, and parasites from water. These factors initiate a requirement for techniques appropriate to arid regions, particularly those located in remote areas of developing countries, to generate clean and safe potable drinking water in addition to conserving both water and energy (Shanmugam et al., 2004). Lack of drinking water sources is a continual, severe, and common problem in the regions of Central and Southern Asia, the Middle East, and northern Africa. Several studies indicated that this problem can be solved by applying one or more of the following methods such as Freshwater transportation from additional sites via water trucks or infrastructure, Desalination of saltwater and Water extraction from atmospheric air (Parekh et al., 2004).

The first method of water transportation is not favorable because the process of transportation is very expensive. However, the second method, desalination, relies on the availability of saline water resources in arid areas, which is often rare. This method also requires electric power to create high pressure to force the water component of seawater to flow through a membrane. A large amount of energy is consumed by the first two methods, and they require highly skilled operation. However, to date, the first two methods are the key practical methods of seawater desalination in various regions in the world. Because these two methods depend on fossil-fuel energy consumption, they result in CO_2 emissions, which are harmful to environment. Furthermore, there are several sites where the energy to operate the

desalination process is very expensive. These disadvantages have encouraged researchers to concentrate on the third method: water extraction from air (Wang and Li, 2007).

Atmospheric air is naturally available in huge amounts and is considered a renewable and endless water reservoir that is obtainable everywhere on the earth's surface. Water extraction from air has many benefits when compared to the first two methods, as air is a clean and renewable water source. The total amount of water available in the air is measured at 14,000 km^3, whereas the amount of freshwater available on the earth is just 1200 km^3 (El-Ghonemy, 2012b). Water extraction from air can be performed by applying various methods, the majority of which depend on cooling moist air until it reaches a temperature below the dew point. Then, the water vapor is absorbed from the moist air by utilizing a liquid or solid desiccant, followed by water recovery through desiccant heating and evaporated water condensation. The selection of a suitable method technique for water extraction from air is considered an engineering decision that depends on different factors such as local climatic conditions in addition to other economic factors including energy, operating, and capital costs. The available devices for water extraction differ in their scale and amount of produced potable water.

1.2   Atmospheric air

A significant amount of atmospheric air is spread over the earth, and this air is a renewable freshwater source. Air primarily contains 78% nitrogen and 21% oxygen in addition to various quantities of water in gas form. This variation is based on the air pressure and temperature. The overall amount of water in the atmosphere can be evaluated from its partial pressure (P) within the air mass. At a defined pressure (P) and temperature (T), the partial pressure cannot become higher than a defined level without the occurrence of condensation. This level is defined as the saturation pressure (P$_s$). Therefore, the relative humidity (RH) of air is the ratio of the partial pressures [RH$^{1/4}$ × (P/P$_s$)]. As the air pressure or temperature increases, the saturation

pressure increases in addition to an increase in the water mass capacity of 1 m^3 of air (Beysens and Milimouk, 2000).

At a defined RH and temperature of air, the psychrometric diagram that describes the amount of water in air in terms of the mass fraction at various RH and temperatures permits the saturation point of the water in air to be ascertained. This is defined as the dew point, the temperature at which water vapor condenses. One example is that at an air temperature of 20 °C and RH of 80%, the dew temperature is measured as 18 °C, which decreases to 10 °C when the RH is just 25%. The condensation of water takes place in the form of droplets, showing partial wetting of the substrate by liquid water (El-Ghonemy, 2012a).

1.3   Climate Analysis

A major factor that must be considered when extracting water from air is the climate of the region in which the extraction will be made. The content of water in air can be measured by means of main three parameters: RH, air temperature, and overall atmospheric pressure. Given that the atmospheric pressure is 101,325 Pa, different values of relative humidity (RH), moisture content, and temperature are illustrated in figure 1.1 (Magrini et al., 2017).
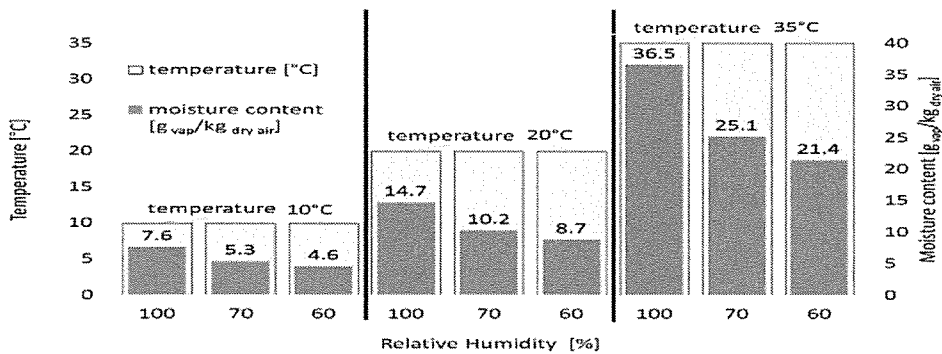
Figure 1.1: Existing relations between air content parameters (Magrini et al., 2017)

3

It is significant to note that recovering water from air requires less energy at a high hygrometric degree. This can be simply ascertained from a psychrometric chart like that presented in Figure 1.2. When the saturation temperature of air increases, a higher slope of the saturation curve is observed, which means that a low specific energy is needed for water extraction. Two values of specific enthalpy difference Δh are presented for the same water extraction, represented by similar values of hygrometric degree difference Δx in two different saturation conditions where the dew point in the first condition is 20 °C and that in the second condition is 10 °C (Magrini et al., 2017).
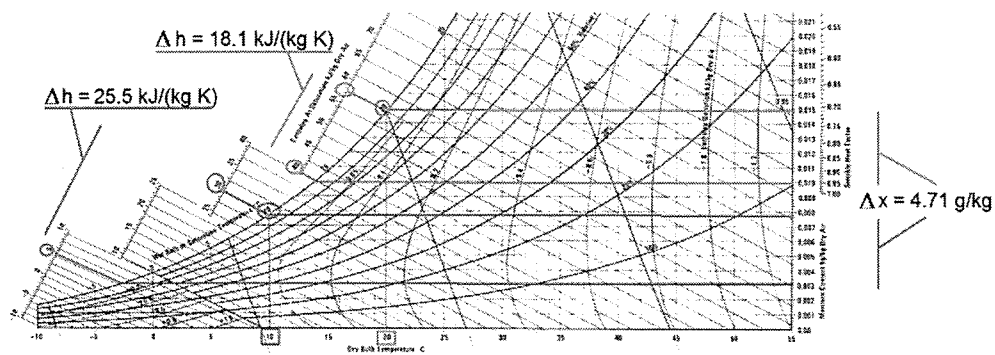
Figure 1.2: Variations in specific enthalpy corresponding to same Δx (Magrini et al., 2017)

Humid and hot regions are considered to be the most appropriate climates in which to apply the water extraction process. In such regions, the air is defined by a state adjacent to the saturation curve and by considerable vapor content.

1.4   Research Importance

All around the world, freshwater has become increasingly inadequate and polluted. It is also increasingly consumed as the population grows, which results in a reduction in conventional sources. Climate change has had a considerable effect on the complex water issue as well. To solve the problem of freshwater shortage, unconventional

sources have been investigated and implemented, including seawater desalination and water extraction from air. This study clearly illustrates the problems associated with seawater desalination and the advantages of using methods of water extraction from air.

The problem of freshwater shortage is usually linked to the problem of shortages in electrical energy. However, this situation is usually not covered in research studies. In this study, a Water Harvester device is proposed for water extraction by directly condensing water vapor from the air. The proposed device uses a Thermoelectric Cooler (TEC) to solve the problem of electrical energy shortage. The TEC is based on conventional systems that use compressors as heat pumps. The TEC can be switched on for short time, or it can be operated using a Peltier module as a heat pump and can continuously run at the optimum current.

A thermoelectric module is defined as solid-state technology that is utilized to primarily transfer heat through the utilization of dissimilar semiconductor materials. The TEC is mainly a heat pump. As energy is absorbed by the electrons when they pass from one semiconductor to another, the cold junction becomes cold. The involved heat sink in the system discharges the accumulated heat energy from the system, while the main function of the DC power source is to pump the electrons from one semiconductor to another. The thermoelectric module and its heat sink can be utilized to dehumidify the humid air.

The main purpose of this study is to build a prototype of a water harvester device from air using a Thermoelectric Cooler, and to evaluate the amount of water produced from this device by using experimental and numerical methods as follows:

Experimental method: In this method, an experimental equipment will be used to evaluate the amount of water produced by the proposed device.

Numerical method: In this method, CAD modeling software will be used to build a model of the proposed system under the specified conditions, and CFD analysis software will be used to solve this system in terms of measuring the amount of water vapor transferred to the device and converted to water owing to condensation.

1.5   Aims and objectives

The main aim of this study is to model the condensation process of water vapor in air using a device that uses a TEC. The amount of water produced by this device will be estimated using experimental analysis and numerical analysis. To achieve this aim, the following objectives will be accomplished:

- Collect a comprehensive literature review focusing on the utilized techniques of water extraction from air, modeling of the condensation process, and gap analyses.
- Build a prototype of a Water Harvester device with a TEC using CAD modeling software and analyzed it numerically to evaluate the amount of water produced by the proposed device.
- Experimentally measure the amount of water produced by the proposed device.
- Record the results from the two analytical methods and compare them.
- Discuss the results and reach a suitable conclusion.

1.6   Research outline

This study is divided into six different chapters. The content of each chapter is as follows:

- Chapter 1 provides a general introduction to the study idea, and it presents the study importance, aims, and objectives.
- Chapter 2 provides a review of previous work on the used techniques and methods of water extraction from air. This chapter also reviews the numerical and experimental modeling of the condensation process.

- Chapter 3 provides the methodology used to achieve the study aim of evaluating the amount of water produced by the Water Harvester device with a TEC via numerical and experimental methods.
- Chapter 4 provides the results obtained from the experimental methods.
- Chapter 5 provides the procedure for the numerical analysis and its results.
- Chapter 6 provides conclusions for the study and suggested recommendations for future work.

Chapter 2 . Literature Review

2.1 Techniques for water extraction from air

There are various techniques for water extraction from humid air that are based on surface cooling to a temperature lower than the dew point of air, inducing convection, or by utilizing desiccants. Some inventions in the field of water extraction from air use hygroscopic desiccants and adsorbent materials, which are useful in climates with low humidity. One of the initial works of water extraction from air was conducted in Russia (Hamed et al., 2011), in which a special device was utilized. The device is a system of inclined, vertical and channels in the earth to be used for water collection from air by cooling moist air until it reaches a temperature below its dew point. This device is called an earth-water collector.

Kobayashi (1996) used such device to collect water from air in Figure 2.1. The earth is treated as having three layers. As the sun shines and the surface becomes dry, a dry layer is generated whose depth changes depending on the soil type, capillary layer depth, and rainfall amount. Below the dry layer, a moist layer is found, which still wet by capillary action as it is in contact with the underground water. As the surface of the earth is heated by the sun, the water that reaches the surface by capillary action dissipates as aqueous vapor. After that, an earth-water collector is used to collect this vapor as water droplets as the evaporated water vapor condenses on the glazing.
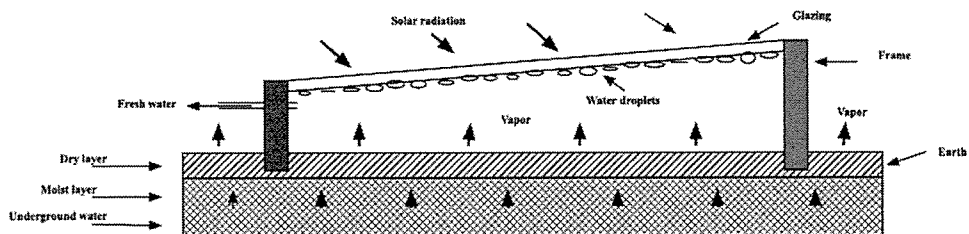
Figure 2.1: Principle of earth-water collector (Kobayashi, 1997)

Figure 2.2 is a flow diagram of the majority of water extraction techniques from air that are based on solar energy. Two main methods are described that use solar energy.
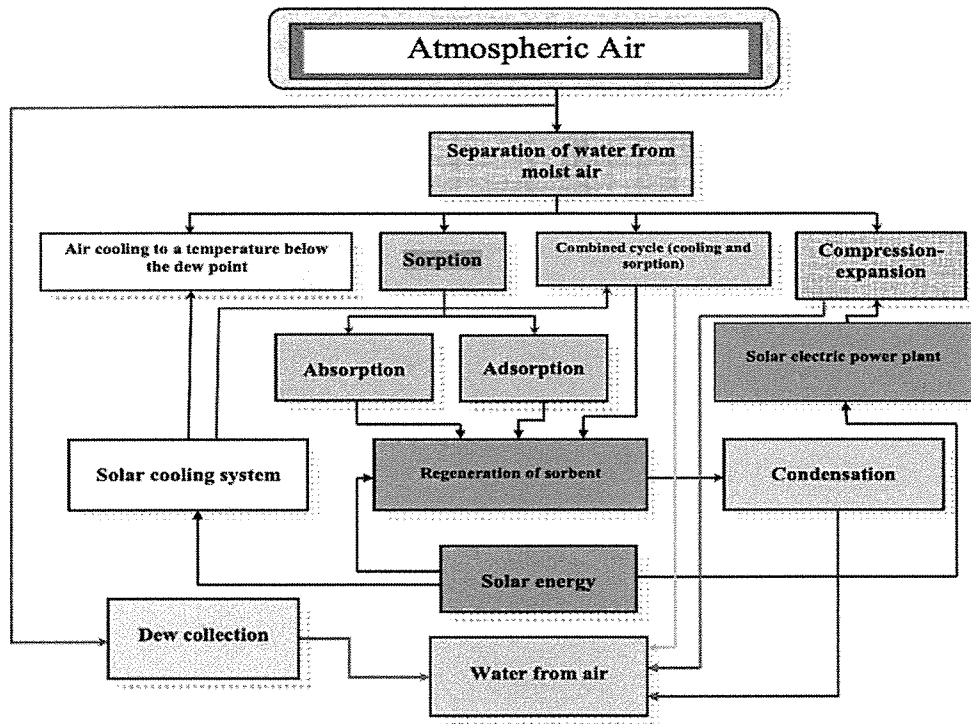
Figure 2.2: Flow diagram of water separation from air based on solar energy (El-Sharkawy, 2000)

2.2   Water vapor condensation

Naturally, humid indoor air can result in the condensation of water droplets on windows of buildings or the appearance of moisture stains on furniture, ceilings, and walls. When the air humidity is very high, this results in the growth of mold; whereas, when the humidity is very low, static electricity and electronic apparatus malfunctions are the key difficulties that may occur. The occurrence of condensation depends on the psychrometric conditions of humidity and temperature in addition to airflows. As

a result, clear and comprehensive moisture-heat-airflow models are needed (Teodosiu et al., 2015).

Joshi et al. (2017) designed a thermoelectric freshwater generator (TFWG) and experimentally tested it. The model depends on the thermoelectric cooling effect through moisture condensation from ambient moist air. Such a model is suitable for people living in humid and coastal regions where the RH is greater than 60%. A generator prototype was built with a 0.7-m-long cooling channel and 10 thermoelectric modules of 0.04×0.04 m^2 in size. Each of the thermoelectric moduli are positioned linearly in an array. At the cold side of the modulus, an internal heat sink is mounted with a surface area of 0.2 m^2 and length of 0.65 m. This heat sink improves the heat transfer rate. The experimental results indicated that with the utilization of an internal heat sink, the amount of water produced per 10 h increased by 81% compared to the situation with no heat sink. Throughout the analyses, the RH, air mass flow rate, and electric current were varied to investigate their effects on the amount of generated water. According to the results, the amount of generated water was directly proportional to the three factors. Figure 2.3 shows the computer-aided prototype of the proposed system and the actual model of the system.
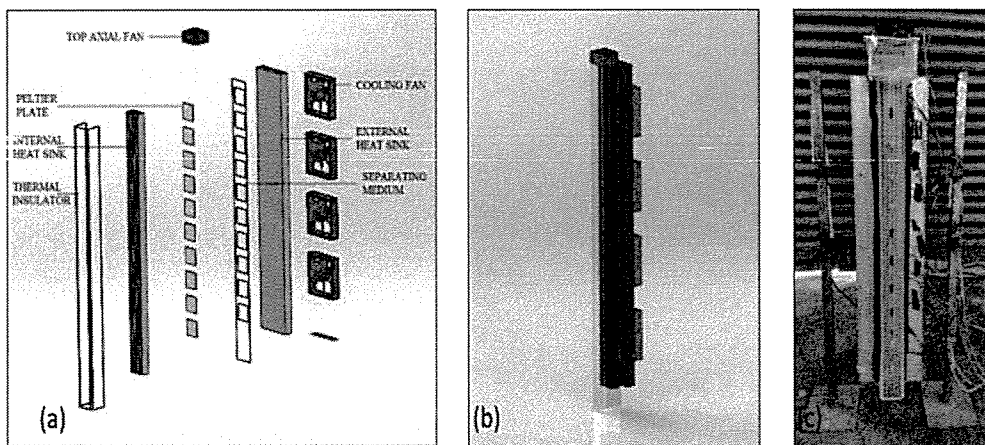
Figure 2.3: Model of proposed system (Joshi et al., 2017)

The entrance of the moist air is at the top end of the system because of the suction produced by the axial fan. Next, the air began to flow through the thermoelectric cooling channel wherein heat is being absorbed from the moist air by the Peltier modules (powered via electrical energy) at the cold side. Thus, the air starts cooling, its temperature reaches the dew point while flowing through the channel, and condensation begins. Finally, the air exits from the bottom of the channel. The water is condensed over the internal heat sink (cold) and starts to flow downward owing to gravity. It is then collected at the bottom of the channel.

The obtained results are presented in Figure 2.4 in terms of changes in the amount of water condense as the current changed, the amount of water condense as the RH changed, and the amount of water condense as the mass flow rate changed. It is clear that the amount of generated water by the system increased as the air mass flow rate increased. This occurred because the water content in the channel increased, which then increased the amount of condensed water. The water condense was directly proportional to the humidity of the moist air because the amount of water vapor in the same mass of air increased. Finally, the amount of water produced by the system increased as the electric current increased owing to the increase in the absorbed heat by the Peltier modules. When no heat sink was used in the system, the maximum amount of water produced by the system was 45 mL. However, adding a heat sink in contact with the cold side of the Peltier modules increased the amount of water to 240 mL. This increase in the amount of water resulted from an increase in the flowing air turbulence as well as an increase in the surface area for convection heat transfer on the module's cold side and the moist air. The observed maximum value of COP was 0.437 when the RH was 90% and the air mass flow rate was 0.011 kg/s.
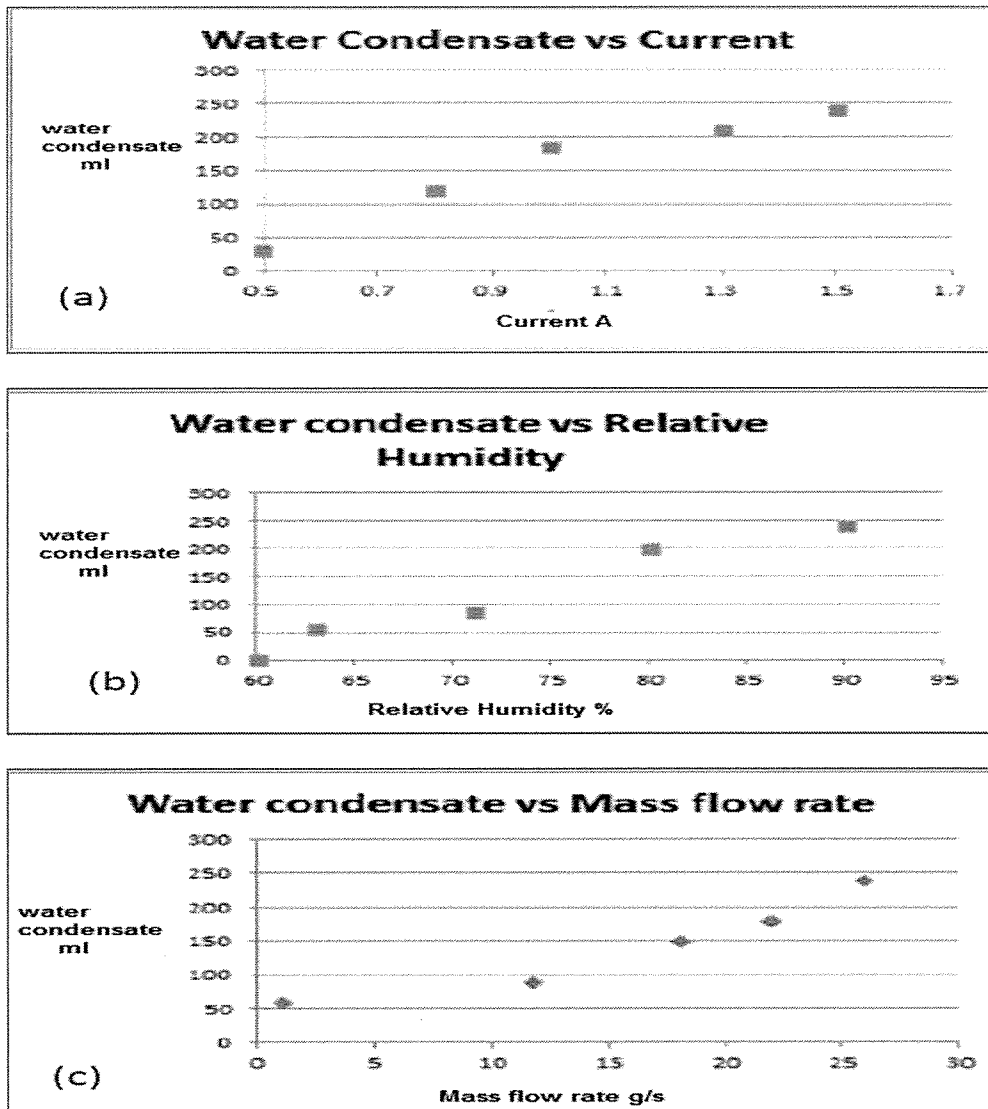
Figure 2.4: Effects of varying current, RH, and mass flow rate of air on amount of condense water (Joshi et al., 2017)

Liu et al. (2017) designed a portable water generator of 7 kg in weight with two TECs. This design was experimentally tested under different boundary conditions. The effects of varying the air flow rates and the inlet air RH on the condensation rate and amount of produced water were experimentally investigated. The designed system is presented in Figure 2.5.

12
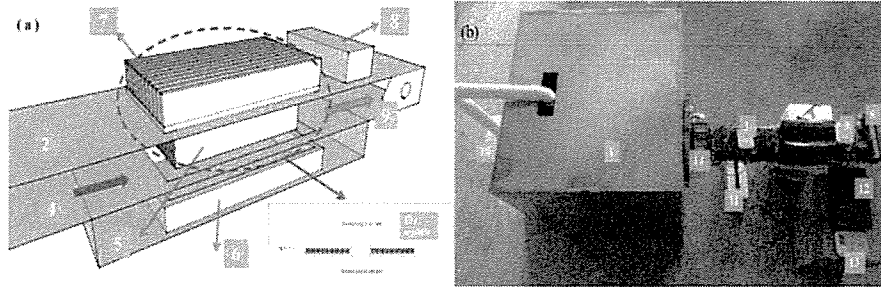
(a) The schematic of water generator (b) The photo of experimental rig. 1-Mixing chamber; 2-Inlet channel; 3- Hygrothermogrophs; 4-Inlet; 5-Thermal slug on the cold side of TECs; 6-Water pan; 7-Thermal slug on the hot side of TECs; 8-Cooling fan; 9-Outlet; 10-Humidifier; 11-DC power; 12-Data acquisition instrument; 13-Electric balance; 14-Anemometer.

Figure 2.5: Designed water generator (Liu et al., 2017)

The utilized system in the experimental work is composed of a mixing chamber, humidifier, TE water generator, and air channel. The data from the condensation experiments are recorded in Table 2.1.

Table 2.1: Condensation experiment data (Liu et al., 2017)

Exp.	Flow rate (m^3/h)	RH (%)	T (°C)	Water (g/h)	Condensation rate η (%)	Water (kg/kWh·m^2)
1	29.7	67.8	24.3	11.2	2.42	0.889
2	29.7	77.7	23.1	15.2	3.08	1.207
3	29.7	84.7	24.2	22.3	3.87	1.771
4	29.7	92.7	23.6	25.1	4.10	1.993
5	29.7	86.8	21.9	18.2	3.56	1.445
6	50.4	86.5	22.1	18.7	2.13	1.485
7	70.6	86.5	21.2	20.6	1.76	1.636

The results showed that both the condensation rate and amount of produced water increased as the RH increased. In addition, those increasing as the air flow rate increased; whereas, the condensation rate decreased as the flow rate increased. The maximum amount of produced water by the system was 25.1 g/h on a condensation surface of 0.216 m^2 with an input power of 58.2 W.

Figure 2.6 clearly shows the obtained results of changing the RH on the amount of condensed water, water produced, inlet moisture content, and generation rate, in addition to a temperature reference.
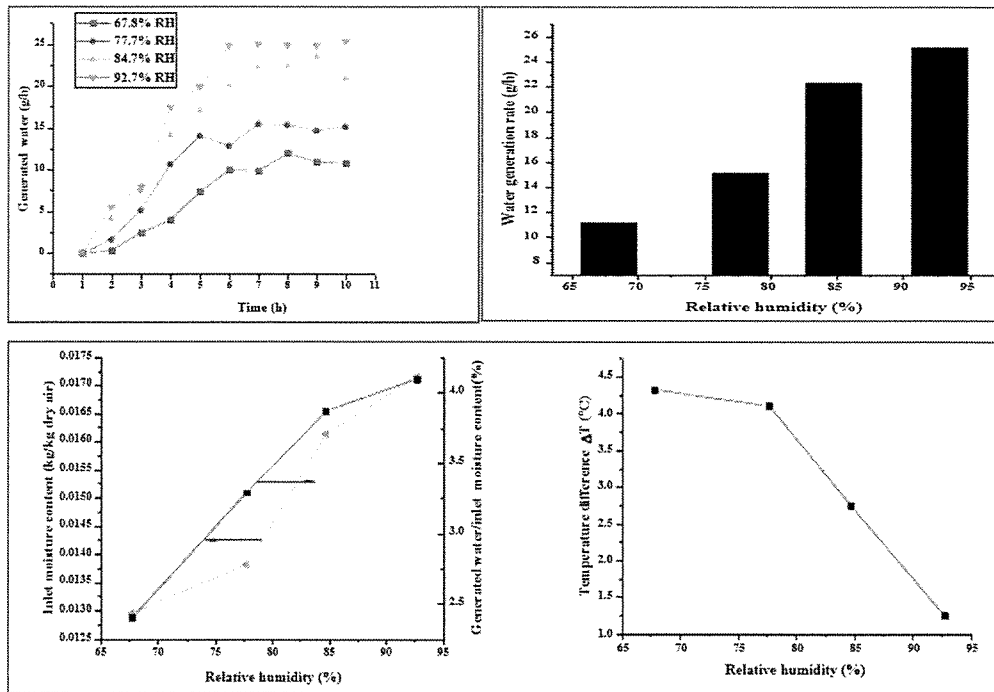
Figure 2.6: Impact of RH (Liu et al., 2017)

Figure 2.7 shows the effects of changing the flow rate on the amount of generated water, temperature at the cold-side fin, condensation rate, and temperature difference. The amount of condensed water was initially 29.6 m^3/h, which was more than that at air flows of 50.4 and 70.6 m^3/h. The lower generation of water at a high flow rate results from the high temperature of the fins at these rates.

14
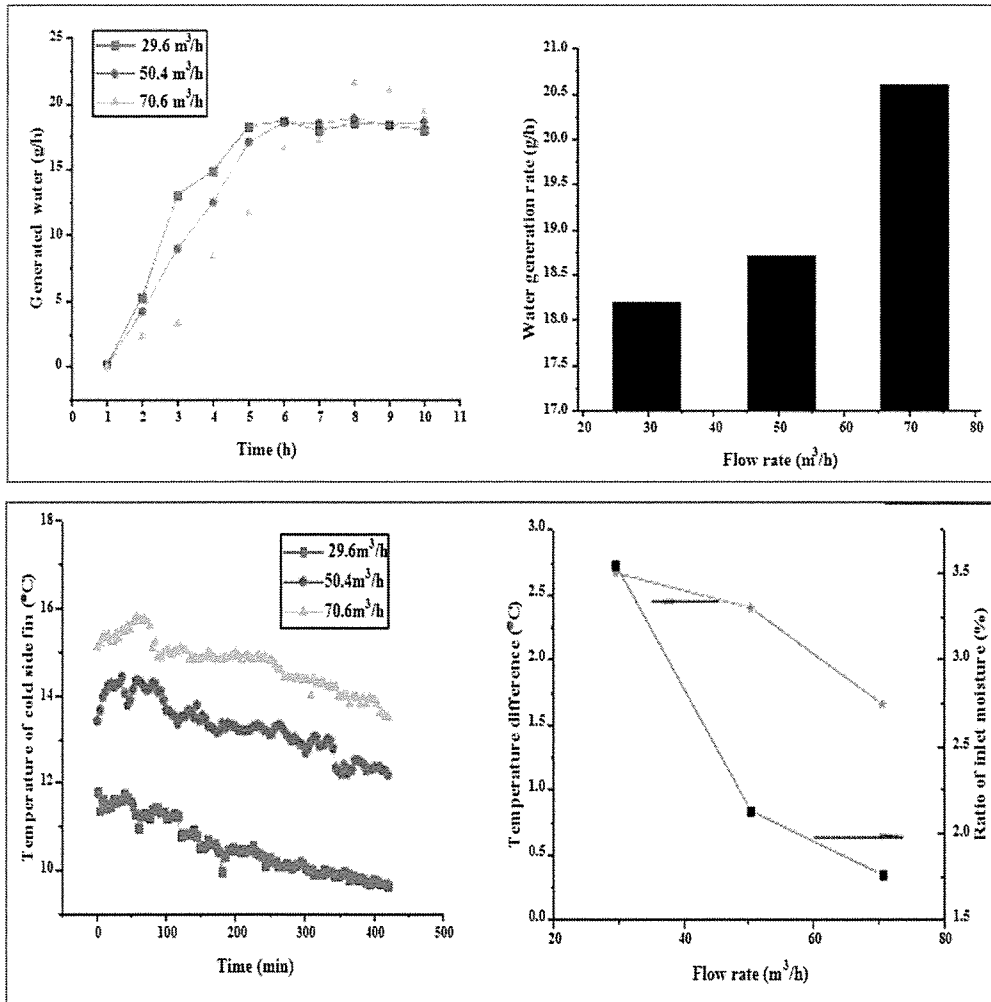
Figure 2.7: Impact of air flow rate (Liu et al., 2017)

Liu et al. (2017) also analyzed the performance of condensation in the system by performing a comparison of the performance of various TE water generators, as shown in Table 2.2. It is clear that the designed system in this work operated efficiently at a low RH and less energy consumption.

Table 2.2: Comparison of performance of various TEC water generators (Liu et al., 2017)

TEC used	Inlet air parameters			System performance		
	T (°C)	RH (%)	Flow rate (m³/h)	TEC consumed power (W)	Water (g/h)	Rate (%)
2*	24.29	67.8	29.7	52.3	11.2	2.42
2[7]	25.3	60	129.1	65.5	27.9	1.78
3[16]	27	82	13.68	100	40.3	13.62
10[8]	30	65	80.3	135.0	5.0	0.31
20[1]	32	39.5	57	1000	597.4	76.2

A long or U-shaped channel resulted in an increase in the condensation rate, whereas a small capacity, single-pass structure, and small condensation surface resulted in a low condensation capacity. The system in this study is small in size and can efficiently operate at low air flow rates, which makes it appropriate for outdoor applications. This research is considered a guide for the design and improvement of a highly efficient potable water generator. Liu et al. (2017) and Colburn and Hougen (1934) developed a condensation mass-transfer theory that was managed by the mass concentration gradient through the noncondensable layer. They additionally illustrated the heat-transfer process as the summation of latent heat and sensible heat flows. Heat and mass transfer modeling in a vertical tube condenser from steam and a noncondensable gas mixture was theoretically derived by Dehbi and Guentay (1990). A set of algebraic equations was derived for the film thickness. Both the heat and mass transfer similarities were invoked to deduce the condensation rate.

Another theory was developed by Munoz-cobo et al. (1999) for turbulent vapor condensation in vertical tubes with the existence of noncondensable gases. In this theory, the thickness of the condense film thickness was evaluated by utilizing an approximate method. The method followed by Colburn and Hougen (1934) was utilized by Che, Da, and Zhuang (2002) for an analysis of the mass and heat-transfer process related to the condensation of water vapor from moist air in a tube. The

analyses were conducted experimentally, and the obtained results showed that the convection-condensation heat transfer coefficient was 1.5–2 times greater than that obtained by forced convection without condensation. Winkler et al. (2006) conducted experimental work to determine the mass and thermal accommodation coefficients of m and t for water vapor condensation in air for a temperature range of 250 to 290 K. The two coefficients were first determined simultaneously and directly. After this determination, water droplets were observed in air at various total gas pressures in the range of 1000 down to 100 hPa. The condensation nuclei were selected as monodispersed seed particles with a diameter of 9 nm. Next, water vapor with a defined partial vapor pressure was added. Then, supersaturation was obtained via adiabatic expansion in an expansion chamber.

The majority of experiments conducted and documented in this paper were conducted at vapor saturation ratios in the range 1.30–1.50. A diffusion humidifier was implemented in this study for humidification. At a saturation ratio of 1.02, only one experiment was conducted. This experiment resembled the circumstances noticed in the earth's lower atmosphere. Within the experimental work, monodispersed DEHS particles with a diameter of 80 nm were utilized as condensation nuclei. The quantitative evaporation of a liquid jet was used to generate water vapor. The growth of water droplets was controlled utilizing a CAM method. The obtained results showed that the coefficient of thermal accommodation (t) was higher than 0.85 across the entire considered temperature range. For a temperature range of 250–270 K, the values of coefficient m were found to be lower than 0.8, while for higher temperatures up to 290 K, the obtained values of m were less than 0.4. The two coefficients are likely to be unity for the overall examined conditions. The obtained results from this research allows for the accurate prediction of the formation and growth of cloud droplets needed to parameterize cloud light scattering/absorption and precipitation properties in climate models. Some of these results are presented in Figures 2.8, 2.9, 2.10.
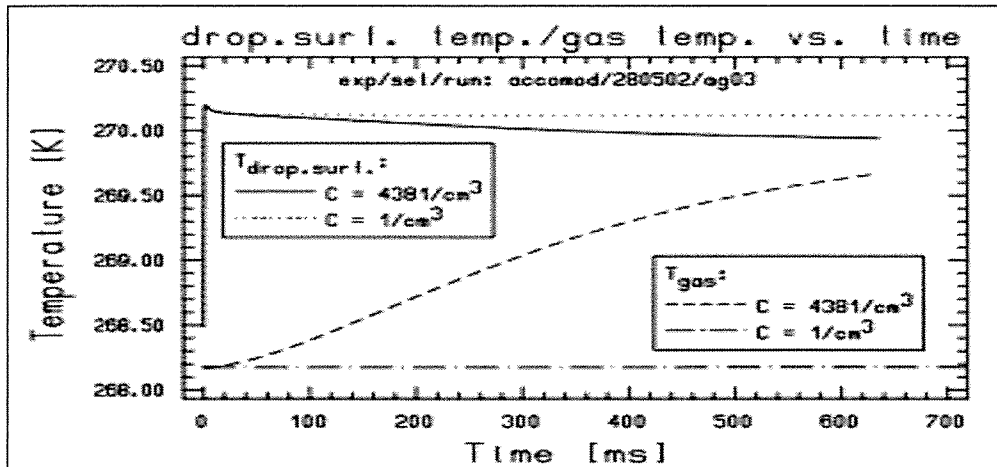
Figure 2.8: Results of gas temperature and droplet temperature throughout condensational growth in droplet populations (Winkler et al., 2006)
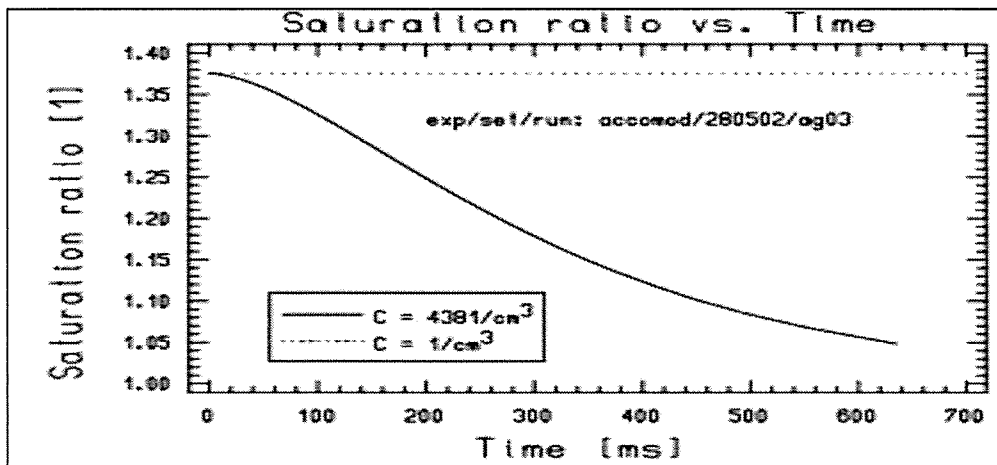
Figure 2.9: Results of saturation ratio throughout condensational growth in droplet populations (Winkler et al., 2006)
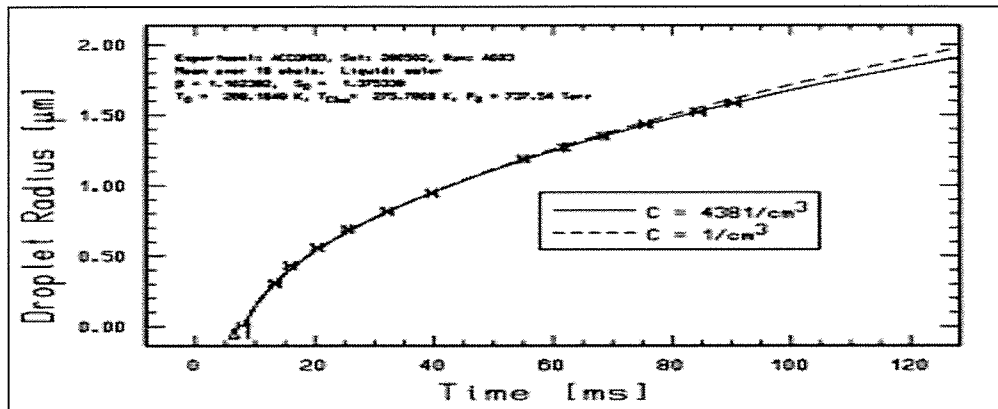
Figure 2.10: Droplet growth curves evaluated for condensational growth in droplet

populations (Winkler et al., 2006)

In a study by Saraireh et al. (2010), a mathematical model for heat and mass transfer leading to water vapor condensation in the presence of noncondensable gases was developed and tested to determine the heat flux, condensation rate, and outlet water temperature. The results were compared with experimental results from other studies and are presented in Figures 2.11, 2.12.
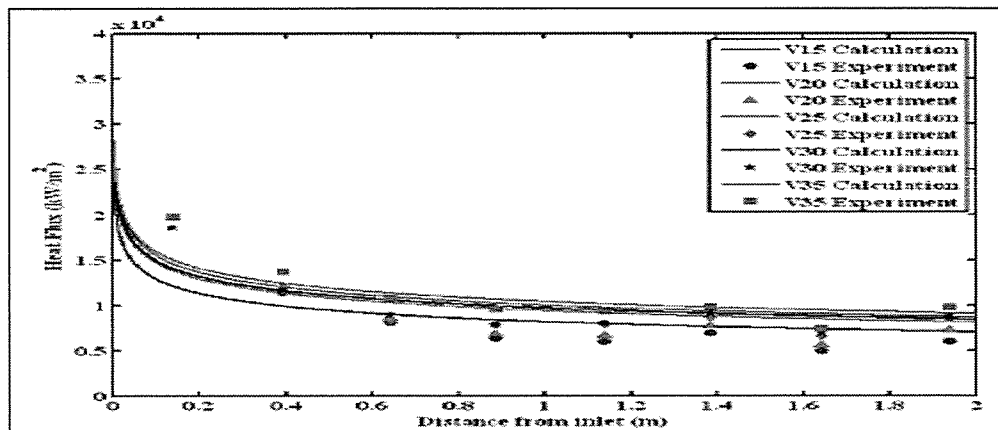
Figure 2.11: Predicted results of heat flux and experimental results of Ambrosini

(2008)

19
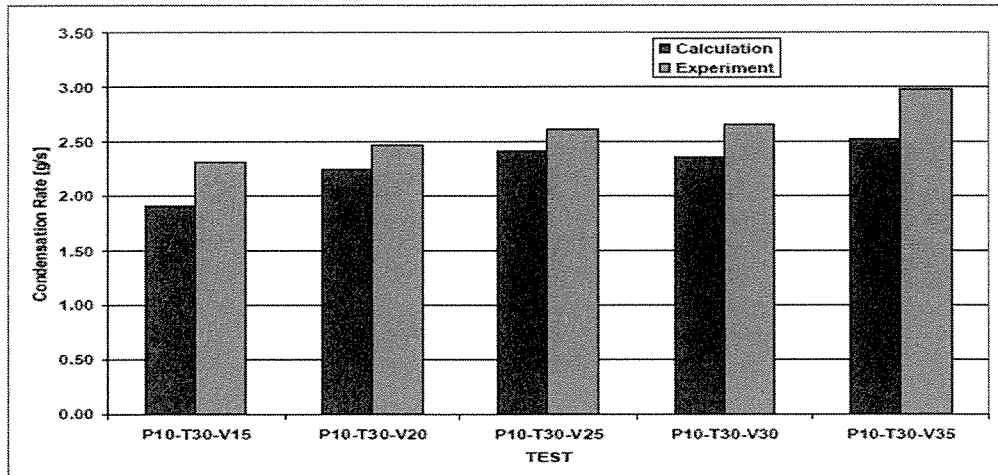
Figure 2.12: Predicted and experimental results of condensation rate by Ambrosini (2008)

2.3   Modelling of water vapor condensation

The modeling of water vapor condensation depends on some essential simplifying hypotheses, such as:

- The humid air should be an ideal gas that is perfectly made of two perfect gases of water vapor and dry air.

- It must be ensured that no chemical reaction can occur between these two gases.

- It should be required that the binary mixture is an incompressible Newtonian fluid.

- It should be required that the heat and mass transfer interactions are negligible.

- It should be required that the surface on which condensation will occur is impermeable with regard to the absorption-desorption phenomena.

- Usually, the amount of condensed vapor is low, and the quantity of condense is eliminated from the computational domain.

20

The main parameter affecting the surface condensation is the temperature of the surface. For precise prediction of the surface condensation and its growth, it is essential to perform an accurate calculation of the surface temperature in terms of the value and distribution. However, a precise approach to measure the surface temperature must consider the sensible heat transfer (conduction, convection, and radiation) in addition to the surface latent heat transfer. By taking into account the convection heat transfer of the surface as well as the water vapor transport, the suggested model depends on methodology proposed by the International Energy Agency (Condensation and Energy, 1991), in which the water vapor transport in air is performed by convective movements.

A numerical model was developed by Teodosiu et al. (2015) for the condensation of humid air inside a room. The developed model concentrated on the surface convection heat transfer and water vapor transport. It was simulated using a CFD technique. The obtained results showed that the overall numerical CFD model could be utilized for airborne moisture prediction in a room when considering humid air condensation on cold surfaces. Experimental data related to water vapor condensation were used to analyze the performance of the numerical model on a glazed wall in a ventilated test room. By comparing the numerical and experimental results, it was clear that the model can estimate the condense appearance in addition to its distribution on cold surfaces. The obtained results from the numerical analyses prove that the condense distribution in terms of the liquid mass occurs on the inner surface of the glazed wall. Two supply-air moisture content values were examined:

- Case 1: 10.2 g/kg;
- Case 2: 13.1 g/kg.

The specific humidity of extracted air in case 1 is presented in Table 2.3.

Table 2.3: Specific humidity of extracted air (Teodosiu et al., 2015)

Experimental (g/kg)	Numerical (g/kg)	Relative error experimental-numerical (%)
10.66	10.83	1.6

The researchers found that a small deviation of 1.6% was found between the numerical and theoretically measured results. This indicates that the room balance in humid air with regard to the amount of water vapor was precisely obtained. In addition, this proves that the mass of liquid observed by condensation on the glazed wall was precisely predicted by the CFD model. Figure 2.13 shows the condense traces in areas A3 and F3 for the numerical and experimental results for the first case. In addition, a uniform distribution of condensation on the glass surface owing to the following reasons:

- The jet was symmetric.
- The glazing borders (boundary conditions) had an impact on the results.
- The temperatures of the side walls were the same.
- The temperature was constant in the climatic chamber.
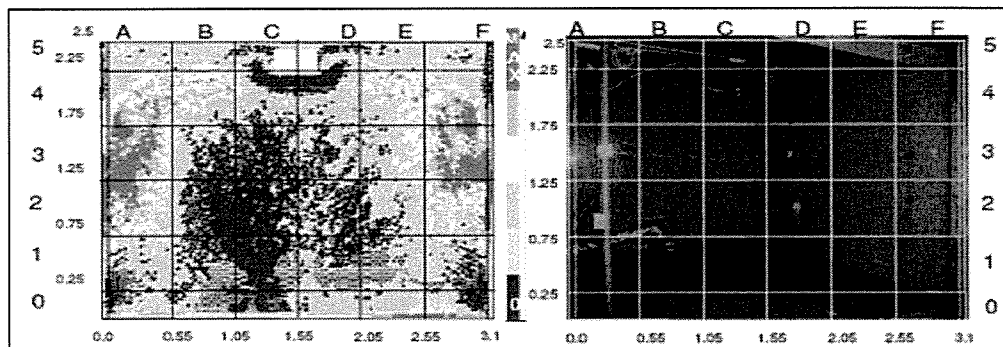
Figure 2.13: Condense distribution on cold glazing for first case (Teodosiu et al., 2015)

Figure 2.14 presents the same results for the numerical and experimental analyses for case 2. The amount of water vapor is more significant than that in case 1.
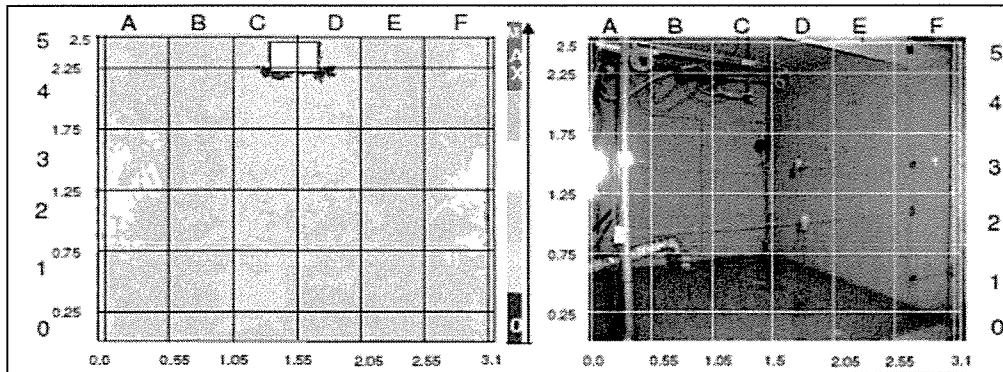
Figure 2.14: Condensation; D = distribution on cold glazing for second case
(Teodosiu et al., 2015)

Li (2013) conducted research to simulate the condensation of water vapor in the presence of noncondensable gas by utilizing CFD to simulate the turbulent flows in a vertical cylindrical condenser tube. Throughout the simulation, the turbulent flow of the gas mixture and the condenser wall was considered in addition to the turbulent flow of the annular channel cooler without assuming a constant temperature of the wall. In addition, it was proposed that a negligible volume was occupied by the condense film, while its influence on the water vapor condensation was considered by imposing a group of boundary conditions. A novel method was utilized to overcome the restrictions of the presently obtainable commercial CFD package when solving the simulation of flows, including multispecies and the fluids of gas and liquid in separate channels.

A comparison between the obtained results from the simulation and other experimental results was conducted for the water vapor condensation with air. The noncondensable gas was considered as an inlet mass fraction of the water vapor from 0.66 to 0.98. There was a high agreement between the results in the literature review

23

and the CFD simulation results. It was also observed that changes in the condenser tube heat flux were considered to be more complex than those of a simple polynomial curve fit. In addition, the CFD results indicated that in flows with a high content of water vapor, the gas mixture had an axial velocity that could not be neglected. The dimensions of the built model of the condenser were defined based on a study by Kuhn (1997). Table 2.4 summarizes the applied experimental conditions provided by Kuhn.

.

Table 2.4: Implemented experimental conditions (Li, 2013)

	P (kPa)	T_{in} (°C)	W_{in}	$\dot{m}_{av}$ (kg/s)	$\dot{m}_c$ (kg/s)	$T_{c,i}$ (°C)
Run 2.1–2	415.3	147.7	0.98	0.01434	0.3521	31.3
Run 2.1–4	390.5	144.8	0.96	0.01464	0.3419	31.0

As previously mentioned, the obtained results from the simulation were compared with the experimental results with regard to the adiabatic wall temperature distribution, centerline temperature, condenser wall temperature distribution, coolant temperature at the exit, and heat flux distribution. Figure 2.15 compares the results of the adiabatic wall temperature distribution in the CFD and experimental analyses. Results were taken for the first two runs of 2-1-2 and 2-1-4. The temperature gradually decreases along the model.
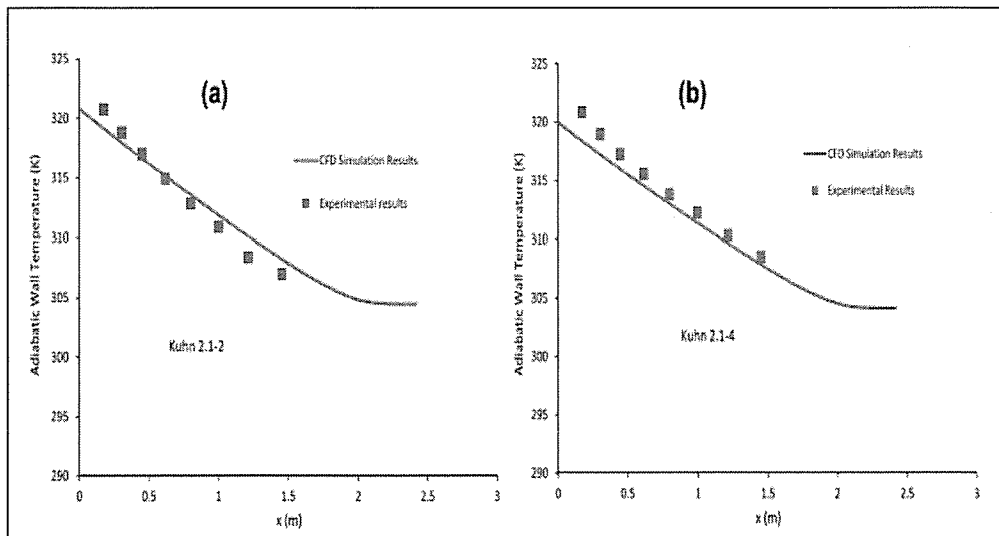
Figure 2.15: Results of adiabatic wall temperature distribution (Li, 2013)

Under the same conditions, the centerline temperature distribution was tested in Figure 2.16.
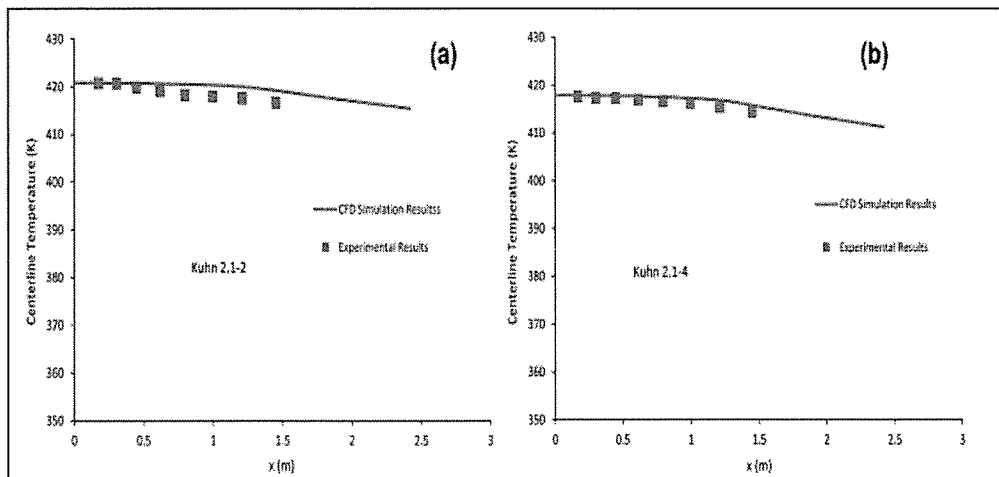
Figure 2.16: Results of centerline temperature distribution (Li, 2013)

Figure 2.17 shows the results of the distribution of the condenser wall temperature as obtained by the CFD and experimental analyses.
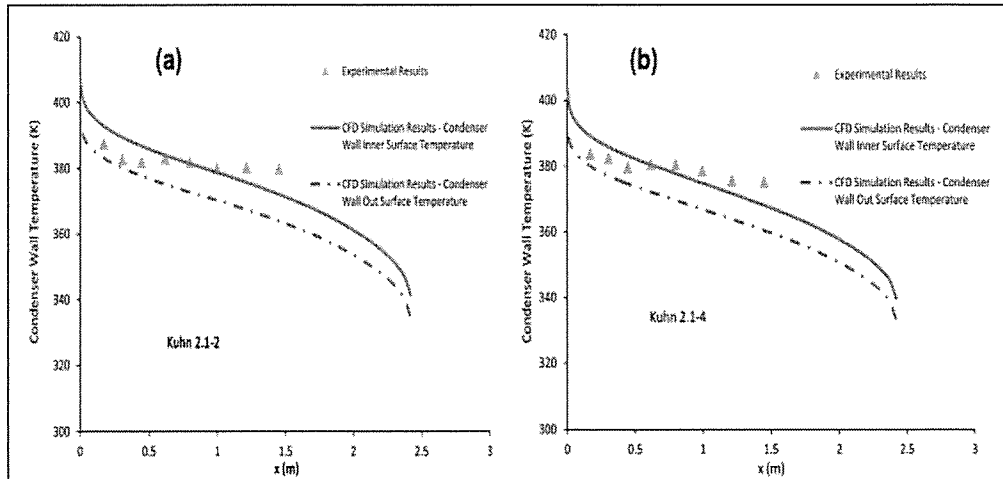
Figure 2.17: Results of distribution of condenser wall temperature (Li, 2013)

The change in the coolant temperature at exit in Figure 2.18.
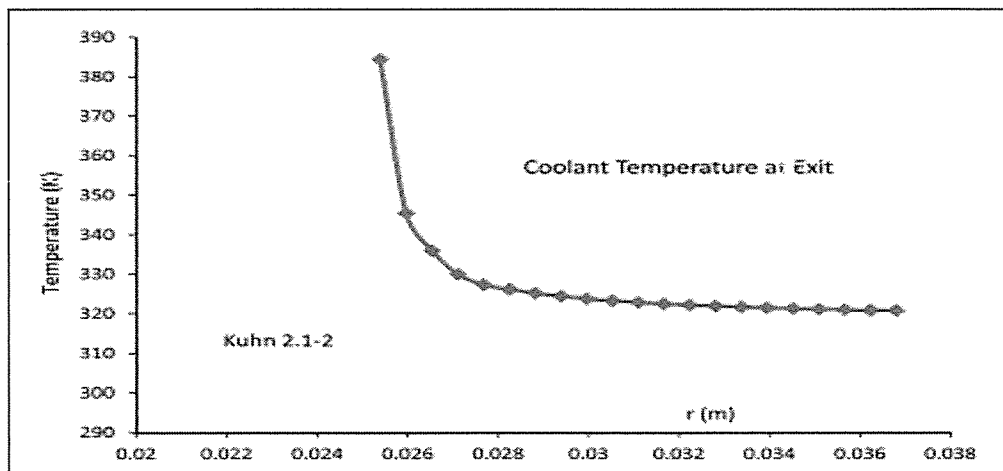
Figure 2.18: Coolant temperature at exit (Li, 2013).

Figure 2.19 in this study compares the heat flux results of the CFD simulation and the results obtained by Kuhn (1997) for the first and second runs. The coolant bulk temperature was measured based on the values of the condenser tube wall temperature, adiabatic wall temperature, and F factor. Based on the measured coolant bulk temperature, the heat flux was estimated. The F factor was calculated by Kuhn (1997) using the k-ε turbulence model for the flow and heat transfer in the coolant channel. The values of the heat flux were used as the input boundary condition in the CFD simulations.
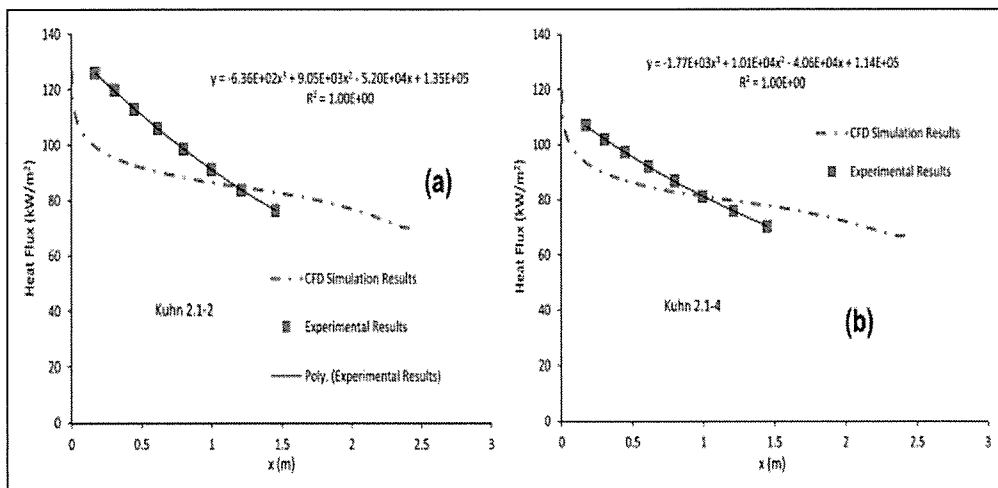
Figure 2.19: Heat flux result comparison between CFD simulation results and Kuhn results for first and second runs (Li, 2013)

Suryaningsih and Nurhilal (2016) provided the optimal design of an AWG based on a TEC for drought in rural areas. This system was applied in Indonesia. A prototype was developed for the AWG based on a TEC that utilized 12-V DC power. CFD was used for model optimization. Parameters such as temperature, moisture content, air flow, pressure, form of the air flow channel, and water productivity per unit input of energy were taken into consideration throughout the analyses. Figure 2.20 shows the model, including the experimental prototype and the components of the AWG device.
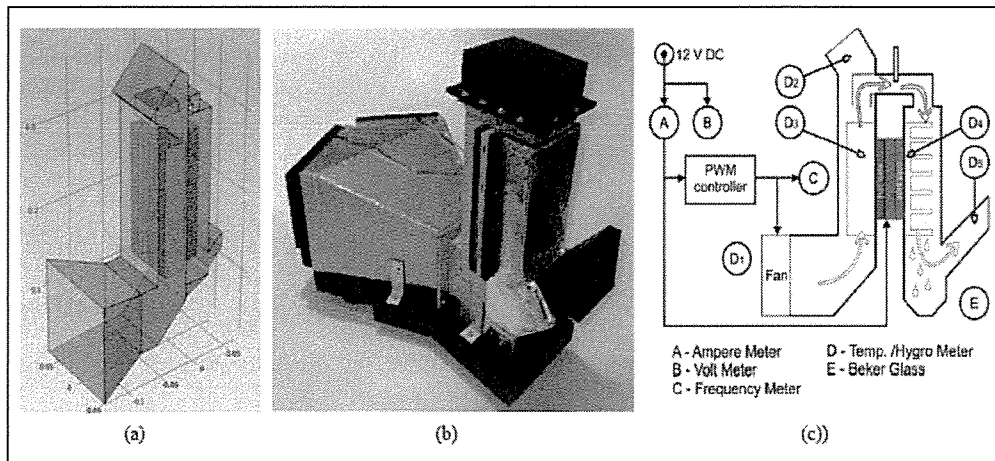
Figure 2.20: Experimental prototype (Suryaningsih and Nurhilal, 2016)

The obtained results are presented in Table 2.5.

Table 2.5: Boundary conditions and measured values (Suryaningsih and Nurhilal, 2016)

TEC Used.	Power (Watts)	PWM Controllef Air Inlet			Ambient Air		Wh (L/h)	Wp (L/h)	CR	PR
		Freq. (Hz)	CFM	(m³/h)	T(°C)	RH (%)				
2	65.52	800	76	129.12	25.3	60	1.57	0.028	0.02	0.09
2	65.52	1200	114	193.69	26	61	2.51	0.050	0.02	0.16
2	65.52	1600	150	254.85	25.5	63	3.31	0.100	0.03	0.32
2	65.52	2000	190	322.81	25.8	58	3.92	0.200	0.05	0.64
4	125.5	800	76	129.12	26	60	1.64	0.320	0.19	1.02
4	125.5	1200	114	193.69	26	59	2.42	0.410	0.17	1.31
4	125.5	1600	150	254.85	26.5	61	3.40	0.490	0.14	1.57
4	125.5	2000	190	322.81	27	62	4.51	0.610	0.14	1.95

Figure 2.21 shows that increasing the air flow capacity resulted in an increase in the water productivity while increasing the power consumption. This resulted in an increase in water production.
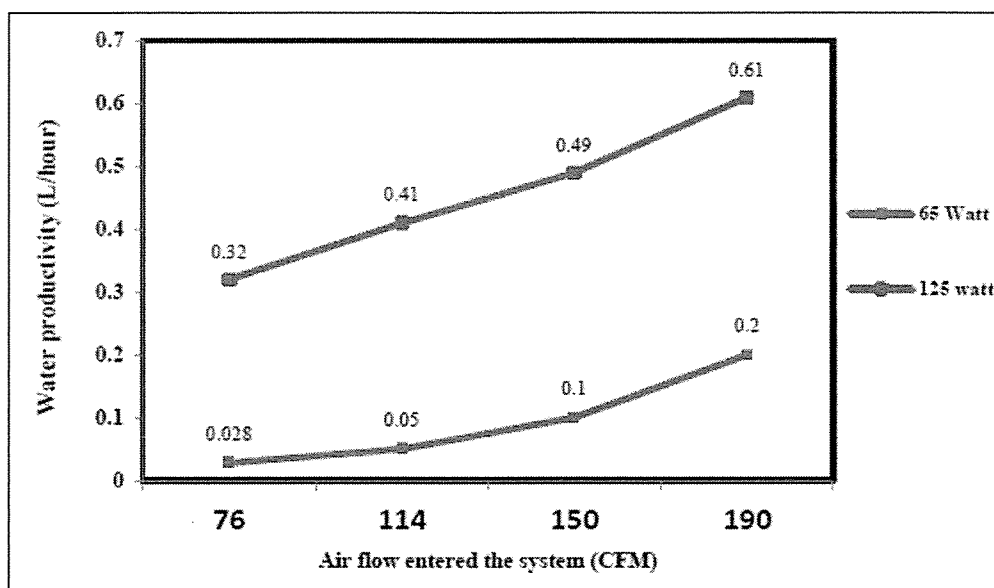
Figure 2.21: Water production (L/h) for different air flows (CFM) and power
consumption (W) (Suryaningsih and Nurhilal, 2016).

2.4   Critical analyses

To establish a novel idea for this study that enhances the performance of water
harvester techniques, previous research works must be critically analyzed to show
their strengths and weaknesses. The strengths will be considered in the new design,
while the weak points or gaps will be improved upon.

In some papers, the researchers did not provide any data about the mass or amount of
produced or recovered water. This prevented the researchers from providing any
indication of the efficiency of the applied system. This gap will be solved in this
study, where the amount of produced water by the proposed device is measured using
two different methods.

The majority of the reviewed papers did not consider the problem of shortages in
electrical energy in the used systems of water extraction from air. This is a very
important problem that occurred in such systems. To solve this gap, this study uses a
thermoelectric cooler to solve the electrical energy shortage. Some researchers

29

conducted a single method of analysis and compared their results with experimental data available in the literature with data from the same experimental conditions. Therefore, in this study, two methods of analysis will be applied to evaluate the amount of produced water: experimental and numerical.

Chapter 3. Methodology

3.1   Overview

This study illustrates the planned and followed methods to achieve the aim of modeling the condensation process of water vapor extraction from air using a device based on the TEC, different methods were applied to estimate the amount of water that can be extracted from air: experimental method, and numerical method. These methods were performed after the collection of literature review data. It is essential to collect theoretical data from previously published papers, journals, websites, and books to understand the study concept and to review previously followed methods for water condensation and water measurement. The collected data are related to the available techniques of water extraction from air, modeling of the condensation process, and the estimated gaps in the previous techniques and models.

A detailed illustration of the followed methods in this study is presented in the following sections.

3.2   Theoretical calculations of fins

The first method of analysis is a theoretical calculation of fins. This model is represented by equations for the conservation laws, fin analysis, and water condensation, as shown below.

In cases when the variations in density are only caused by temperature variations, the volumetric thermal expansion coefficient can be calculated as follows:

3

$$\beta = -\frac{1}{\rho}\left(\frac{\partial \rho}{\partial T}\right)_P \tag{3.1}$$

where β is the volumetric thermal expansion coefficient in K^{-1}. The volumetric thermal expansion coefficient can be defined as the amount of change in density as the temperature changes at a constant pressure. It can be written as (Incropera, 2002):

$$\rho_\infty - \rho \approx \rho\beta(T - T_\infty)$$

(3.2)

This equation is defined as the Boussinesq approximation. By adding this equation to the x-momentum equation, the following equation is generated (Merle, 2011; Incropera, 2002):

$$u\frac{\partial u}{\partial x} + v\frac{\partial u}{\partial y} = g\beta(T - T_\infty) + v\frac{\partial^2 u}{\partial y^2}$$

(3.3)

Equation (3.3) clearly shows the relation between the buoyancy force and the temperature difference. Since the effects of the buoyancy force are limited to the conservation equations of momentum, mass, and energy from forced convection, the equations for their forced convection are used to finish the formulation of the problem. α is the thermal diffusivity in m^2/s.

In Equation (3.4), which is the energy conservation equation, the effect of viscous dissipation is neglected. The effects of free convection are clearly based on the expansion coefficient and depend on the type of fluid. For an ideal gas, the relation between the key parameters is given as $\rho = p/RT$. Then, the volumetric thermal expansion coefficient is written as (Merle, 2011).

$$\beta = -\frac{1}{\rho}\left(\frac{\partial\rho}{\partial T}\right)_P = \frac{1}{\rho}\frac{P}{RT^2} = \frac{1}{T}$$

(3.4)

32

where

R is the gas constant, J/kg·K.

T refers to the value of the absolute temperature. For nonideal gas or any liquid, this value is taken from the appropriate property Table.

3.2.1   Nondimensional parameters

The mechanism of heat transfer between a surface and a fluid can be mainly forced convection or natural convection based on the relative contribution of buoyancy over forced flow. Mixed convection is only considered when the effects of both forced flow and buoyancy are of comparable magnitude. The transfer of heat by natural convection is limited because of the paucity of heat transfer; thus, forced convection delivers a number of immediate solutions. Because natural convection may not be ruled out from a system, the principle of mixed convection is significant to a researcher. This section reviews the principles and governing equations of convection heat transfer modes. In this mode, fluid is forced to move by an external source to increase the heat transfer rate. The characteristics of convection mass and heat transfer between a surface and a fluid flowing past it can be defined by considering the boundary-layer concept and its parameters, as shown below.

For similarity considerations, the heat transfer and flow of free convective for a vertical plate is governed by dimensionless parameters that can be obtained by nondimensional governing equations (Çengel, 1998). These parameters include:

$$x = \frac{x}{L} \text{ and } y = \frac{y}{L} \qquad (3.5)$$

$$u = \frac{u}{u_0} \text{ and } v = \frac{v}{u_0} \qquad (3.6)$$

$$T = \frac{T - T_\infty}{T_s - T_\infty} \qquad (3.7)$$

$$C_A = \frac{C_A - C_{A,s}}{C_{A,\infty} - C_{A,s}} \qquad (3.8)$$

where u and v are mass average fluid velocity components, m/s, v refers to the upstream surface velocity, m/s. C_A is the molar concentration (kmol/m^3). $C_{A,s}$ is the surface molar concentration (kmol/m^3). $C_{A,\infty}$ is the flow molar concentration (kmol/m^3). In these formulas, rearranging the equations can provide dimensional variables in terms of new dimensionless variables such as x = x·L, y = y·L, and so on.

In these parameters, the term L refers to the characteristic length, whereas the term u0 refers to a reference velocity. The given equations of x momentum and energy become (Welty, 1976).

$$u\frac{\partial u}{\partial x} + v\frac{\partial u}{\partial y} = \frac{g\beta(T_s - T_\infty)L}{u_0}T + \frac{1}{Re_L}\frac{\partial^2 u}{\partial y^2} \qquad (3.9)$$

$$u\frac{\partial T}{\partial x} + v\frac{\partial T}{\partial y} = \frac{1}{Re_L Pr}\frac{\partial^2 T}{\partial y^2} \qquad (3.10)$$

In Equation (3.9), the buoyancy force is given by $\frac{g\beta(T_s - T_\infty)L}{u_0^*}T$, which is a dimensionless term. The term u_0 refers to a dimensionless reference velocity and can be given by $u_0^2 = g\beta(T_s - T_\infty)L$. Therefore, the term in Equation (3.10) that involves this velocity becomes unity.

Table 3.1 presents the boundary conditions in the y-direction needed for the solution to the convection equation. By normalizing the equations of the boundary layer, this leads to three significant dimensionless similarity parameters that are also presented

34

in Table 3.1, which are the Reynolds number (Re_L), Schmidt number (Sc), and Prandtl number (Pr). These parameters are not constant; they change based on the fluid type, its velocity, and the surface size in terms of the characteristic length (L).

Table 3.1: Nondimensional forms of equations of boundary layer and their conditions in y-direction (Incropera, 2002)

Boundary Layer	Conservation Equation	Boundary Conditions		Similarity Parameter(s)
		Wall	Free Stream	
Velocity	$u^*\frac{\partial u^*}{\partial x^*}+v^*\frac{\partial u^*}{\partial y^*}=-\frac{dp^*}{dx^*}+\frac{1}{Re_L}\frac{\partial^2 u^*}{\partial y^{*2}}$	$u^*(x^*,0)=0$ $v^*(x^*,0)=0$	$u^*(x^*,\infty)=\frac{u_\infty(x^*)}{V}$	$Re_L=\frac{VL}{\nu}$
Thermal	$u^*\frac{\partial T^*}{\partial x^*}+v^*\frac{\partial T^*}{\partial y^*}=\frac{1}{Re_L Pr}\frac{\partial^2 T^*}{\partial y^{*2}}$	$T^*(x^*,0)=0$	$T^*(x^*,\infty)=1$	$Re_L, Pr=\frac{\nu}{\alpha}$
Concentration	$u^*\frac{\partial C_A^*}{\partial x^*}+v^*\frac{\partial C_A^*}{\partial y^*}=\frac{1}{Re_L Sc}\frac{\partial^2 C_A^*}{\partial y^{*2}}$	$C_A^*(x^*,0)=0$	$C_A^*(x^*,\infty)=1$	$Re_L, Sc=\frac{\nu}{D_{AB}}$

To solve these equations, the above momentum equation shows that the velocity boundary-layer conditions based on the fluid properties of density, length, and velocity can be written in one relation called the Reynolds number relation. The velocity equation in Table 3.1 can be solved based on the following solution form (Incropera, 2002):

$$u = f\left(x, y, Re_L, \frac{\partial_P}{\partial_x}\right) \tag{3.11}$$

where u^* is the dimensionless velocity, m/s. f refers to fluid properties x^* and y^*, which are dimensionless rectangular coordinates, m. Re_L is the Reynolds number. $\frac{dP^*}{dx^*}$

is the first derivative of pressure, which is defined as the pressure distribution based on the geometry of the surface. This can be found independently by taking into consideration the flow conditions in the free stream.

Equation (3.12) calculates the value of the friction coefficient on the surface (Incropera, 2002):

$$C_f = \frac{\tau_s}{\rho V^2/2} = \frac{2}{Re}\frac{\partial_u}{\partial_y}\ , at\ y = 0 \qquad (3.12)$$

where C_f is the friction coefficient. V is the shear velocity, m/s.

The same results can be achieved for the convection heat and mass transfer coefficients. It can be expected that the coefficient of h is a function of the fluid properties of k: thermal conductivity, W/m·K; c_p: specific heat at constant pressure, J/kg·K; μ: viscosity, kg/s·m; and ρ: density, kg/m3; the surface geometry; the length scale (L); and the fluid velocity (V). The thermal equation in Table 3.1 can be written as (Incropera, 2002):

$$T = f\left(x, y, Re_L, Pr, \frac{\partial P}{\partial x}\right) \qquad (3.13)$$

where Pr is the Prandtl number. The following equation refers to the key definition of the convection heat transfer coefficient (Welty, 1976):

$$h = -\frac{k_f\ (T_\infty - T_s)\partial T}{L(T_s - T_\infty)\partial_y} \qquad at\ y = 0 \qquad (3.14)$$

36

$$h = +\frac{k_f}{L}\frac{\partial T}{\partial y} \qquad at\ y = 0 \qquad\qquad (3.15)$$

where h is the convection heat transfer coefficient, W/m^2·K. k$_f$ is the thermal conductivity, W/m·K. T is the absolute temperature, K. Equation (3.16) proposes a definition for a significant dependent dimensionless parameter known as the Nusselt number, which is given by Incropera (2002):

$$Nu = \frac{hL}{k_f} = +\frac{\partial T}{\partial y} \quad at\ y = 0 \qquad\qquad (3.16)$$

where Nu is the Nusselt number. As shown in Equation (3.16), the Nusselt number is a function of the dimensionless temperature gradient at the wanted surface. It mainly refers to the amount of convection heat transfer that takes place at the surface. For a prescribed geometry, the Nusselt number can be written as (Welty, 1976)

$$Nu = f(x, Re_L, \mathrm{Pr}) \qquad\qquad (3.17)$$

Equation (3.17) indicates that for a given geometry, the Nusselt number should be some universal function of x*, Re$_L$, and Pr. As this function is defined, then Nu can be calculated from this function for various fluids of various lengths and velocities. Equation (3.18) calculates the average Nusselt number over the body surface that is independent of the spatial variable x* (Welty, 1976):

$$\overline{Nu} = \frac{\overline{h}}{k_f} = f(Re_L, \mathrm{Pr}) \qquad\qquad (3.18)$$

$\overline{Nu}$ is the average Nusselt number, and $\overline{h}$ is the average convection heat transfer coefficient. In a similar manner, it can be said that the convection mass transfer (h$_m$)

37

in a gas flow over a sublimating solid or an evaporating liquid is a function of D_{AB}, velocity, μ, and ρ in addition to the characteristic length (L). For the concentration equation in Table 3.1, the following function simplifies the relation between the solution parameters (Incropera, 2002):

$$C_A = f\left(x, y, Re_L, Sc, \frac{\partial P}{\partial x}\right) \tag{3.19}$$

where Sc is the Schmidt number. Equation (3.20) defines the general formula of the convection mass transfer coefficient (Incropera, 2002):

$$h_m = \frac{D_{AB}}{L} \frac{\left(C_{A,\infty} - C_{A,s}\right)}{\left(C_{A,s} - C_{A,\infty}\right)} \cdot \frac{\partial C_A}{\partial y} \quad at\ y = 0 \tag{3.20}$$

$$h_m = \frac{D_{AB}}{L} \frac{\partial C_A}{\partial y}\ at\ y = 0 \tag{3.21}$$

where h_m is the convection mass transfer coefficient, m/s. D_{AB} is the binary mass diffusivity, m^2/s. An additional dependent dimensionless parameter that must be defined is the Sherwood number (Sh), which is given in Equation (3.22) (Incropera, 2002):

$$Sh = \frac{h_m L}{D_{AB}} = +\frac{\partial C_A}{\partial y}\ at\ y = 0 \tag{3.22}$$

where Sh is the Sherwood number. It refers to a surface dimensionless concentration gradient that evaluates the amount of convection mass transfer taking place at the surface. For a prescribed geometry, this parameter is given as (Incropera, 2002)

$$Sh = Sh = f(x, Re_L, Sc) \qquad (3.23)$$

Equation (3.24) describes the average Sherwood number, which is based only on Re_L and Sc (Incropera, 2002):

$$\overline{Sh} = \frac{\overline{h_m}L}{D_{AB}} = f(Re_L, Sc) \qquad (3.24)$$

where $\overline{Sh}$ is the average Sherwood number, and $\overline{h}m$ is the average convection mass transfer coefficient, m/s. For a nonideal gas or any liquid, this value is taken from the appropriate property Table.

3.3   Governing equations of fluid motion

The water extraction process from humid air is defined in this section using a theoretical model by defining seven governing equations of the total process. In these equations, the fluid behavior is defined in terms of seven macroscopic properties:

- Velocity, u
- Pressure, p
- Density, ρ
- Temperature, T
- Energy, E

- Humidity/salinity, q/s

These properties of fluid are averages of an adequately large number of molecules. Figure 3.1 illustrates a fluid element that is assumed to have the smallest volume for which the continuum supposition is applicable.
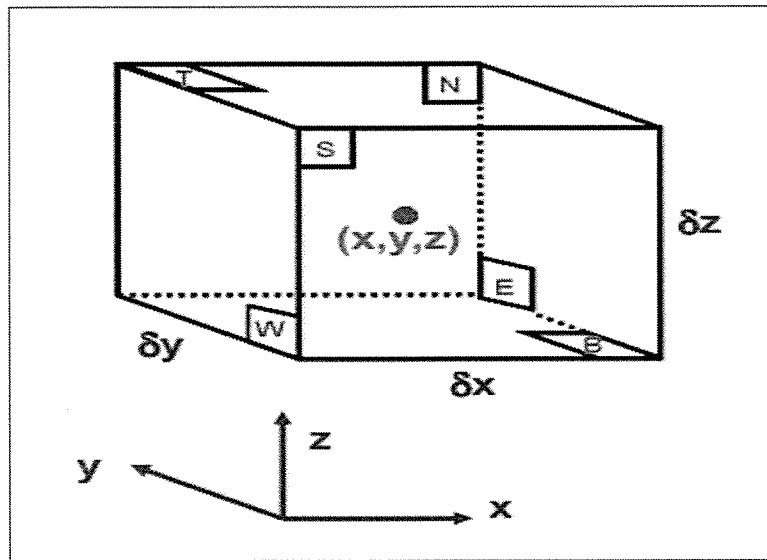
Figure 3.1: Fluid element for conservation laws

The seven properties of this element are defined within seven equations that together govern the motion of fluid. These equations include the physical laws of mass, momentum, and energy conservation; Newton's second law; and the first and second thermodynamic laws. Each of these equations is discussed separately below.

3.3.1   Conservation of mass

One of the essential statements to be considered in fluid flow mechanics is the conservation of mass. Mathematically, the mass conservation statement is defined by considering a small fixed volume element around point (x, y, z), where this element has three sizes of Δx, Δy, and Δz, as displayed in Figure 3.2.

40
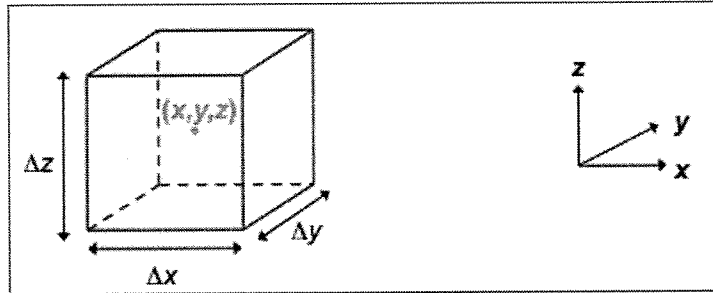
Figure 3.2: Fixed-volume element

Fluid density (ρ) is defined as 1.25 kg·m^{-3} when the fluid is air, and 1030 kg·m^{-3} when the fluid is seawater. The velocity components in the three directions of x, y, and z are defined by u, v, and w, respectively.

Inside the given volume element in Figure 3.2, the mass is defined by $\Delta m = \rho \Delta x \Delta y \Delta z$, which is called the conservation of mass equation. The value of this equation varies based on the overall mass inflow when all of the element sides $\neq 0$. Figure 3.3 shows the mass inside the element volume.

Mass flux 'right' : $\rho u \big|_{(x+\frac{1}{2}\Delta x, y, z)} \approx \rho u \big|_{(x,y,z)} + \frac{\partial}{\partial x}(\rho u)\big|_{(x,y,z)} \frac{1}{2}\Delta x$
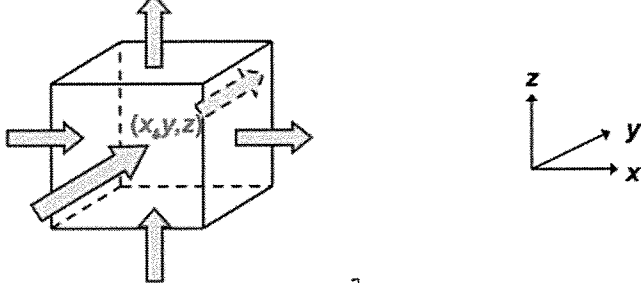
Mass flux 'left' : $\rho u \big|_{(x-\frac{1}{2}\Delta x, y, z)} \approx \rho u \big|_{(x,y,z)} - \frac{\partial}{\partial x}(\rho u)\big|_{(x,y,z)} \frac{1}{2}\Delta x$

Total mass/time entering through left+right side: (flux left - flux right) $\Delta y \Delta z$

41

Figure 3.3: Definition of mass inside volume

Figure 3.4 shows the derivation of the overall mass per time passing through the right and left sides of the volume element.

$$\left[\cancel{\rho u}\big|_{(x,y,z)} - \frac{\partial}{\partial x}(\rho u)\big|_{(x,y,z)} \frac{1}{2}\Delta x - \left(\cancel{\rho u}\big|_{(x,y,z)} + \frac{\partial}{\partial x}(\rho u)\big|_{(x,y,z)} \frac{1}{2}\Delta x \right) \right] \Delta y \Delta z$$

$$= -\frac{\partial}{\partial x}(\rho u)\Delta x \, \Delta y \Delta z$$

(x,y,z)

Likewise,
through front + back side: $\quad = -\dfrac{\partial}{\partial y}(\rho v)\Delta x \, \Delta y \Delta z$

through top + bottom side: $\quad = -\dfrac{\partial}{\partial z}(\rho w)\Delta x \, \Delta y \Delta z$

Figure 3.4: Total mass per time definition

Thus,

$$\frac{\partial}{\partial t}(\rho \Delta x \Delta y \Delta z) = \left[-\frac{\partial}{\partial x}(\rho u) - \frac{\partial}{\partial y}(\rho v) - \frac{\partial}{\partial z}(\rho w) \right] \Delta x \Delta y \Delta z \qquad (3.25)$$

By dividing the two sides of the equation by $\Delta x \Delta y \Delta z$, we have

$$\frac{\partial \rho}{\partial t} + \frac{\partial}{\partial x}(\rho u) + \frac{\partial}{\partial y}(\rho v) + \frac{\partial}{\partial z}(\rho w) = 0 \qquad (3.26)$$

This is called a continuity equation.

The above equation is written in terms of vector notation as follows:

$$\frac{\partial \rho}{\partial t} + \nabla \cdot (\rho \overline{V}) = 0 \qquad (3.27)$$

This equation represents the first equation of the seven governing equations.

3.3.2 Momentum and energy conservation

The momentum conservation equations can be written in the three dimensions x, y, and z. These equations are derived from Newton's second law (White, 1999).

$$\rho \frac{\partial u}{\partial t} + \rho u \frac{\partial u}{\partial x} + \rho v \frac{\partial u}{\partial y} + \rho w \frac{\partial u}{\partial z}$$
$$= -\frac{\partial p}{\partial x} + pg_x + \mu \frac{\partial^2 u}{\partial x^2} + \mu \frac{\partial^2 u}{\partial y^2} + \mu \frac{\partial^2 u}{\partial z^2} \qquad (3.28)$$

$$\rho \frac{\partial v}{\partial t} + \rho u \frac{\partial v}{\partial x} + \rho v \frac{\partial v}{\partial y} + \rho w \frac{\partial v}{\partial z}$$
$$= -\frac{\partial p}{\partial y} + pg_y + \mu \frac{\partial^2 v}{\partial x^2} + \mu \frac{\partial^2 v}{\partial y^2} + \mu \frac{\partial^2 v}{\partial z^2} \qquad (3.29)$$

$$\rho \frac{\partial w}{\partial t} + \rho u \frac{\partial w}{\partial x} + \rho v \frac{\partial w}{\partial y} + w\rho \frac{\partial w}{\partial z}$$
$$= -\frac{\partial p}{\partial z} + pg_z + \mu \frac{\partial^2 w}{\partial x^2} + \mu \frac{\partial^2 w}{\partial y^2} + \mu \frac{\partial^2 w}{\partial z^2} \qquad (3.30)$$

In the above equations,

- P is the pressure, N/m^2.
- ρ is the fluid density, kg/m^3.
- g is the gravitational acceleration, m/s^2.

The energy conservation equation can be written as follows (Merle, 2011):

$$\rho \frac{DU}{Dt} = k \left(\frac{\partial^2 T}{\partial x^2} + \frac{\partial^2 T}{\partial y^2} + \frac{\partial^2 T}{\partial z^2} \right) - p \left(\frac{\partial u}{\partial x} + \frac{\partial v}{\partial y} + \frac{\partial w}{\partial z} \right) \quad (3.31)$$

where

- U: internal energy
- k: thermal conductivity
- T: temperature in K.

3.3.3   Other equations

The fluid system description is incomplete without presenting a relation between the pressure and density, where this relation is defined as the equation of state. Additional equations include the thermodynamic (heat) equation and mass conservation for moisture/salt.

For the equation of state,

- ρ = constant (homogeneous fluid)
- $\rho = \rho$ (p) (barotropic fluid)

where the density ρ depends on the pressure (P), temperature (T), and specific humidity/salinity (q/s).

The atmospheric air is usually composed of water vapor. For this moist air, the ideal gas general equation is written in a general form by introducing an additional factor that changes as the specific humidity q is changed:

$$\rho = \frac{P}{RT(1 + 0.61q)},$$ (3.32)

where q is the specific humidity given by:

$$q = water\ vapor\frac{mass}{air}mass$$ (3.33)

for the thermodynamic heat equation.

From the first and second laws of thermodynamics:

$$\rho\ c_p\ \frac{DT}{Dt}\ -\ \alpha T\ \frac{Dp}{Dt} =\ \nabla\ \cdot (k_T \nabla T\ - F_{rad}\ ) +\ \rho Q,$$ (3.34)

where

- c_p (J·kg^{-1}K^{-1}): specific heat at constant pressure
- α (K^{-1}): thermal expansion coefficient
- k_T (W·m^{-1}K^{-1}): thermal diffusion coefficient
- F_{rad} (W·m^{-2}): radiative fluxes
- Q: heating rate per mass (e.g., latent heat release)

The last equation in the governing equations is called the water-mass continuity equation and is given by

$$\frac{\partial(\rho q)}{\partial t} + \nabla \cdot \left(\rho q \vec{V}\right) = S_o - S_x \qquad (3.35)$$

where S includes the sources and sinks of water to the atmosphere.

3.3.4   Summary of governing equations

As previously mentioned, the motion of air or any other ideal gases is characterized by seven variables of u, v, w, p, T, q, and ρ, which are defined within seven equations. These equations are summarized as follows.

Continuity equation:

$$\frac{\partial \rho}{\partial t} + \nabla \cdot \left(\rho \vec{V}\right) = 0 \qquad (3.36)$$

Momentum equations:

$$\frac{\partial u}{\partial t} + \vec{V}.\nabla u = -\frac{1}{\rho}\frac{\partial p}{\partial x} + f_v \qquad (3.37)$$

$$\frac{\partial v}{\partial t} + \vec{V} \cdot \nabla v = -\frac{1}{\rho}\frac{\partial p}{\partial y} - f_u \qquad (3.38)$$

$$\frac{\partial w}{\partial t} + \vec{V} \cdot \nabla w = -\frac{1}{\rho}\frac{\partial p}{\partial z} - g \qquad (3.39)$$

Thermodynamic equations:

$$\frac{\partial(\rho q)}{\partial t} + \nabla \cdot \left(\rho q \vec{V}\right) = S_o - S_x \qquad (3.40)$$

46

$$c_p \frac{DT}{Dt} - \frac{1}{\rho} \frac{Dp}{Dt} = \dot{Q} \qquad (3.41)$$

$$P = \rho R_d T (1 + 0.61q) \qquad (3.42)$$

These seven governing equations discussed in the above section can be solved numerically using different methods. In ANSYS Fluent, the instantaneous mass, momentum, and energy conservation laws are defined in terms of transport equations. For turbulent flows, these equations are averaged, resulting in extra terms. The instantaneous formulas of mass, momentum, and energy conservation are defined as follows.

According to the ANSYS Fluent guide, the continuity equation is defined as

$$\frac{\partial \rho}{\partial t} + \nabla \cdot (\rho U) = 0 \qquad (3.43)$$

The momentum equation is defined as

$$\frac{\partial (\rho U)}{\partial t} + \nabla \cdot (\rho U \ \Theta U) = -\nabla \rho + \nabla \cdot \tau + S_M, \qquad (3.44)$$

where τ refers to the stress tensor, which is defined in relation to the strain rate as follows:

$$\tau = \mu \left(\nabla \vec{V} + \left(\nabla \vec{V}^T \right)^{-\frac{2}{3} \nabla \cdot \vec{V} I} \right) \qquad (3.45)$$

The equation that defines the total energy is given by

47

$$\frac{\partial \rho h_{tot}}{\partial t} - \frac{\partial p}{\partial t} + \nabla \cdot (\rho.U.h_{tot}) = \nabla \cdot (\lambda \nabla T) + \nabla \cdot (U.\tau) + U \cdot S_M S_E \qquad (3.46)$$

where h_{tot} defines the total enthalpy, which is given by the following equation in terms of the static enthalpy h (T, p):

$$h_{tot} = h + \frac{1}{2}U^2 \qquad (3.47)$$

$\nabla.(U.\tau)$ refers to the work done because of the viscous stress.

$U.S_M$ refers to the work done because of an external momentum source.

These transport equations should be augmented with additional equations that define the density and enthalpy state to finally provide a closed system. Within ANSYS Fluent, the equations of state are defined as follows:

$$\rho = \rho(p, T) \qquad (3.48)$$

$$dh = \frac{\partial h}{\partial T} |p \, dT + \frac{\partial h}{\partial p} |T \, dp = c_p dT + \frac{\partial h}{\partial p} |T \, dp \qquad (3.49)$$

$$c_{p=c_p} \, (p,T) \qquad (3.50)$$

The results of the theoretical model are presented in the Appendix after the experimental analysis is completed.

3.3.5   Turbulence modelling (k-ε)

A realizable k-ε model was utilized by several studies to model the turbulence in a numerical simulation of the condensation process. The k-ε equation expresses the

convective diffusion, production (by deformation and viscous shear), and dissipation, as shown in the following equation. $\frac{\partial}{\partial x_i}\left(\frac{\mu}{\sigma}\frac{\partial k}{\partial x_i}\right)$ is the diffusion term, and the viscosity (μ) is the effective viscosity, $\mu\frac{\partial U_i}{\partial x_i}\left(\left(\frac{\partial U_i}{\partial x_j}+\frac{\partial U_j}{\partial x_i}\right)-\frac{2}{3}\rho\delta_{ij}k\right)$ represents the production by deformation and shear stress, and $c_d\frac{\rho k^{1.5}}{l}$ represents the dissipation (Gerald, 2009).

$$\frac{Dk}{Dt}=\frac{\partial}{\partial x_i}\left(\frac{\mu}{\sigma}\frac{\partial k}{\partial x_i}\right)+\mu\frac{\partial U_i}{\partial x_i}\left(\left(\frac{\partial U_i}{\partial x_j}+\frac{\partial U_j}{\partial x_i}\right)-\frac{2}{3}\rho\delta_{ij}k\right)-c_d\frac{\rho k^{1.5}}{l} \qquad (3.51)$$

ε represents the eddy kinetic energy during one cycle rotation.

The following equations calculate the convective diffusion, production (by deformation and viscous shear), and dissipation, where $\frac{\partial}{\partial x_i}\left(\frac{\mu}{\sigma}\frac{\partial \epsilon}{\partial x_i}\right)$ is the diffusion term, $C_\epsilon\mu\frac{\partial U_i}{\partial x_i}\left(\left(\frac{\partial U_i}{\partial x_j}+\frac{\partial U_j}{\partial x_i}\right)-\frac{2}{3}\rho\delta_{ij}k\right)$ represents the production by deformation and shear stress, and $c_\epsilon\frac{\rho\epsilon^2}{k}$ represents the dissipation (Gerald, 2009).

$$\frac{D\epsilon}{Dt}=\frac{\partial}{\partial x_i}\left(\frac{\mu}{\sigma}\frac{\partial \epsilon}{\partial x_i}\right)+C_\epsilon\mu\frac{\partial U_i}{\partial x_i}\left(\left(\frac{\partial U_i}{\partial x_j}+\frac{\partial U_j}{\partial x_i}\right)-\frac{2}{3}\rho\delta_{ij}k\right)-c_\epsilon\frac{\rho\epsilon^2}{k} \qquad (3.52)$$

Two-equation turbulent models are usually determined within ANSYS Fluent to solve the turbulent flow. Within these models, the length scale and velocity are solved by applying separate transport equations. These two equation models are known as k-ε and k-ω. They utilize a gradient diffusion hypothesis to relate the Reynolds stresses to the mean velocity gradients and the turbulent viscosity, which is modeled as a turbulent length scale and turbulent velocity product.

In the k-ε model in ANSYS Fluent, the term k is the turbulent kinetic energy, which refers to the velocity fluctuations. The term ε refers to the eddy dissipation of the turbulent flow. The following equation defines the continuity equation according to the k-ε model:

$$\frac{\partial \rho}{\partial t} + \frac{\partial}{\partial x_j}\left(\rho U_j\right) = 0 \tag{3.53}$$

The momentum equation is defined as

$$\frac{\partial \rho U_i}{\partial t} + \frac{\partial}{\partial x_j}\left(\rho U_i U_j\right) = -\frac{\partial p}{\partial x_i} + \frac{\partial}{\partial x_j}\left[\mu_{eff}\left[\frac{\partial U_i}{\partial x_j} + \frac{\partial U_j}{\partial x_i}\right]\right] + S_M \tag{3.54}$$

In this equation, S_M refers to the body-forces sum, and μ_{eff} refers to the effective velocity for turbulent flow. The term $\acute{p}$ defines the modified pressure. μ_{eff} is given by:

$$\mu_{eff} = \mu + \mu_t \tag{3.55}$$

The turbulent viscosity μ_t is given by:

$$\mu_t = \rho C_\mu \frac{k^2}{\varepsilon}. \tag{3.56}$$

The k and ε values are directly obtained from the differential transport equations for the turbulent kinetic energy and turbulent dissipation rate, as shown below:

$$\frac{\partial(\rho k)}{\partial t} + \frac{\partial}{\partial x_j}(\rho U_j k) = \frac{\partial}{\partial xj} - \left[\left(\mu + \frac{\mu_t}{\sigma_k}\right)\frac{\partial k}{\partial x_j}\right] + P_k - \rho\varepsilon + P_{kb} \tag{3.57}$$

$$\frac{\partial(\rho\varepsilon)}{\partial t} + \frac{\partial}{\partial x_j}\left(\rho U_j \varepsilon\right) = \frac{\partial}{\partial x_j} - \left[\left(\mu + \frac{\mu_t}{\sigma_\varepsilon}\right)\frac{\partial \varepsilon}{\partial x_j}\right] + \frac{\varepsilon}{k}\left(C_{\varepsilon 1}P_k - C_{\varepsilon 2}\rho\varepsilon + C_{\varepsilon 1}P_{\varepsilon b}\right) \quad (3.58)$$

The terms P_{kb} and $P_{\varepsilon b}$ define the effects of the buoyancy forces.

3.4   Experimental analysis

The second method that was used in this study to measure the amount of water produced by the proposed Water Harvester device is an experimental analysis method. A full description of the used equipment, procedures, and conditions is presented in the following subsections.

3.4.1   Experimental apparatus

An experimental apparatus was used in this study to measure the condensation flow parameters including the inlet air temperature, cooling surface temperature, and RH. This device is shown in Figure 3.5 and consists of two small fans, a Peltier module attached to the cooling surface, and a heat sink. These are also presented in Appendix A.
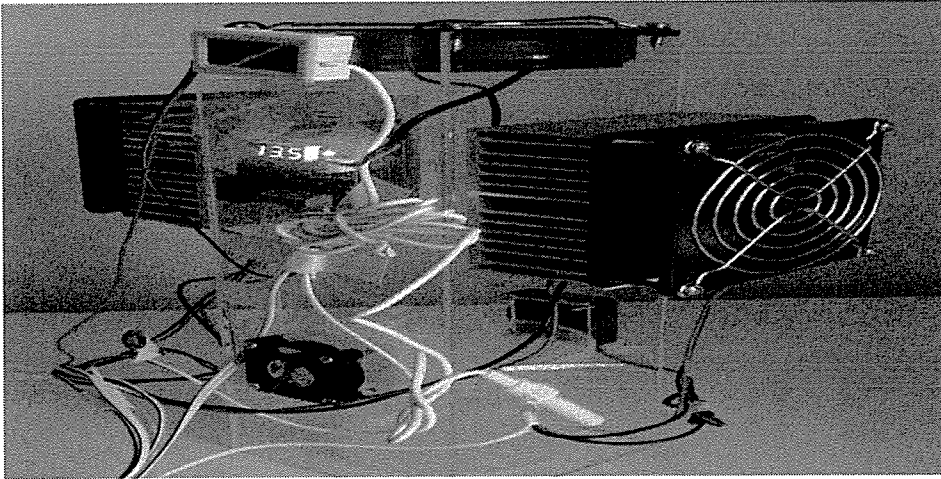
Figure 3.5: Experimental equipment of length 30 cm × width 10 cm

In this device, the water harvester unit uses a fan to blow air on the cooling surfaces as the resulting water vapor in the air condenses on the surface and is collected in the container. This procedure is presented in Figure 3.6.
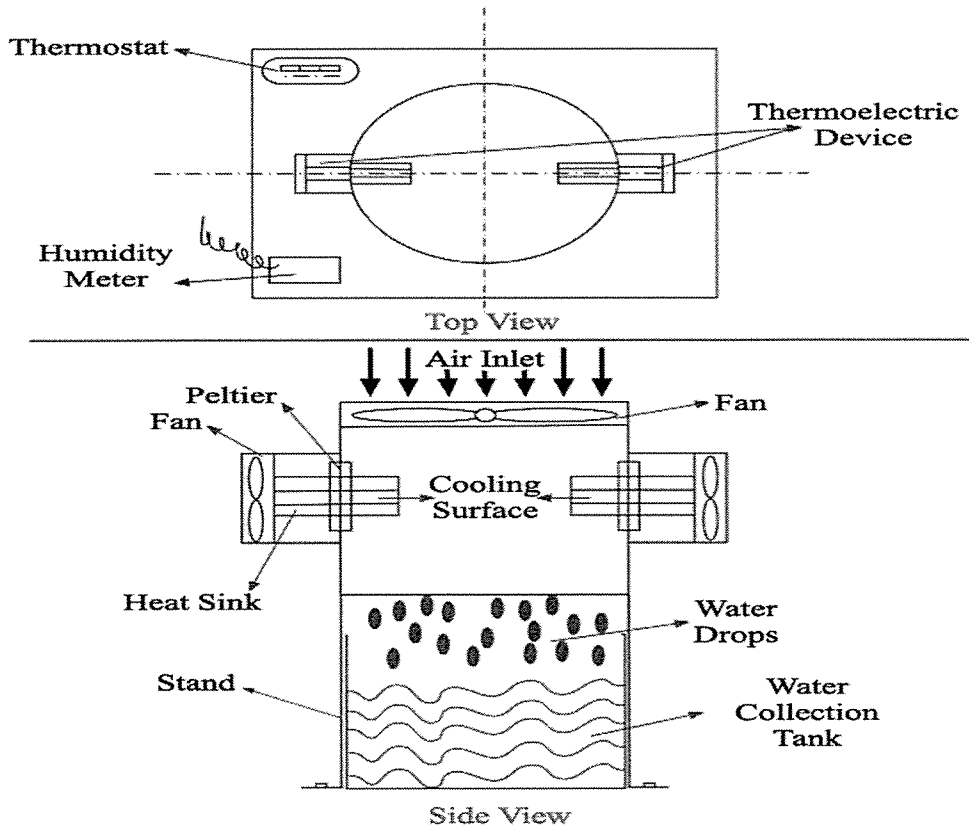
Figure 3.6: Apparatus design

The geometric data of the cooling surfaces are as follows:

The system includes 11 fins, 4 of which are located at two sides of the system and have a length of 18 mm. The other 7 fins have a length of 15 mm. The first 4 fins have a thickness of 1.40 mm, and the other 7 fins have a thickness of 0.8 mm. All 11

fins have an equal width of 46 mm. The cooling surface is proposed to be made from aluminum.

3.5   Experimental conditions

The water harvester device was applied to perform to experiments at different two conditions which are illustrated as follows;

3.5.1   Condition 1: Actual condition

The first experiment was performed at actual weather condition, where the amount of water that can be extracted from air is measured at different temperatures and different relative humidity.

3.5.2   Condition 2: Controlled condition

For the second experiment, it was performed at a fixed temperature of 40 °C. It was performed at climate chamber with a constant relative humidity of 85%. This condition was performed for improvement purposes where its results will be compared to the numerical analysis.

3.5.3   Data collection

By following the experimental procedure described in this Chapter, different experimental parameters were measured. These parameters include the cooling surface temperature (°C), air temperature (°C), RH (%), these parameters are presented in Table 3.2.

Table 3.2: Data collected for suggested model

Air Inlet T (°C)	Cooling Surface T (°C)	RH%
34.7	22.2	66
35.4	22.3	71
33	20.3	72
32.1	20.1	78
32.7	20.9	79
32.4	21.2	83
37.2	23.2	85
32.3	21.2	91
31.6	20.9	94

The dew point temperature is measured from the dry bulb temperature and RH. To cool unsaturated air, the humidity content and partial pressure of the water initially remain constant. Nevertheless, the RH increases because the saturated water vapor pressure coming from above increasingly approximates the partial water vapor pressure, which means that the cold air can absorb less humidity than warm air. As the saturation limit reaches 100% RH, i.e., as the saturated water vapor pressure equals the partial water vapor pressure, this is known as the dew point temperature. Figure 3.7 shows the equations used to calculate the dew point temperature.

$$\varphi = U_w \div 100\%$$ [ ] φ Relative Humidity

U_w Relative Humidity in %

$$p_s = C_1 * \exp\frac{C_2 * t}{C_3 + t}$$ [mbar] p_s saturated water vapour pressu

t temperature in °C

$$p_d = p_s * \varphi$$ [mbar] $C_{1,2,3}$ Magnus coefficient from table

p_d partial water vapour pressure

$$tp = \frac{-\ln\frac{p_d}{C_1} * C_3}{\ln\frac{p_d}{C_1} - C_2}$$ [°C] tp dew point temperature

Figure 3.7: Dew point temperature calculation

The coefficients in the above equations have the following values in Table 3.3.

Table 3.3: Values of given coefficients

Phase	t	C_1	C_2	C_3
	°C	mbar	-	°C
Ice	-50.9 to 0.0	6.10714	22.44294	272.440
Water	-50.9 to 0.0	6.10780	17.84362	245.425
Water	0.0 to 100	6.01780	17.08085	234.175

Chapter 4 . Experimental analysis and results

4.1   Actual conditions results

The humid air was condensed on the cooling surface which is contact to the thermoelectric cooler. The air will condense if the cooling surface temperature is less than the dew point temperature. Table 4.1 shows the dew point temperature for different experimental records as well as the amount of water, as shown, the dew point is higher than the cold temperature for the different records.

Table 4.1: Recorded data for experimental analysis

	Day Time	Cooling surface temperature (°C)	Air temperature (°C)	RH (%)	Dew point (°C)	Amount of water (g)
1	9–11	21.2	32.4	83	29.14	56
2	11–13	20.9	31.6	94	30.51	85
3	13–15	21.2	32.3	91	30.64	71
4	15–17	22.3	35.4	71	29.33	58
5	17–19	23.2	37.2	85	34.25	57
6	19–21	23.0	38.9	55	28.21	55
7	21–23	23.7	39.2	52	27.52	45
8	23–1	22.2	34.7	66	27.41	50
9	1–3	20.3	33.0	72	27.27	56
10	3–5	19.2	32.9	68	26.2	54
11	5–7	20.9	32.7	79	28.57	60
12	7–9	20.1	32.1	78	27.77	71

Figure 4.1 shows the relation between the RH and the dew point temperature. As shown in the Figure, as the RH increases, the dew point temperature increases proportionally. Some points in the graph are misaligned; this behavior results from the variation in the air temperature, where the dew point temperature is a function of the air temperature and RH.
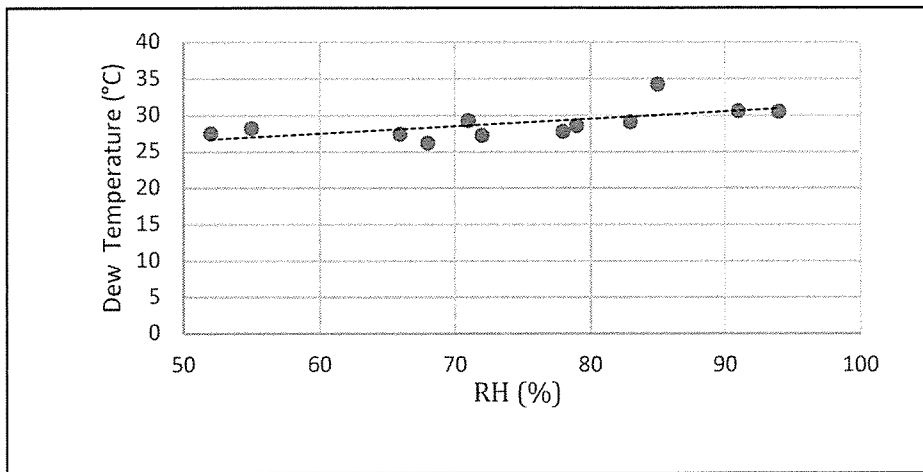
Figure 4.1: Relation between RH and dew point temperature

Figure 4.2 shows the relation between the cooling surface temperature and air temperature. It is clear that there is a proportional relation between these two temperatures where the cooling surface temperature increases as the air temperature increases. At a maximum air temperature of 39.2 °C, a maximum cooling surface temperature of 23.7 °C was obtained.
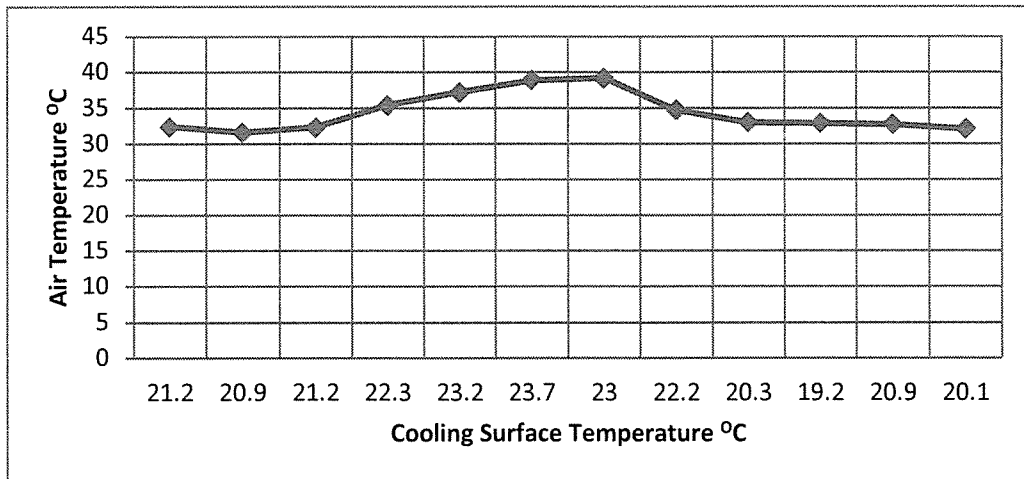
Figure 4.2: Relation between air temperature and cooling surface temperature

A similar relation between these temperatures was observed by Saraireh (2012), as shown in Figure 4.3.
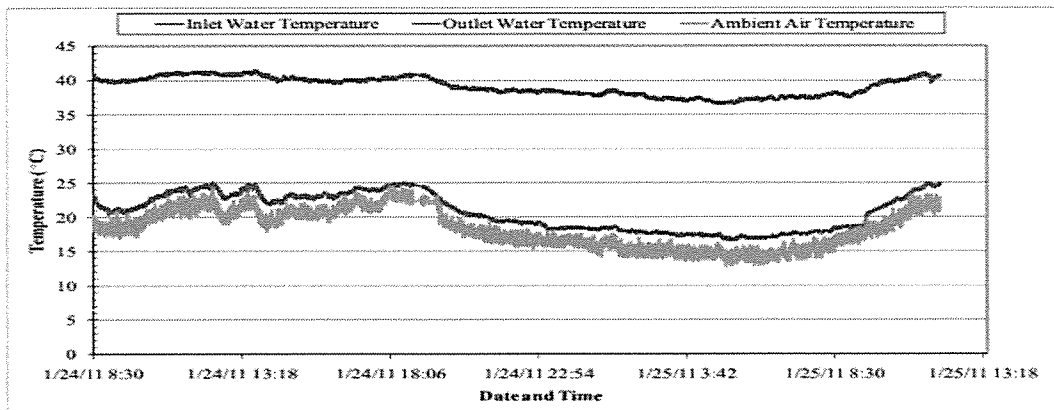
Figure 4.3: Relation between air temperature and cooling surface temperature at different dates and times

Figure 4.4 shows the relation between the amount of water produced by condensation and the RH of air. Increasing the RH of air from 52 to 94% resulted in a proportional increase in the condensation rate of water from this air. The maximum amount of produced water was measured as 85 g at a maximum RH of 94%.
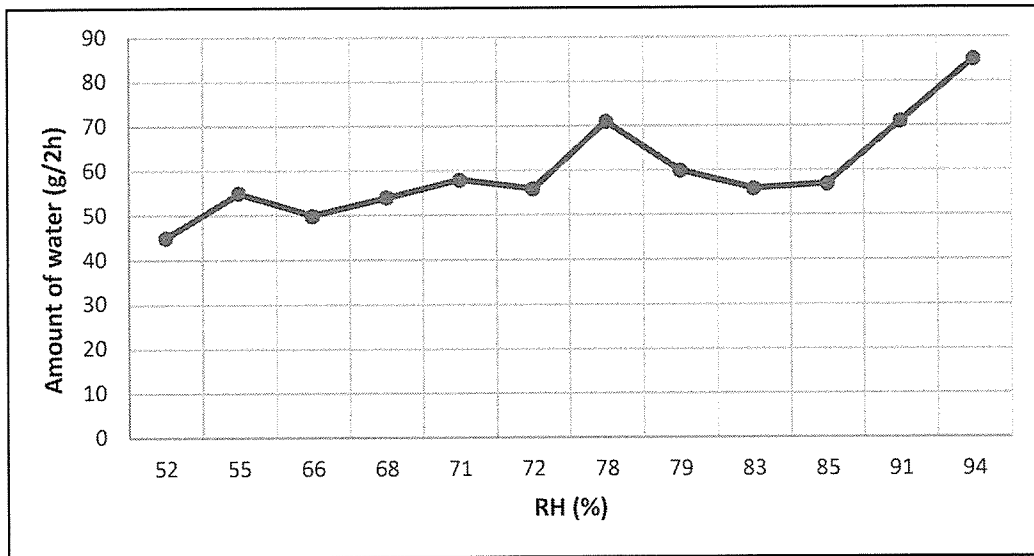
Figure 4.4: Relation between RH and condensation rate

According to the above results, it can be clearly noted that the main parameters affecting the condensation process are the air temperature and RH. The condensation rate, dew point, and surface temperature increase when these parameters are increased.

Based on the measured values in Table 4.1, some calculations were made on these values to determine the amount of heat received by the condensation system, the amount of heat rejected from the condensation process, and the amount of Peltier heat, as a thermoelectric collar was used for condensation. Furthermore, the percentage of error in the calculated values was determined. Records with errors greater than 8% were neglected. Table 4.2 presents the calculated values.

Table 4.2: Experimentally calculated values of received heat, rejected heat, Peltier heat, and error percentage of two hours running time

Cooling surface temp (°C)	Air temp (°C)	RH (%)	Amount of water (g)	QReceived (W)	QRejected (W)	QPeltier (W)	Error (%)
21.2	32.4	83	56	278.6	142.7	4.7	0.8706
20.9	31.6	94	85	320	163	5.2	1.2333
21.2	32.3	91	71	311.2	157	4.9	2.2559
22.3	35.4	71	58	247.9	133	4.7	3.2387
23.2	37.2	85	57	293	149	4.8	1.4785
23.7	38.9	55	55	206.3	123.1	4.8	12.2932
23.0	39.2	52	45	192.4	122.7	4.6	17.8442
22.2	34.7	66	50	233.4	127.5	4.9	4.6561
20.3	33.0	72	56	249	136.7	5	5.2813
19.2	32.9	68	54	228.7	131.1	5.1	8.8758
20.9	32.7	79	60	267.4	139.7	5	0.6806
20.1	32.1	78	71	264.3	137.1	4.6	0.2423

To better understand the relation between the calculated values and the measured parameters throughout the experimental work, a number of plots were created.

Figure 4.5 shows the relation between the received heat and the condensation rate. There is a proportional relation between the two parameters.
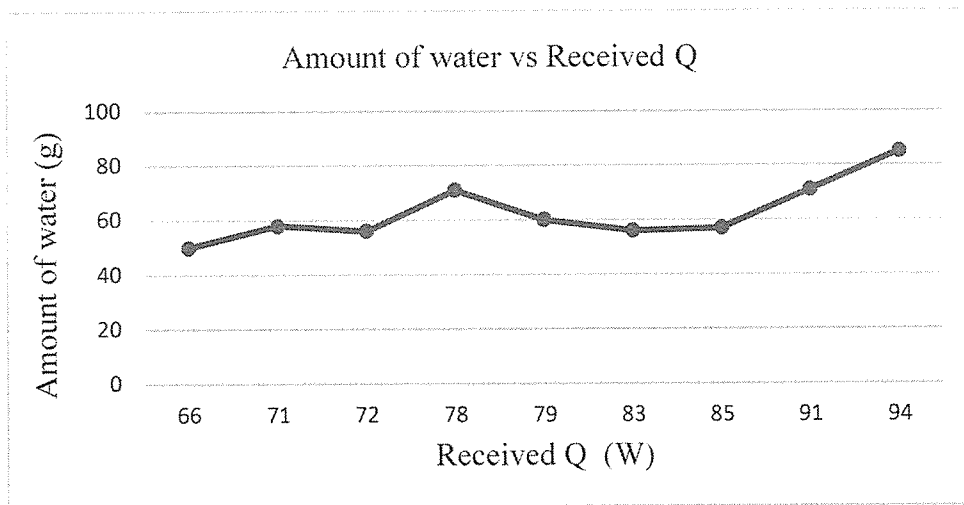
Figure 4.5: Relation between received heat and condensation rate

The amount of heat rejected from the system increased as the condensation rate increased. As more heat is rejected, more water vapor is cooled and converted to water. This property is also proportional to the air temperature, cooling surface temperature, and dew point as shown in Figure 4.6.
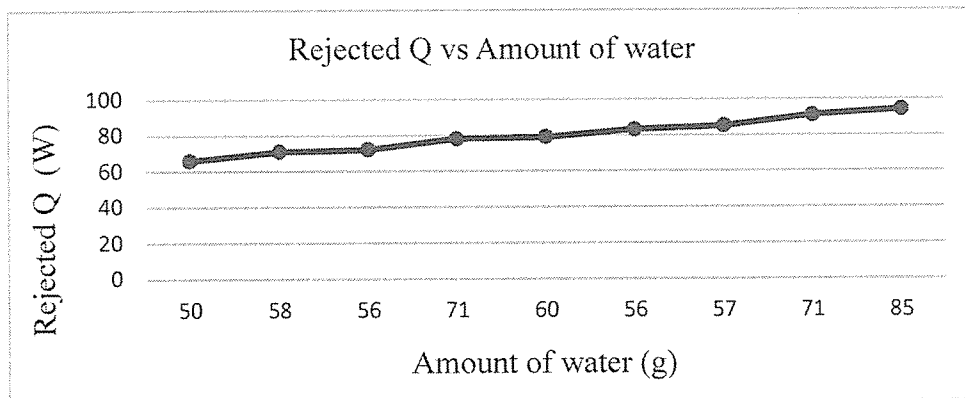
Figure 4.6: Relation between rejected heat and condensation rate

The same analysis of rejected heat by a plate heat exchanger for water extraction from air by condensation was conducted by Saraireh (2012), as shown in Figure 4.7.

61
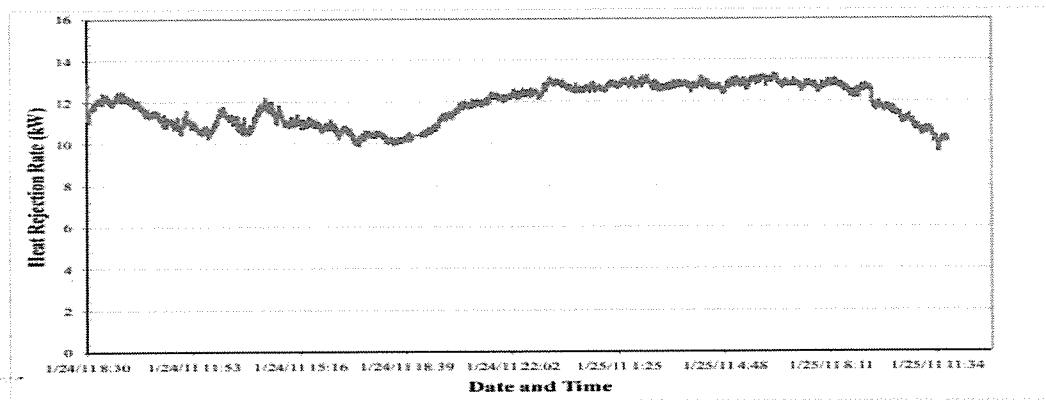
Figure 4.7: Heat rejected by polypropylene compact heat exchanger (Saraireh, 2012)

Figure 4.8 shows the results of the water condensation vs. the RH based on the experimental results. The amount of condensed water increases as the humidity increases, but at some points (e.g., where the humidity was 72%), there was a reduction in the amount of water when a high temperature was introduced. This means that the dew point increased.
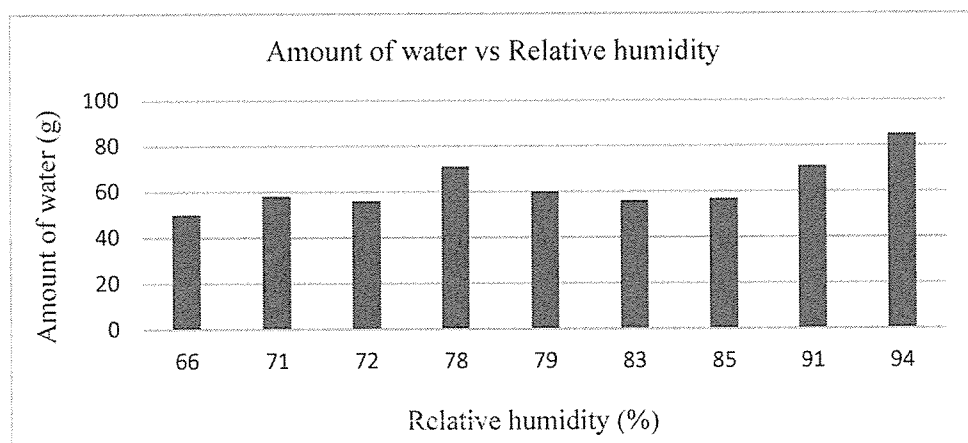
Figure 4.8: Water condensation according to experimental results vs. RH

4.2 Controlled condition

As illustrated in Chapter 3, as you see in Figures 4.9, 4.10 and 4.11 a second experiment was performed under controlled conditions where the temperature was fixed at a value of 40 °C with 85% humidity and water was collected and measured.
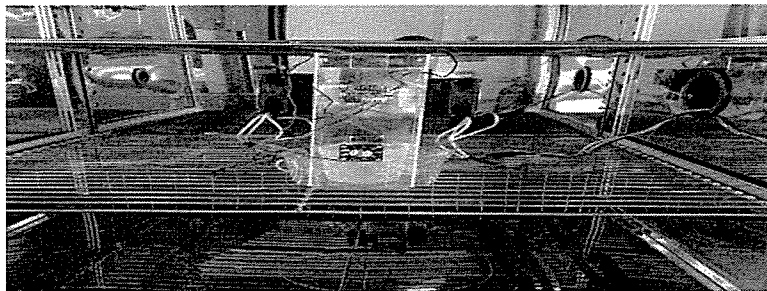
Figure 4.9: Humidity Chamber test
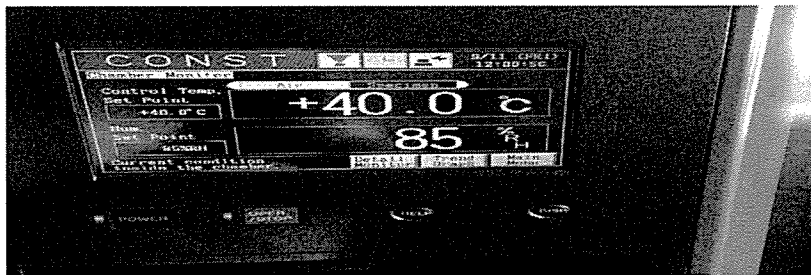
Figure 4.10: Chamber control panel

Figure 4.11: Collected water

Similar measurements were made for the working hours, cooling surface temperature, air temperature, humidity, and amount of collected water under these specified conditions. The results are presented Table 4.3.

Table 4.3: Controlled condition results

Trials	Working hours	Cooling surface temperature (°C)	Air temperature (°C)	Humidity (%)	Collected water (g)
1	0–2	30.6	40	85	95
2	2–4	30.8	40	85	100
3	4–6	30.8	40	85	100
4	6–8	30.9	40	85	110
				Total	405

A greater amount of water was generated under this condition, which means that the unit gained high efficiency at 40 °C and 85% humidity. Compared to the first condition, this condition generated more water. The overall amount of water produced within 8 h was 405 g, which was more than that under the first condition, which was 715 g within 24 hours, owing to improvements in the efficiency of the device, Figure 4.12 shows the amount of water collected during specified working hours.
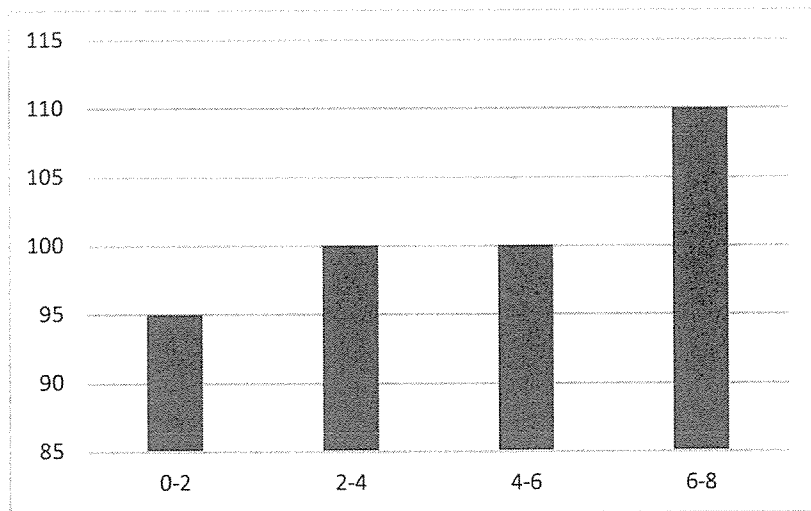
Figure 4.12: Amount of collected water

4.3   New concept

The water harvester is a developed version of the old device from my undergrads level.

The main development is size of the device, Figures 4.13, 4.14 shows the old device and the new device.
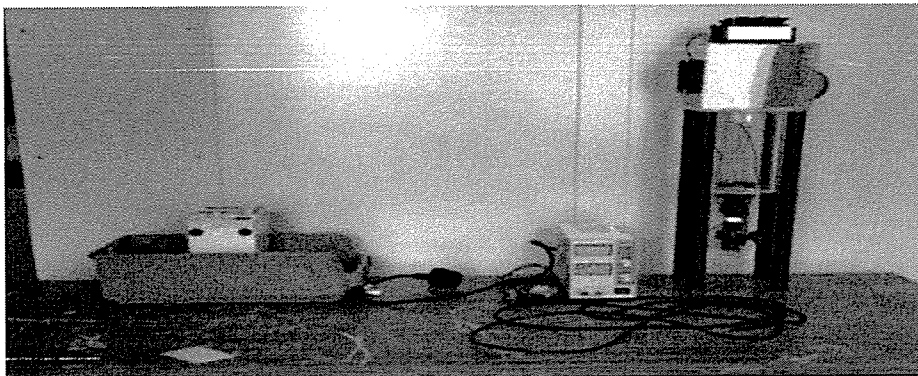
Figure 4.13: Old water harvester device
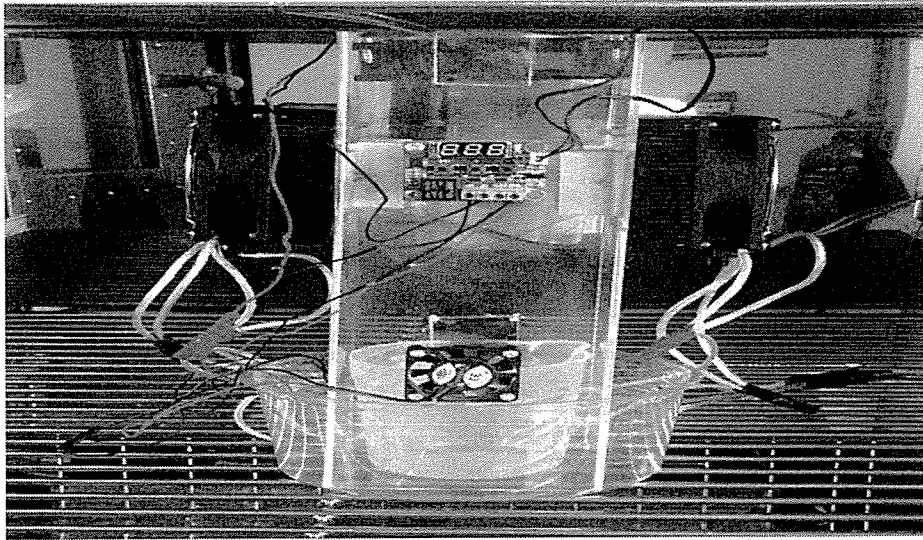
Figure 4.14: Developed water harvester device

Power consumption was 34 Watt in the old device with only one thermoelectic, but in the new device 2 thermoelectrics uses, each one consume only 5 Watt which is considerably low. There is an increasment in extraction of water with less consumtion of power.

The most important improvement is the amount of water collected, the new device collected 405 g, while the olde device in same condition collected only 88 g.

Moreover, the new device has a termostat to control the air flow where the old device didn't have any control mechanism.

The new device is portable while the old device was huge and heavy and also consume more energy which need a power supply to operate, but the new device works with solar power and battery, the development of old device is summarized in Table 4.4.

Table 4.4: Comparison between the old device and the new device

	Old Machine	New Machine
Size	150 mm x 150 mm x 700mm	100 mm x 100 mm x 300mm
Power consumption	23W	35W
Controllers	No	Thermostat/DC-DC Digital Controller
Renewable energy	Power supply	Solar panel/ Battery/Power supply
Portable	No	Yes
Operation environment	climate chamber	Actual weather and climate chamber
Efficiency	Less efficient	360.2% More efficient
Produced water	88g/8h	405g/8h

Chapter 5. Numerical analysis and results

5.1 Overview

The second method of analysis was a numerical method. In this method, CAD geometry was built for the suggested model using SolidWorks software. The model was imported to ANSYS software to simulate it under boundary conditions of inlet air temperature, cooling surface temperature, and RH. The boundary conditions in the ANSYS software are defined in the following sections. Note that the flow rate was assumed to be 52.04 CFM according to the specifications of the fans used in the experiment.

5.2 Model preparation

SolidWorks software was used to build a three-dimensional geometry for the proposed Water Harvester device based on the defined specifications in Chapter 3. The final assembly created by the SolidWorks software is presented in the Figure 5.1.
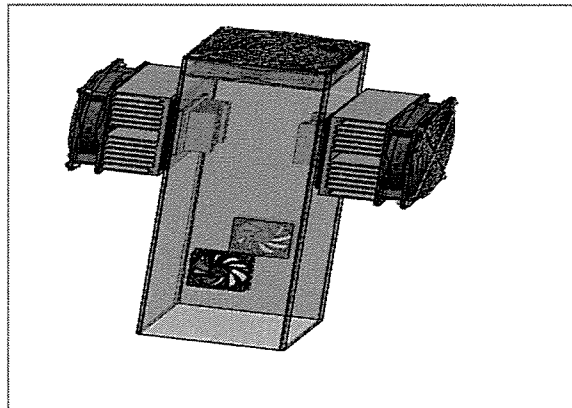
Figure 5.1: CAD model for tested prototype

5.3 Basic assumptions for numerical model

The main assumptions in this analysis are as follows:

- Three-dimensional analysis where the outlets, inlets, and cooling surface were not aligned in one plane, so the analysis was assumed to be three-dimensional

- The energy equation was implemented in the analysis, where the condensation process occurred by the heat transfer between the cooling surface and the inlet air.

- The fins and design walls had a rectangular geometry, so the Cartesian coordinate system (x, y, and z) was used.

- The flow was assumed to be Newtonian fluid, where air and water are Newtonian fluids

- The effect of gravity was considered, with the gravity effect in the vertical direction only

- The flow was considered unsteady according to physical changes in the flow properties

- The flow was considered to be fully turbulent according to the calculations of the Reynolds number. In addition, the flow was assumed to be incompressible flow.

- A K-ε model was used to simulate the flow, where the values of K and ε are shown in the boundary conditions Table 5.3. Treatment near the wall was assumed to be realizable wall treatment. The realizable wall treatment considered changes in the turbulent viscosity.

- The inlet air was modeled as a mixture fluid. This mixture included two materials (water vapor and dry air), and the humidity ratio was used to specify the ratio of water vapor in the inlet air. An injection model was created for 7200 s (2 h) to be similar to the experimental time, where the water vapor was defined as H_2O.

- The temperature distribution at the inlet region was assumed to be constant.

69

5.3.1 Model analysis

The prepared model using SolidWorks software was imported to ANSYS to test the condensation of the humid air under actual and controlled conditions. In ANSYS, the volume of the fluid was created to define the fluid domain. A mesh was generated for the exported model in which the model was separated into very fine areas to simplify the simulation and to maintain an accurate result. For this purpose, ANSYS ICEM was used.

ANSYS ICEM CFD is one of the available proprietary software packages in the ANSYS software. This package provides advanced geometry/mesh generation, mesh diagnostics, and repair functions applicable to in-depth analyses. A wide range of studies have used this package because it can precisely produce computational grids for complex geometries and configurations. The created mesh for the prepared model is presented in Figures 5.2, 5.3.
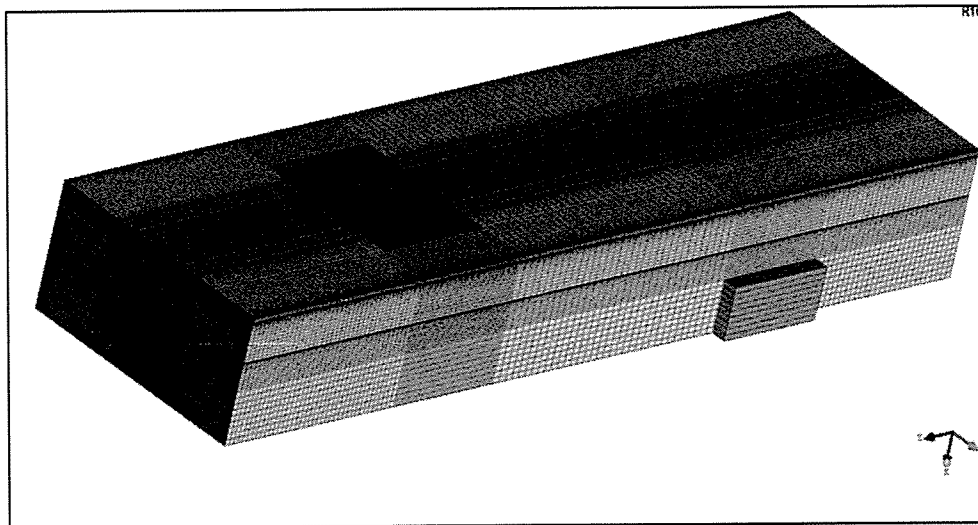
Figure 5.2: Created ICEM mesh for proposed model
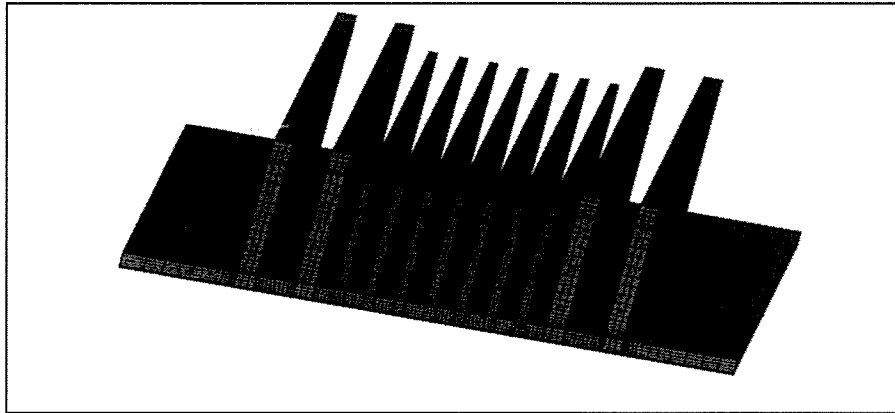
Figure 5.3: Created mesh of cooling surface

The above ICEM mesh comprises different element types in Table 5.1.

Table 5.1: Different element types

NODE	LINE_2	HEXA_8	QUAD_4
114	1784	1867782	143958

The number of mesh elements for the device parts is presented Table 5.2.

Table 5.2: Number of elements for generated mesh

Part	Number of elements
Fins	37149
Inlet	10945
Outlet	522
Solid	1867782
Symmetry	36423
Walls	58919
Total elements	2013638
Total nodes	1939960

The boundary conditions that were defined in the prepared model are presented in Table 5.3. The inlet velocity depends on the flow rate provided by the fan, which is 52 CFM. The velocity according to the inlet section area was found to be 4.1 m/s.

Table 5.3: Boundary conditions

	U (m/s)	V (m/s)	W (m/s)	T (°C)	RH (%)	k	ε
Inlet	4.1	0.0	0.0	40	85	0.00632	0.17179
Cooling surface	0.0	0.0	0.0	30.6	100	Wall function	Wall function
Walls	0.0	0.0	0.0	Wall function	Wall function	Wall function	Wall function
Outlet	Fully developed	Fully developed	Fully developed	Fully developed	Fully developed	Fully developed	Fully developed

The turbulence intensity (I) is a function of R_e. This can be defined as $0.16Re^{-1/8}$, where R_e is calculated based on the hydraulic diameter (D_h) and the kinematic viscosity. R_e in this case is 1.26×10^5 at a kinematic viscosity of 1.65×10^{-5} m²/s. Then, the turbulence intensity for this case is 0.17179. $k = \frac{3}{2}(UI)^2$ and $\varepsilon = \frac{k^{\frac{3}{2}}}{l}$ can be calculated by using the value of the turbulence intensity.

5.3.2   Numerical modeling results

The results were obtained after approximately 1621 iterations and were converged to 1×10^{-6} residuals. It is worth mentioning that the pressure gradient was treated using a second-order upward model. This part presents the results obtained from the model

72

that was prepared for the condensation of a humid air system in SolidWorks and simulated using ANSYS software. The results of a numerical simulation in the ANSYS software are shown below for the mass fraction of the air and water over the condensation surface, amount of water over the condensation surface (numerical simulation), distribution of surface temperature, and air velocity distribution. The results are presented as contour plots and graphs.

5.3.3 Results for testing conditions

The simulation was carried out where the temperature was constant at a value of 40 °C with a humidity of 85% for 8 hours in climate chamber. For the vertical flow of air, Figure 5.4 shows the results of the water mass fraction under this condition. It can be noted that a higher water concentration at the lower side of the fins. This high amount and closeness to the other readings indicate that condensation occurred, and the cooling surface is wet. The distribution of water over the surface is defined by different colors. The maximum value is given by a red color which is 98.7%, which means that 98.7 % of the surface is wet. The mass fraction of the water was higher at the middle section which has the lowest temperature, where less air circulation at the center of the fins, so the mass fraction of air at the middle also is low and water fraction is high.
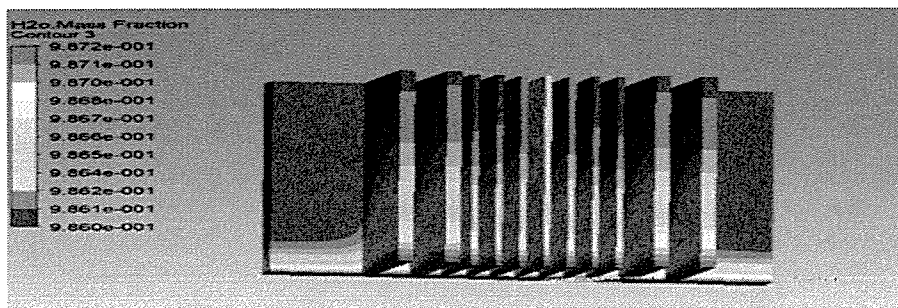
Figure 5.4: Mass fraction of water

Markatos (2015) utilized a CFD analysis to measure the humidity formation on all surfaces for two dissimilar initial humidity conditions in real time for 100 s. The results are presented in Figures 5.5, 5.6, which shows the numerically analyzed water-vapor condensation by means of a flow-oriented scheme.
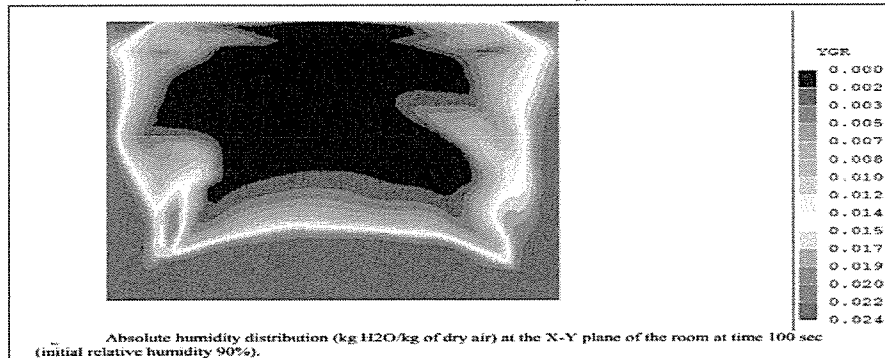
Figure 5.5: Numerical results of Markatos (2015)
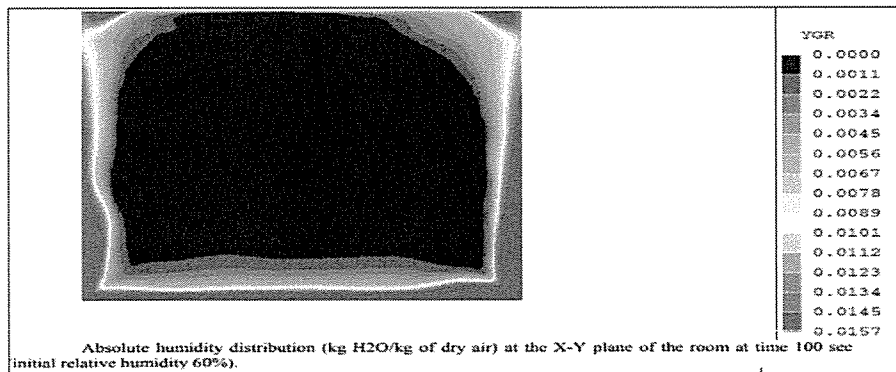
Figure 5.6: Numerical results of Markatos (2015)

Figure 5.7 below demonstrates the distribution of mass fraction of air over the model surface as obtained by the numerical simulation. As shown in the Figure 5.9, the results are presented as a contour plot where the maximum mass fraction of air is presented by a red color with a value of 1.4%. This value gives indication to that majority of the humid air amount was condensed to water. Since the flow is vertical,

74

the higher concentration of air is at the upper side. The temperature at the middle section has lowest value because less air in circulation in this region comparing with other sides, so the sides has higher temperature according to air circulation especially the sides are closer to the outlet suction fans.
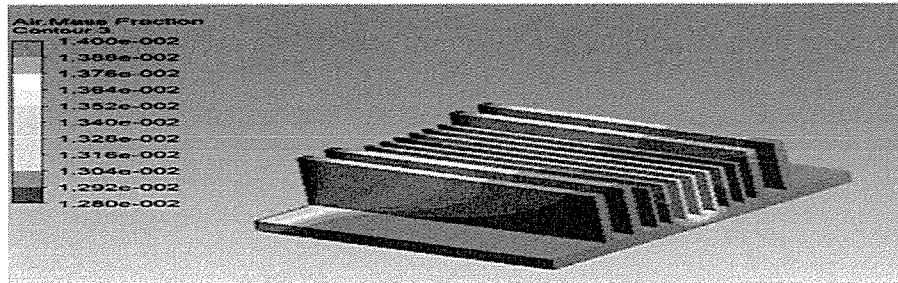
Figure 5.7: Mass fraction of air for second condition

The distribution of the temperature at the surface under the controlled condition is presented in Figure 5.8. It is clear that the temperature decreases from the inlet to the outlet owing to the occurrence of condensation. Minimum values were observed at the middle of the model at a temperature of 307.3 K.
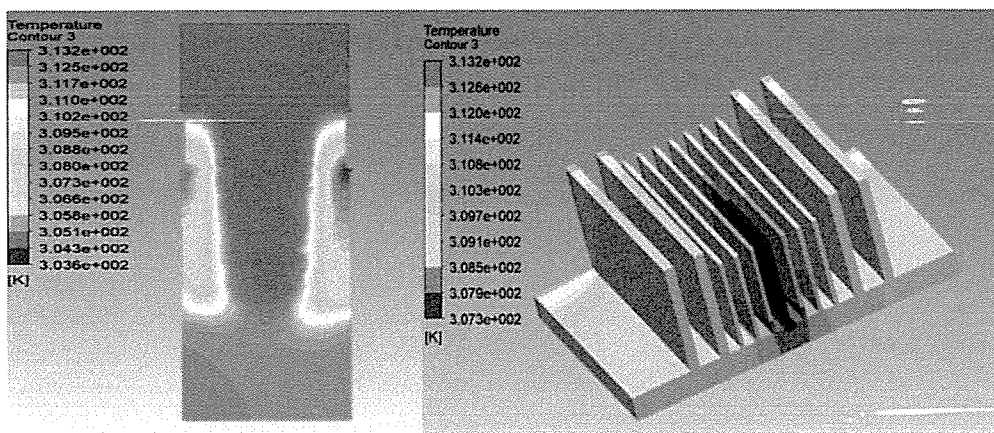
Figure 5.8: Side views of temperature distribution

The amount of water produced by the conditional experiment was 405 g/8 h. According to the numerical analysis, this amount or 437.76 g/8 h.

Velocity distribution at inlet flow rate of 52 CFM. The following set of contour plots defines the distribution of the air velocity over the condensation surface in difference directions. From Figure 5.9, it is clear that the maximum air velocity is 3.712 m/s and the velocity at the condensation walls is zero. This means that these walls are fully wetted by a layer of condensed water. The maximum velocities in the z-, x-, and y-directions are 1.563 m/s, 3.221 m/s, and 1.820 m/s, respectively.
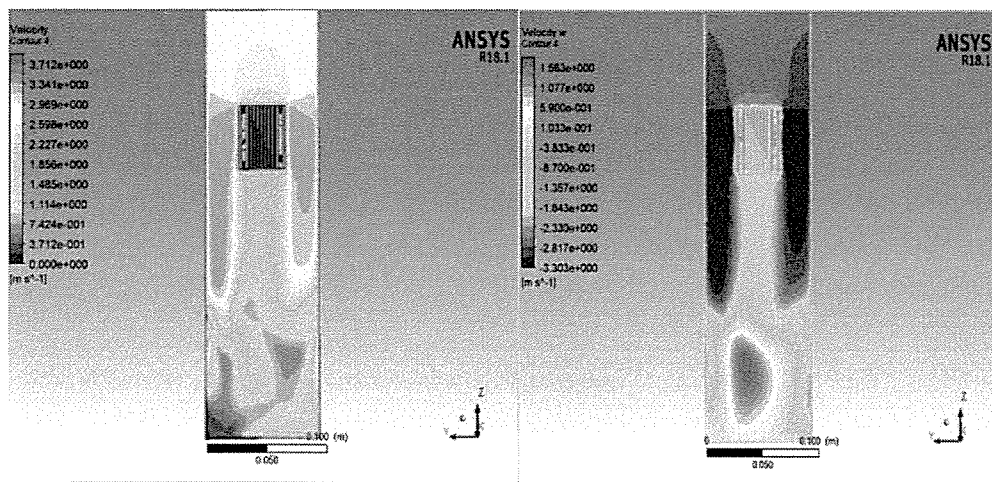
Figure 5.9: Velocity distribution along the model

5.4   Discussion

This section discusses the results obtained from the performed tasks in the previous chapters including the experimental analysis, theoretical analysis, and numerical analysis of water condensation from humid air. Different results were obtained from these methods; however, all of the results indicate the amount of water that can be generated from condensing air. From the experimental analysis, an evaluation of the initial and boundary conditions required for the numerical analyses was performed.

The measured values for the experiments include the number of working hours, time of day, cooling surface temperature (°C), air temperature (°C), RH%, amount of water (g), and dew point. The relations between these measured values are graphically presented to understand how changing these values affects the amount of produced water.

For the numerical analysis, the prepared model in SolidWorks software for the condensation of humid air with a thermoelectric cooler was simulated using ANSYS software to determine the mass fractions of water and air over the condensation surface, the amount of produced water against the RH, and the change in the Sherwood number as the Reynolds number changed.

In the first method of analysis, which was the experimental analysis, the initial and boundary conditions needed to complete the additional two types of analysis were evaluated. The evaluated parameters in this analysis involved measurements of the cooling surface temperature (°C), air temperature (°C), RH%, amount of water (g), and dew point at different working hours and times of day.

A number of plots were produced to examine the relation between these values to show how the amount of produced water changed when one or more of these parameters was changed. From the plots, it was observed that:

- Increasing the RH of air resulted in a considerable increase in the amount of condensed water.
- The air temperature when the humidity was 68% was less than the air temperature at 66% humidity.
- There is a proportional relation between the condensation rates per 2 h and the temperature difference. The maximum condensation was achieved at a temperature difference of approximately 9.61 °C and a value of 85 (g/2 h).
- There is a proportional relation between the cooling surface temperature and the air temperature: the cooling surface temperature increased as the air temperature increased. At a maximum air temperature of 39.2 °C, a maximum cooling surface temperature of 23 °C was obtained.

- Increasing the RH of air from 52 to 94% resulted in a proportional increase in the condensation rate of water from this air. The maximum amount of produced water was measured as 85 g at a maximum RH of 94%.

- By calculating the amounts of heat received by the condensation system, the amount of heat rejected from the condensation process and the amount of Peltier heat as a thermoelectric collar was used for condensation. It was found that the amount of heat rejected from the system increased as the condensation rate increased. As more heat was rejected, more water vapor was cooled and converted to water.

In the second method of analysis, which was the theoretical method, equations for analyses of the fins and the condensation of humid air were solved using code written for the MATLAB software. The obtained results from running the code written for the fin analysis involved the temperature and temperature difference of 11 fins in addition to their efficiencies for dry and wet surfaces.

As a result, a higher temperature was measured for the first fin, with a value of approximately 279.7 K. This temperature gradually increased for the following fins until it reached a minimum temperature of 275.7 K for fin number 8. In addition, fin number 8 showed a higher temperature difference of 18 K. This was because of its lower base temperature compared to the other fins. In term of fin efficiency, for the dry surface condition, the efficiencies of the 11 fins were simulated. The results showed that the efficiency increased for fins 1 to 8 and then experienced a slight reduction for fins 9, 10, and 11. The maximum efficiency observed for fin number 8 was approximately 87%.

For a wet surface of the fin, a constant efficiency of 73% was observed for fins 1 and 2. This value increased to 76.3% for fins 3 to 9. After that, the value decreased to 73% for fins 10 and 11.

The MATLAB simulation for the condensation process provided an indication of the relation between different dimensionless numbers such as the Reynolds number and Sherwood number for natural convection, forced convection, and mixed convection;

the Grashof number and Nusselt number for free convection; and the Reynolds number and Nusselt number for forced and mixed convection.

The obtained results showed that:

- For natural convection, the Sherwood number is a function of the Reynolds number and increased as the Reynolds number increased. The maximum amount of convection mass transfer (Sherwood number) that took place at the surface was 1.742, which was obtained at a Reynolds number of 2.104×10^4.

- For forced convection, the maximum amount of mass transfer that occurred at the surface (Sherwood number) was approximately 18.97, which was obtained at the same Reynolds number of 2.104×10^4.

- For mixed convection, the maximum value of the Sherwood number (22.72) was obtained at a Reynolds number of 2.104×10^4.

- For lower values of the Grashof number, a slight increase in the average Nusselt number was observed. This resulted from the low thermal gradients and predominance of the conduction regime. When the value of Gr was raised, a quick increase in the Nusselt number was observed until it reached a maximum value of 2.224.

- For forced convection, the Nusselt number increased as the Reynolds number increased. This means that the Nusselt number for turbulent flow is higher than that for laminar flow.

- For mixed convection, the Nusselt number increased linearly as the Reynolds number increased. A maximum Nusselt number of 79.7 was observed at a Reynolds number of 2.104×10^4.

In the third type of analysis, which was the numerical analysis, a model was prepared using SolidWorks software for a system that condensed humid air with a thermoelectric cooler. This model was simulated under two conditions using the ANSYS software to determine the mass fractions of water and air over the condensation surface and the amount of produced water against the RH.

79

The obtained results under actual conditions showed that the maximum value of the water fraction over the surface was measured as 98.7%. This indicated that 98.7% of the surface was wet. However, the maximum mass fraction of air was measured as only 1.4%. This indicated that a very high amount of humid air was converted to water. Increasing the inlet temperature resulted in an increase in the condensation surface temperature. The flow of air was vertical, so the temperature decreased from the inlet to the outlet. The inlet temperature was selected as 313 K with a humidity of 85%. This result showed a greater amount of water owing to the improved efficiency of the water harvester device. The condensation surface temperature in this case was measured as 303 K.

Figure 5.10 shows a comparison of the amount of water under controlled conditions. The difference between the experimental and numerical results was approximately 30 g/8 h.
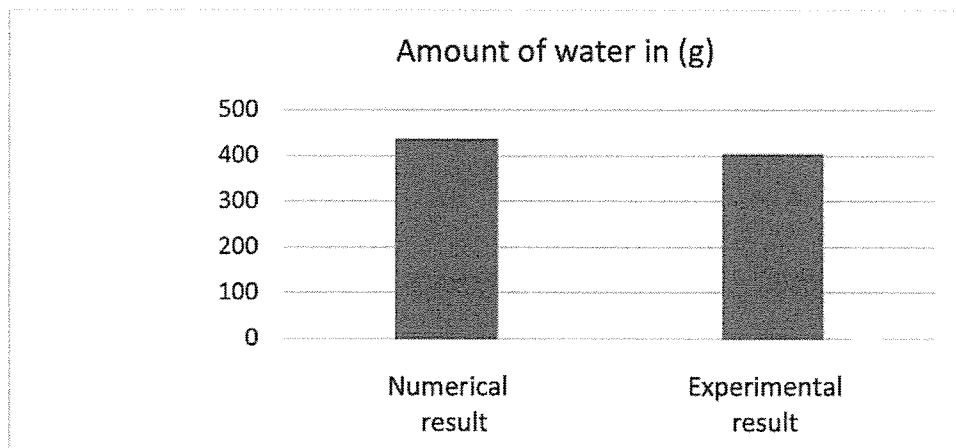

Figure 5.10: Comparison between numerical result and controlled condition result for amount of water in 8 hours over condensation surface

Chapter 6 . Conclusion

Sources of water are increasingly unable to meet the needs of humans and industries. This inspires us to search for other sustainable sources of water. One of these sustainable, renewable, and clean sources is atmospheric air. Several studies have shown that atmospheric air includes a significant amount of water vapor that can be converted to freshwater by using several techniques. Among the many available techniques, the extraction of water from air by the condensation process by using thermoelectric coolers was selected to be analyzed in this study. The goal of this study was to perform experimental, theoretical, and numerical analyses to estimate the amount of water that can be extracted from humid air using the specified technique, in addition to evaluating the factors that affect the amount of extracted water.

To achieve the intended aim of this study within a specified time period and in a successful manner, the study was divided into a number of tasks. Each task was related to the study objectives. Each of these tasks was accomplished within a separate chapter.

Chapter 1 provided a general introduction to the problem of water shortages, the amount of water available in atmospheric air, the climate conditions to be considered before extracting the water, and generally used techniques for water extraction from air. From this chapter, the overall idea of the study could be understood. The overall aim, objectives, and significance of this study were defined in this chapter.

All of the provided data in Chapter 1 was expanded upon in Chapter 2. This chapter was a literature review that involved data collected from previous studies regarding their methods of water extraction from air. Also reviewed were water vapor condensation models provided in the studies of different authors. It was found in this chapter that there is a wide range of techniques used for water extraction from air. The principles and layouts of these techniques were illustrated in this chapter. For condensation process modeling, different experimental, theoretical, and numerical

models were reviewed. Their principles, layouts, and results were reviewed for future comparison with the achieved results of this study.

By analyzing the studies in the literature review chapter, the idea of this study was proposed. The methodology is followed to achieve the proposed idea and is presented in detail in Chapter 3. The study idea of analyzing the condensation process of humid air was proposed to be achieved using theoretical methods, experimental methods, and numerical methods. Each of these methods was discussed separately. The water harvester has been developed to a new concept compared with the old device, which proofed the improvements in terms of the efficiency, power consumption, size and produced water.

By using this apparatus, several parameters could be measured, including the air temperature, cooling surface temperature, RH, and amount of produced water at different working hours and times of day. These values were taken into consideration in the theoretical and numerical analyses.

For the numerical analysis, a CAD model that was similar to the experimental Water Harvester device for water extraction from air which was built using SolidWorks software. This model was imported into ANSYS software to run a simulation by taking the experimental values as the boundary conditions. The model was simulated to measure the mass fractions of water and air on the surface after condensation.

For the experimental analysis results, the values of the cooling surface temperature (℃), air temperature (℃), RH%, amount of water (g), and dew point at different working hours and times of day were measured and recorded. The effects of these parameters on the amount of water produced were estimated by generating plots that related these parameters.

The results of the numerical analysis were also presented in a plot format. The contour plots for the mass fractions of air and water.

Discussion of the results obtained from the two methods of analysis. A comparison of the results showed that the amount of water evaluated by the numerical calculations was closer to the experimental value when compared together.

For future works, the same analysis can be performed for other techniques such as plate heat exchangers to show which technique provides more water from air condensation under the same conditions.

In this device two cooling surface place, it can be increase to four cooling surfaces to increase water condensation. However, it should be noted that power consumption could be an obstacle for future works.

Further research is required to analyze the heat transfer in the aluminum material of the surface under extreme conditions, and to examine the tightness of the built design to eliminate any leakage.

Finally, a computerized controller can be added to the device, and automatically measure dew point and control the cooling surface temperature where can keep it close to the measured air dew point. Therefore, it has the advantage of reduction of power consumption and increases the efficiency of the Water Harvester device.

Acknowledgment

I want to express thanks to my supervisor, Professor Jung, Hyung Ho for his continual support throughout and for guiding me in establishing this thesis. I also want to thank all the people who helped me determine how to implement the experimental and numerical analysis methods. My family and my friends all had a considerable role in supporting me throughout my thesis, a hearty thank you to every one of them.

References

Abualhamayel, H. I., & Gandhidasan, P. (1997). A method of obtaining freshwater from the humid atmosphere. *Desalination, 113*, 51–63.

Alayli, Y., Hadji, N. E., Leblond, J. (1987). A new process for the extraction of water from air. *Desalination, 67*, 227–229.

Aly, S.E. (1989). Humidity water vapour collection by absorption cooling machines. Proc. 4th World IDA Congress on Desalination and Water Reuse, Kuwait, Vol. I, pp. 139–167.

Ambrosini, W. (2008). Comparison and analyses of the condensation benchmark results. The Third European Review Meeting in the Severe Accident Research, Bulgaria, pp. 1–6.

Aristov, Y. I., Tokarev, M. M., Gordeeva, L. G., Snytnikov, V. N., & Parmon, V. N. (1999). New composite sorbents for solar-driven technology of freshwater production from the atmosphere. *Solar Energy, 66*, 165–168.

Beysens, D., & Milimouk, I. (2000). The case for alternative freshwater sources pour-less resources alternatives. *eneau.Se´ cheresse*, 11(4), 1–5.

Çengel, Y. A. (1998). Heat transfer: A practical approach. Boston, Mass: WBC McGraw-Hill.

Çengel, Y. A., & Cimbala, J. M. (2006). Fluid mechanics: Fundamentals and applications. Boston: McGraw-Hill Higher Education.

Colburn, A.P., & Hougen, O.A. (1934). Design of cooler condensers for mixtures of vapours with noncondensing gases. *Industrial and Engineering Chemistry, 26*, 1178–1182.

Condensation and Energy. (1991). Energy conservation in buildings and community systems programme. *International Energy Agency*. Annex 14, Report Annex 14, vol. 1, pp. 1–10.

De Swart, H. E. (2016). The governing equations and the dominant balances of flow in the atmosphere and ocean, *USPC Summerschool*, 1–40.

Dehbi, A. A. (1990). Analytical and experimental investigation of the effects of non-condensable gases on steam condensation under turbulent natural convection conditions. Ph.D. thesis, Massachusetts Institute of Technology, Department of Nuclear Engineering, pp. 1–13.

EL-Sharkawy, I. (2000). Production of water by extraction of atmospheric moisture using solar energy. M.Sc. Thesis, Mansoura University, 1–9.

Elsarrag, E. (2011). Experimental investigations on water recovery from the atmosphere in arid humid regions. CIBSE Technical Symposium, De Montfort University, Leicester, UK.

Gandhidasan, P., & Abualhamayel, H. I. (2005). Modeling and testing of a dew collection system. *Desalination, 180*, 47–51.

Gerald, R. (2009). The k-ε turbulence model. [Online] Available at http://web.cecs.pdx.edu/~gerry/class/ME448/notes_2012/pdf/keModel.pdf

Hamed, A., Gad, H. E. M., & El-Sharkawy, I. (2001). Application of a solar desiccant/collector system for water recovery from atmospheric air. *Renewable Energy, 22*, 451–556.

Hamed, A. M. (1993). Non-conventional method for collecting water from air using solar energy. Ph.D. Thesis, Russian Academy of Science, pp. 1–12.

Hamed, A. M. (2011). Application of solar energy for recovery of water from atmospheric air in climatic zones of Saudi Arabia. doi:10.4236/nr.2011.21002.

Incropera, F. P., & DeWitt, D. P. (2002). Fundamentals of heat and mass transfer. New York: J. Wiley.

Joshi, V. P, Joshi, V. S., Kothari, H. A., Mahajan, M. D., Chaudhari, M. B., & Sant, K. D. (2017). Experimental investigations on a portable freshwater generator using a thermoelectric cooler. *Energy Procedia, 109*, 161–166.

Kabeel, A. E. (2007). Water production from air using multi-shelves solar glass pyramid system. *Renewable Energy, 32*, 157–72.

Khalil, A. (1993). Dehumidification of atmospheric air as a potential source of freshwater in the UAE. *Desalination, 93*, 587–596.

Kobayashi, M. (1997). A method of obtaining water in arid land. *Solar Energy, 7*, 93–99.

Kuhn, S. Z., Schrock, V. E., & Peterson, P.F. (1997). An investigation of condensation from steam–gas mixtures flowing downward inside a vertical tube. *Nucl. Eng. Des., 177,* 53–69.

Li, J. D. (2013). CFD simulation of water vapour condensation in the presence of non-condensable gas in vertical cylindrical condensers. *International Journal of Heat and Mass Transfer, 57*(2), 708–721.

Liu, S. H., He, W., Songlev, Dengyun, H., Lv, S., Chen, D., Wu, X., Xu, F., & Li, S. (2017). Experimental analysis of a portable atmospheric water generator by thermoelectric cooling method. *Energy Procedia, 142,* 1609–1614.

Magrini, A., Cattani, L., Cartesegna, M., & Magnani, L. (2017). Water production from air conditioning systems: Some evaluations about a sustainable use of resources. *Sustainability*, 9(1309), 1–17.

Martin (2015). The continuity and additional equations. ESCI 342: Atmospheric Dynamics I, Alex DeCaria. pp. 1–8.

Mattheus F. A. G., Shyam S. S., Hilal, H., Charles, P., & Walid, H.S. (2002). Humidification, dehumidification desalination: Seawater greenhouse development, Proc. IDA Conf., Bahrain, pp. 1–15.

Merle, C., David C., & Bassam H. (2011). Mechanics of fluid dynamics. Cengage Learning, 4th edition, ISBN: 978-1-4390-6203-6.

Parekh, S., Farid, M. M., Selman, J. R., & Al-Hallaj, S. (2004). Solar desalination with a humidification–dehumidification technique: A comprehensive technical review. *Desalination, 160(1),* 67–86.

Roy. L., Walter, A., James, B., & Scolt, F. (1989). Carrier gas process: A new desalination and concentration technology, Proc. of the 4th World IDA Congress on Desalination and Water Reuse, Kuwait, Nov. 4–8, Vol. I, pp. 119–138.

Saraireh, M., Li, J. D., & Thorpi, G. (2010). Modeling of heat and mass transfer involving vapour condensation in the presence of non-condensable gasses. 17th Australasian Fluid Mechanics Conference, pp. 1–4.

Shanmugam, G., Jawahar, G. S., Ravindran, S. (2004). Review on the uses of appropriate techniques for arid environment. International Conference on Water Resources and Arid Environment, pp. 1–7.

Sofrata, H. (1981). Non-conventional system for water collection. Proc. of Solar Desalination Workshop, pp. 71–87.

Suryaningsih, S., & Nurhilal, O. (2016). Optimal design of an atmospheric water generator (AWG) based on thermo-electric cooler (TEC) for drought in rural area. Second Padjadjaran International Physics Symposium 2015 (PIPS-2015), pp. 1–7.

Teodosiu, C., Ilie, V., & Teodosiu, R. (2015). Condensation model for application of computational fluid dynamics in buildings. *International Journal of Materials, Mechanics and Manufacturing, 3*(2), 129–132.

Wang, G., Ji, R. Z., &and Li, L. X. (2007). New composite adsorbent for solar-driven freshwater production from the atmosphere. *Desalination, 212,* 176–182.

Wang, L. W., Oliveira, R. G., & Wang, R. Z. (2007). A review on adsorption working pairs for refrigeration. *Science Direct,* 518–534.

Wankhade, A., & Tiwari, H. U. (2016). Extraction of water from air using adsorption refrigeration system. *International Engineering Research Journal (IERJ),* 1069–1074.

Welty, J. R., Wicks, C. E., & Wilson, R. E. (1976). Fundamentals of momentum, heat, and mass transfer. New York: Wiley.

Werner N. G. (1970) Multiple effect humidity process, Proc. of the 3rd Int. Symp. on Freshwater from the Sea, Delyannis, A. and Delyannis, E., (ed.), Vol. 1, pp. 655–668.

White, F. M. (1999). Fluid mechanics. Boston, Mass: WCB/McGraw-Hill.

Winkler, P. M., Vrtala, A., Rudolf, R., Wagner, P. E., Riipinen, I., Vesala, T., Lehtinen, K. E. J., Viisanen, Y., & Kulmala, M. (2006). Condensation of water vapour: Experimental determination of mass and thermal accommodation coefficients. *Journal of Geophysical Research*, *111*, 1–12.

Zheng, Q. R., Pan, Q. Y., Jie, C., & Zhi, H. J. (2011). Preliminary study of extracting water from air utilizing ships waste heat from the cylinder jacket cooling water. *IEEE*, 1632–1636.

Appendix A   : MATLAB codes for theoretical calculations

A.1 Theoretical Calculations for fins (dry conditions)

```
%this code calculates the heat transfer and efficiency of fin for dry

% surface

To_ideal= 273% the ideal base temperature from the specifications

To_measured=[279.7 279.2 278.9 278.8 278.8 278.4 277.9 275.7 276.2 276.5 277.1]

% the measured temperature for each fin where the total number of fins = 11

T_inf = 293.7 % measured for ambient temperature

THETA_Ideal= T_inf-To_ideal% for ideal case

for i=1:11

THETA_MEASURED(i)= T_inf-To_measured(i)

TM(i)=(T_inf+To_measured(i))/2

Beta(i)= 1/TM(i)

if i>2&&i<10

    L=0.015

    t=0.0008

    w=0.046

else

    L=0.018

    t=0.0014

    w=0.046

end
```

p(i)=2*L+2*t

A(i)=p(i)*w

v=14.376-6% this value is the kinetic viscosity at temperature 285 K (table A-5) p. 659

pr= 0.7122% this value is the Prandtl number at temperature 285 K (table A-5) p. 659

k= 0.025049% this value is the thermal conductivity of air at temperature 285 K (table A-5) p. 659

gr(i)=9.81*Beta(i)*(T_inf-To_measured(i))*L^3/v^2% Grashof number

Ra(i)=gr(i)*pr % Raleigh number

Nu(i)=0.825+(0.387*(((Ra(i))^(1/6))))/(1+((0.492/pr)^(9/16)))^(8/29)

h(i)=Nu(i)*k/L

q_ideal(i)=(h(i)*p(i)*k*A(i))^(1/2)*THETA_Ideal

q_actual(i)=(h(i)*p(i)*k*A(i))^(1/2)*THETA_MEASURED(i)

eff(i)=q_actual(i)/q_ideal(i)*100

end

plot(eff)

xlabel('fin#')

ylabel('efficiency(%)')

A.2 Theoretical calculations for fins (wet conditions)

%this code to calculate the heat transfer and efficiency of fin for wet

% surface

To_ideal= 273% the ideal base temperature from the specifications

To_measured=[279.7 279.2 278.9 278.8 278.8 278.4 277.9 275.7 276.2 276.5 277.1]

humdity=0.51

% the measured temperature for each fin where the total number of fins = 11

T_inf = 293.7 % measured for ambient temperature

THETA_Ideal= T_inf-To_ideal% for ideal case

for i=1:11

THETA_MEASURED(i)= T_inf-To_measured(i)

TM(i)=(T_inf+To_measured(i))/2

Beta(i)= 1/TM(i)

if i>2&&i<10

   L=0.015

   t=0.0008

   w=0.046

else

   L=0.018

   t=0.0014

   w=0.046

end

p(i)=2*L+2*t

A(i)=p(i)*w

v=14.376-6% this value is the kinetic viscosity at temperature 285 K(table A-5)pp659

pr= 0.7122% this value is the Prandtl number at temperature 285 K(table A-5)pp659

k= 0.025049% this value is the thermal conductivity of air at temperature 285 K(table A-5)pp659

cpa= 1.00558% this value is the specific of air at temperature 285 K(table A-5)pp659

cpw= 4.19176 %this value is the specific of water at temperature 285 K(12 C)(table A-9)pp606

cifg=cpa*(1-humdity)+cpw*humdity

gr(i)=9.81*Beta(i)*(T_inf-To_measured(i))*L^3/v^2% Grashof number

Ra(i)=gr(i)*pr % Raleigh number

Nu(i)=0.825+(0.387*(((Ra(i))^(1/6))))/(1+((0.492/pr)^(9/16)))^(8/29)

h(i)=Nu(i)*k/L

M(i)=(h(i)*p(i)/(k*A(i))*(1+cifg/cpa))^(0.5)

effm(i)=tanh(M(i)*L)/(M(i)*L)*100

end

plot(effm)

xlabel('fin#')

ylabel('efficiency(%)')

```
%this code to calculate the heat transfer and the efficiency of fin

To_ideal= 273% the ideal base temperature from the specifications

To_measured=[279.7 279.2 278.9 278.8 278.8 278.4 277.9 275.7 276.2 276.5 277.1]

% the measured temperature for each fin where the total number of fins = 11

T_inf = 293.7 % measured for ambient temperature

THETA_Ideal= T_inf-To_ideal% for ideal case

for i=1:11

THETA_MEASURED(i)= T_inf-To_measured(i)

end

plot(THETA_MEASURED)

xlabel('Fin #')

ylabel('theta (K)')
```

```
%this code to calculate the heat transfer and the efficiency of fin

To_ideal= 273% the ideal base temperature from the specifications

To_measured=[279.7 279.2 278.9 278.8 278.8 278.4 277.9 275.7 276.2 276.5 277.1]

% the measured temperature for each fin where the total number of fins = 11

T_inf = 293.7 % measured for ambient temperature

THETA_Ideal= T_inf-To_ideal% for ideal case

for i=1:11

THETA_MEASURED(i)= T_inf-To_measured(i)

end
```

plot(To_measured)

xlabel('Fin #')

ylabel('T(K)')

A.3 Theoretical calculation for condensation

% this code to calculate the NU and Sh numbers according to the experimental

% data, where the temperatures and humidity are defined below, also, the

% experimental data with high error was neglected

ti1=[34.7 35.4 33 32.1 32.7 32.4 37.2 32.3 31.6]

% the inlet temperature C

Ti=273+ti1% the inlet temperature k

humidity =[66 71 72 78 79 83 85 91 94]

tc=[22.2 22.3 20.3 20.1 20.9 21.2 23.2 21.2 20.9]% temperature at condensation surface C

Tc=273+tc% temperature at condensation surface K

wvp=[41.51 43.16 37.3 35.86 36.82 36.34 47.62 36.18 34.9]% water vapour pressure

%(torr)tabulated   can   be   found   also   at
http://www.wiredchemist.com/chemistry/data/vapour-pressure

wvp2=0.00131578947*wvp.*(humidity/100) % water vapor pressure (atm)

%where 1 torr = 0.00131578947 atm, where the humidity was taken

wvpc=[20.06 20.19 17.86 17.62 18.58 18.92 21.36 18.92 18.58]

wvpc2= 0.00131578947*wvpc% water vapor pressure (atm) where 1 torr = 0.00131578947 atm,

%where the humidity was taken 100% at surface (fully wetted)

air_flow=52.04 % cfm

air_flow_si= 0.0245 % converted to m^3/s

d=0.04 % diameter of fan

v=0.0245/(22/7*d^2/4)

vk=[1.67E-05 1.68E-05 1.66E-05 1.65E-05 1.65E-05 1.65E-05 1.70E-05 1.65E-05 1.64E-05]

% the kinematic viscosity (m/s^2) was calculated using interpolation p 659 heat transfer book

L=0.0177 % length of plate

Re= L*v./vk;% Reynolds number

shfor=0.365.*Re.^(0.8).*((vk./2.77).^(1/3))% Sherwood number for forced convection (turbulant flow)

shnat=0.664.*Re.^(0.5).*((vk./2.77).^(1/3))% Sherwood number for natural convection (laminar flow)

shmix=shnat+shfor % mixed Sherwood

moli=wvp2/(0.08205.*Ti);% mole fraction at inlet using ideal gas law

%mole fraction = partial pressure / (universal gas constant * temperature)

molc=wvpc2/(0.08205.*Tc);% mole fraction at inlet using ideal gas law

%mole fraction = partial pressure / (universal gas constant * temperature)

N= shmix.*(2.77/0.018).*(moli-molc)./1000% molar flow rate

% calculating surface area below

for i=1:11

if i>2&&i<10

    L=0.015;

```
    t=0.0008;

    w=0.046;

  p(i)=L+t;

A(i)=p(i)*w;

else

    L=0.018;

    t=0.00014;

    w=0.046;

end

p(i)=L+t;

A(i)=p(i)*w;


end
```

aa=sum(A);% total condensation surface

wa=aa*18*N % theoretical condensation water (kg/s) where 18 is the molar mass of water

%to calculate the Nusselt number for mixed convection should consider

% nu (mix) = nu_free +nu forced as shown in ch 9 (section 9-9) Incropera

% book.

% for natural

TM=(Ti+Tc)/2;% mean temperature

Beta= 1./TM; % this parameter to find Gr number

pr=[7.05922E-01 7.05824E-01 7.06160E-01 7.06286E-01 7.06202E-01 7.06244E-01 7.05572E-01 7.06258E-01 7.06356E-01]

% Pr number was calculated using interpolation p 659 heat transfer book

gr=9.81*Beta.*(Ti-Tc)*0.0180^3./((vk).^2)% Grashof number

Ra=gr.*pr % Raleigh number

Nu_free=0.825+(0.387.*(((Ra).^(1/6))))./((1+((0.492./pr).^(9/16)))).^(8/27))%chuchi lland chu for vertical plate flow

%as shown in ch 9 (section 9-6-1) Incropera

Nu_forced=0.228.*(Re.^0.731).*(pr.^1/3)% Hilpert equation heat transfer book

%using the flow over rectangular vertical plate equation 7.52 and table 7.3

Nu_mix=Nu_free+Nu_forced % using section 9-10 in heat transfer book

Figure(1)

subplot(2,2,1)

scatter(Re,shnat)

lsline

grid on

xlabel('Re')

ylabel('Sh')

title('Re vs sh for natural convection')

subplot(2,2,2)

scatter(Re,shfor)

lsline

grid on

xlabel('Re')

ylabel('Sh')

title('Re vs sh for forced convection')

```
subplot(2,2,3)

scatter(Re,shmix)

lsline

grid on

xlabel('Re')

ylabel('Sh')

title('Re  vs sh for mixed convection')

subplot(2,2,4)

semilogy(Re,shnat,Re,shmix)

grid on

xlabel('Re')

ylabel('Sh')

title('Compare Re  vs sh for free/mixed convection')

legend('sh for natural','sh for mixed')

Figure(2)

subplot(2,2,1)

scatter(gr,Nu_free)

lsline

grid on

xlabel('Gr')

ylabel('Nu')

title('Gr  vs Nu for free convection')

subplot(2,2,2)
```

```matlab
scatter(Re,Nu_forced)
lsline
grid on
xlabel('Re')
ylabel('Nu')
title('Re  vs Nu for forced convection')
subplot(2,2,3)
scatter(Re,Nu_mix)
lsline
grid on
xlabel('Re')
ylabel('Nu')
title('Re  vs Nu for mixed convection')
subplot(2,2,4)
semilogy(Re,Nu_free,Re,Nu_mix)
grid on
xlabel('Re')
ylabel('Nu')
title('Compare Re  vs Nu for free/mixed convection')
legend('Nu for natural','Nu for mixed')
```

Figure (3)

wa_exp=[0.00025 0.000251 0.000251 0.000252 0.000252 0.000253 0.000257
0.000263 0.000264]

Figure (3)

plot(humidity, wa)

xlabel('RH%')

ylabel('water (kg/s)')

title('Water (kg/s) vs RH%')

 % this code to separate the sensible and latent heat\

ti1=[34.7 35.4 33 32.1 32.7 32.4 37.2 32.3 31.6]

% the inlet temperature C

Ti=273+ti1% the inlet temperature k

humidity =[66 71 72 78 79 83 85 91 94]

tc=[22.2 22.3 20.3 20.1 20.9 21.2 23.2 21.2 20.9]% temperature at condensation surface C

Tc=273+tc% temperature at condensation surface K

cp=[1.0060762 1.0060894 1.0060564 1.0060036 1.0060498 1.0065052 1.0062544 1.0062082 1.0064854] % % the specific heat (Kj/Kg) was calculated using interpolation p 659 heat transfer book

heat_ratio=[0.451 0.385 0.372 0.362 0.355 0.48 0.338 0.26 0.249]

% from psychrometric chart, which is shr= qs/qt where qt =(qs+ql), so ql can be written as ql = qs/shr - qs

dT = Ti-Tc

sensble_heat = cp.*dT %qs

latent_heat =(sensble_heat./heat_ratio) -sensble_heat% ql

total=sensble_heat+latent_heat %qt

subplot(2,2,1)

plot(humidity,latent_heat)

101

```
xlabel('humidity (%)')

ylabel('latent heat (w)')

title('latent vs humidity')

subplot(2,2,2)

plot(humidity,sensble_heat)

xlabel('humidity (%)')

ylabel('sensible heat (w)')

title('sensible vs humidity')

subplot(2,2,3)

plot(humidity,ti1)

xlabel('humidity (%)')

ylabel('inlet Temperature (C)')

title('inlet Temperature vs humidity')

subplot(2,2,4)

plot(humidity,tc)
```

A.4: Results of theoretical model

By using the equations presented in Chapter 3 of the theoretical model of water condensation, various parameters were mathematically calculated. These equations refer to the fin and condensation analyses. The experimentally measured values of temperatures in the experimental work were substituted in the given equations. The final equations obtained after substituting these values cannot be solved by hand; thus, MATLAB software was used to solve them via code. The theoretical analysis results are discussed in detail in the following sections.

A.5: Theoretical analysis for fins

The first theoretical calculations were performed to calculate some parameters related to fins, such as the heat transfer and efficiency for a dry surface, heat transfer and efficiency for a wet surface, and heat transfer and efficiency for fins. Code was written in MATLAB for each of these parameters.

The code that defines the heat transfer and efficiency of a fin for a dry surface is provided in the above appendices. Additional code for the fin and condensation analyses are provided in Appendix A.3. Through the MATLAB code, results were provided in the form of plots for the relations between

Temperature and number of fins;

Theta and number of fins;

Efficiency and number of fins for dry surface;

Efficiency and number of fins for wet surface.

The Figure A.1 demonstrates the relation between the measured temperatures for each fin, where the total number of fins is 11. As shown in the Figure, a higher temperature was measured for the first fin with a value of approximately 279.7 K. This temperature gradually increased for the following fins until it reached a minimum temperature of 275.7 for fin number 8. The temperature gain increased for fins 9, 10, and 11. The higher temperature of the first fin is owing to the higher temperature of air at the beginning of condensation.
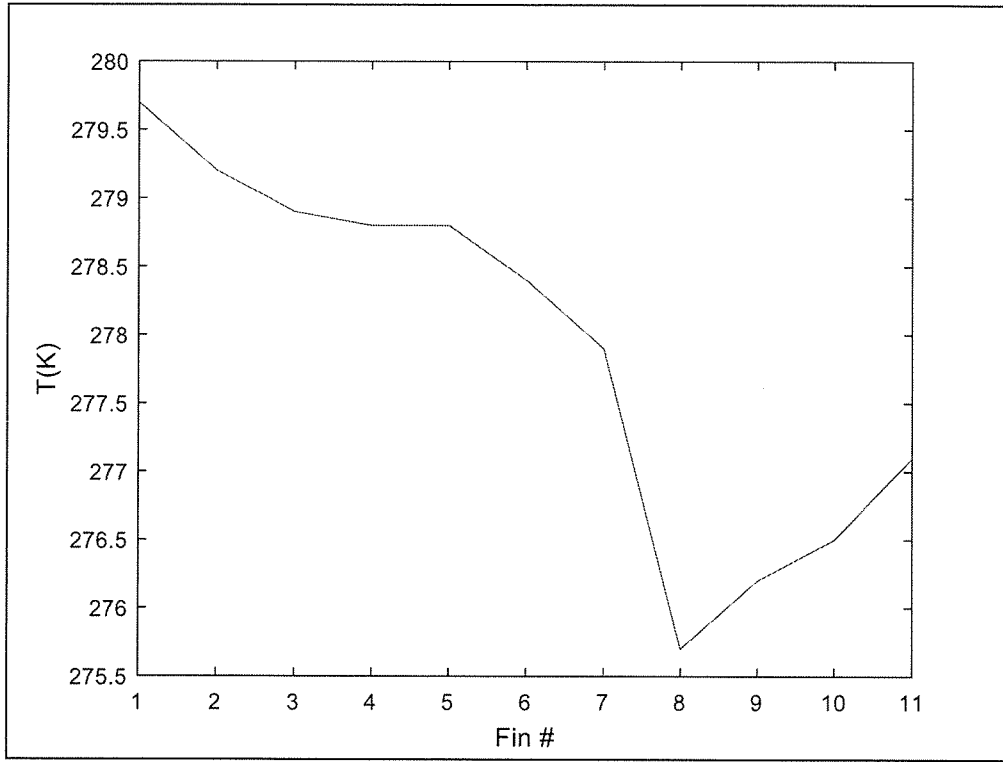
Figure A.1: Measured temperature for 11 fins

The fins are required to remove the energy that was released from the fluid that experienced condensation. For this purpose and in an ideal case, each fin showed a different temperature difference between the ambient temperature and the ideal base temperature. The temperature difference for the fins was defined by theta, as shown in the Figure A.2. From the Figure, fin number 8 showed a higher temperature difference of 18 K owing to its lower base temperature compared to the other fins.
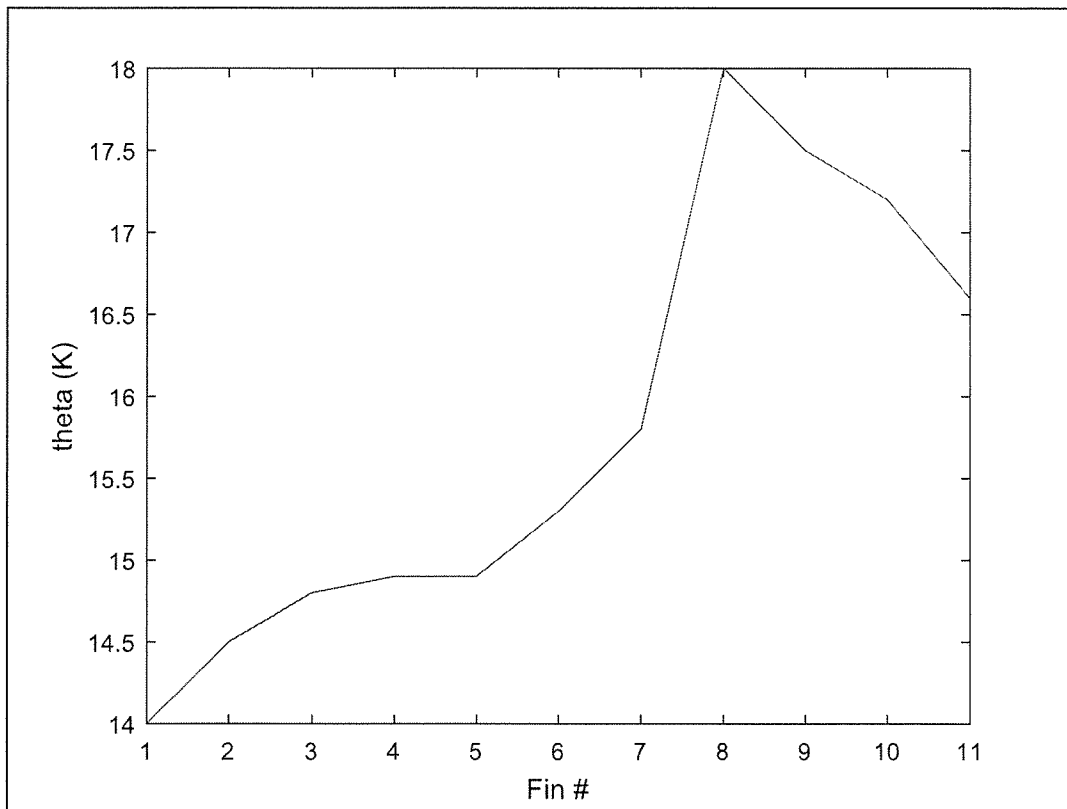
Figure A.2: Temperature difference for each fin

For a dry surface condition, the efficiencies of the 11 fins were simulated in MATLAB, and the results are presented in the following plot. From the plot, the efficiency increased for fins 1–8 and then showed a small decrease for fins 9, 10, and 11. The maximum efficiency observed was that of fin 8, which was approximately 87%.
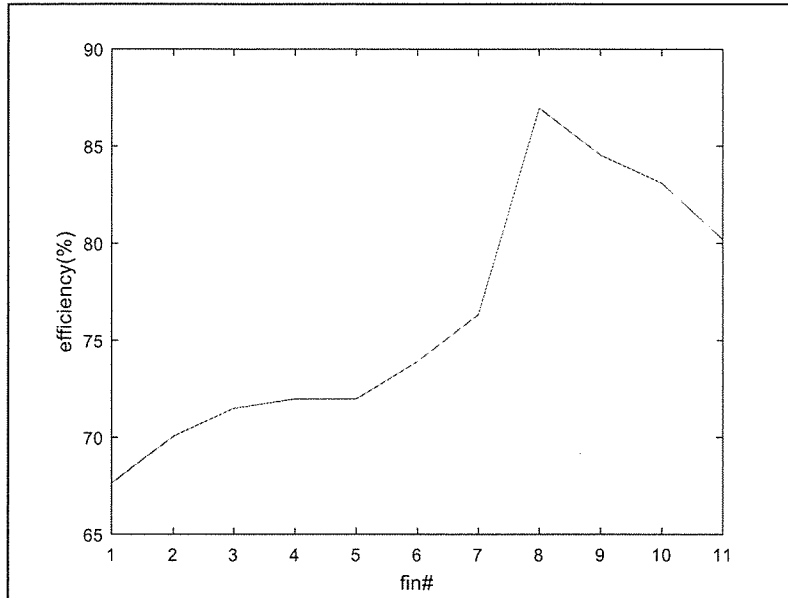
Figure A.3: Efficiency of dry-surface fins

For a wet surface, the efficiency of the 11 fins was measured using MATLAB code. The results are presented in Figure A.4. A constant efficiency of 73% was observed for fins 1 and 2. This value increased to 76.3% for fins 3–9. After that, the value decreased to 73% for fins 10 and 11.
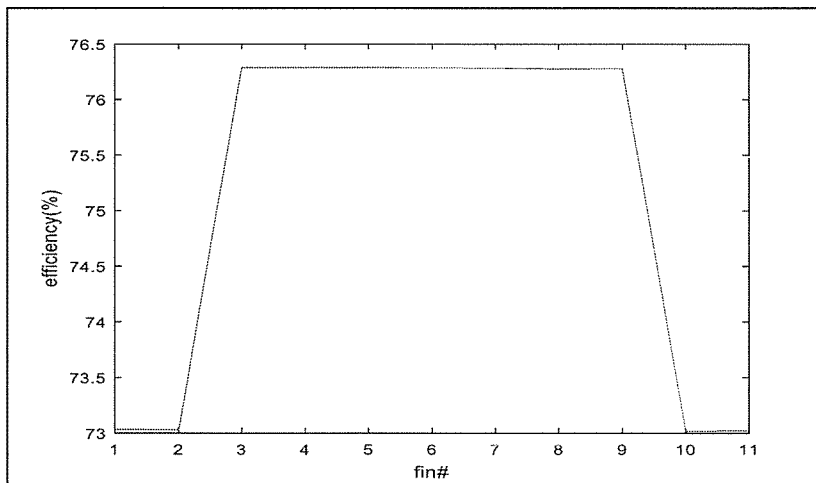

Figure A.4: Efficiency results of 11 fins for wet surface

A.6: Theoretical calculation for condensation

The second part of the theoretical calculation involves equations to solve the condensation process of humid air. These equations were defined in Chapter 3 and were solved using MATLAB software. The code written to solve the condensation of humid air is presented in Appendix A.3. From the code, the relation between the Reynolds number and Sherwood number for natural convection, forced convection, and mixed convection were evaluated.

Using the MATLAB code, the relations between the Grashof number and Nusselt number for free convection, in addition to the Reynolds number and Nusselt number for forces and mixed convection, were evaluated.

The mechanism of heat transfer that occurred throughout the condensation process of the humid air is a convection heat-transfer mechanism. In this mechanism, the heat is transferred via the movement of fluid, which is air in this study. The heat transfer by convection can be forced convection, which is caused by the movement of a fluid because of an external source (a fan in this study). The convection can also be natural convection, in which buoyancy alone is responsible for the fluid motion as the fluid is subjected to heat. This type is caused by density variations because of temperature variations in the fluid. When the two modes of convection occur at the same time, the heat-transfer mechanism is called a mixed-convection heat transfer.

In these mechanisms of convection heat transfer, the fluid motion is governed by a dimensionless group that includes the Reynolds, Grashof, Sherwood, and Nusselt numbers.

The **Reynolds number** is a dimensionless parameter that is utilized in condensation analysis to indicate the flow patterns in various fluid flow cases. When the value of this parameter is low, the flow is said to be a laminar flow, whereas when its value is high, the flow is said to be a turbulent flow. Turbulent flow occurs owing to differences in the speed and direction of the flowing fluid. The value of the Reynolds number also indicates the ratio of the inertial forces to viscous forces within the

flowing air, which is exposed to relative internal movement because of various fluid velocities.

The **Sherwood number** is a dimensionless number that is also known as the mass-transfer Nusselt number. It is usually used in mass-transfer operations to estimate the ratio of the convective mass transfer to the rate of diffusive mass transport.

In this study, theoretical analyses were applied to estimate the relation between these two dimensionless numbers. The Figure A.5 shows the Sherwood number for the average mass-transfer coefficient as a function of the Reynolds number. As described in Chapter 3, the Sherwood number is a function of the Reynolds number and increases as the Reynolds number increases, where a linear relation existed between the two parameters. The maximum amount of convection mass transfer that occurred at the surface was 1.742, which was obtained at a Reynolds number of 2.104×10^4. This result is for natural convection heat transfer.
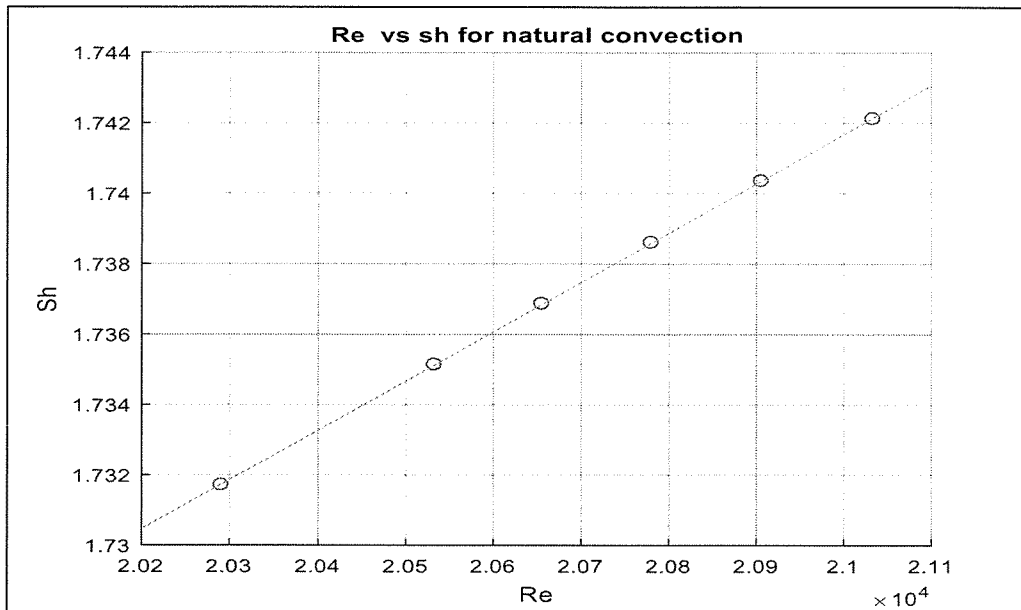
Figure A.5: Sherwood number for average natural mass transfer coefficient as a function of Reynolds number

The Sherwood number for the average forced convection mass-transfer coefficient as a function of the Reynolds number is presented in the following Figure. From the Figure, a linear relation exists between the two parameters for forced convection. The maximum amount of mass transfer that occurs at the surface was approximately 18.97, which was obtained at the same Reynolds number of 2.104×10^4 as with natural convection.
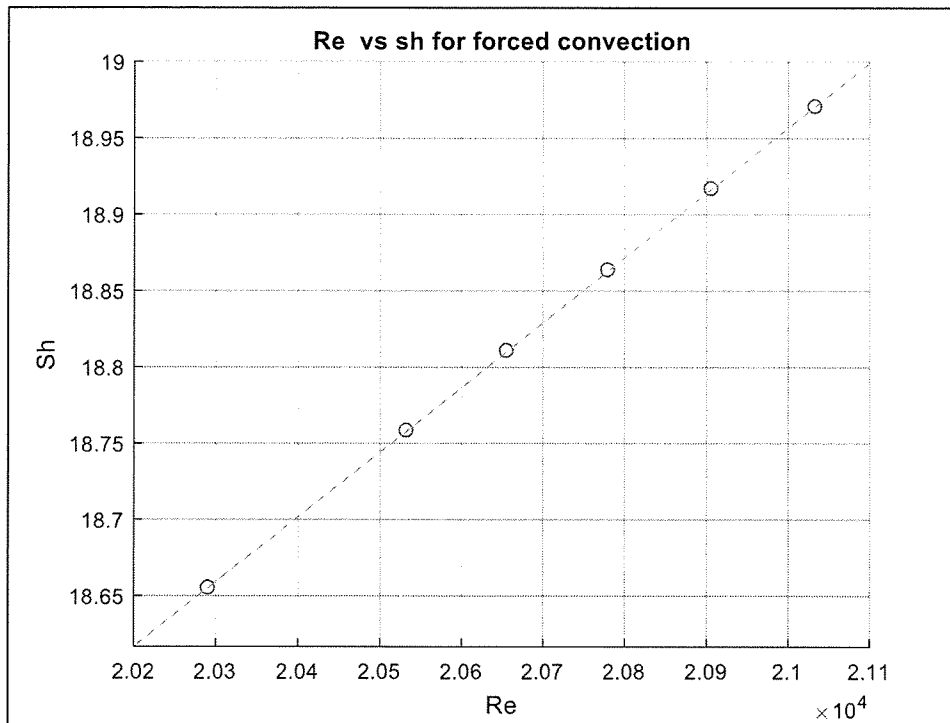
Figure A.6: Sherwood number for average forced convection mass transfer
coefficient as a function of Reynolds number

The effect of the mean flow velocity on the mass of water was presented as a function
of the Sherwood number and Reynolds number by Fontaine et al. (2013), as shown
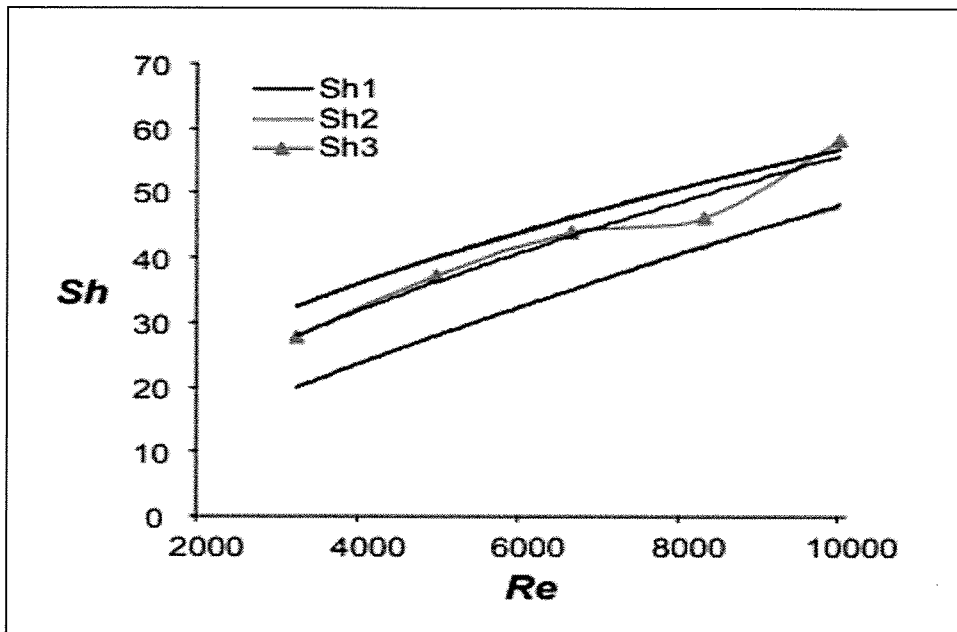in the Figure A.7.

Figure A.7: Effect of mean flow velocity on mass (Fontaine et al., 2013)

Figure A.8 describes the relation between the two parameters for a mixed-convection case. From the Figure, there is a linear relation between the two parameters in this situation. A maximum Sherwood number of 22.72 was obtained at a Reynolds number of 2.104×10^4.
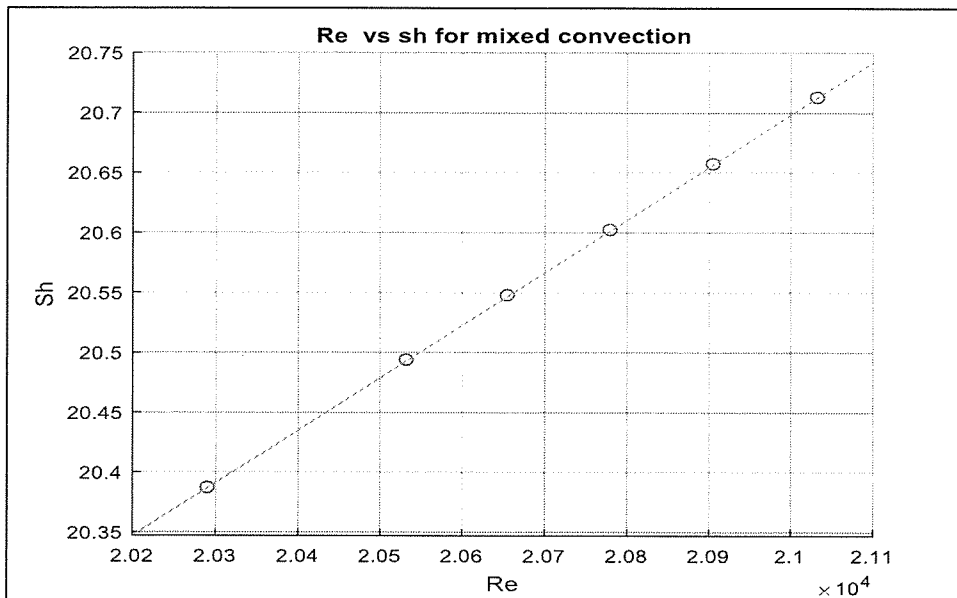
Figure A.8: Sherwood number for average mixed convection mass transfer coefficient as a function of Reynolds number

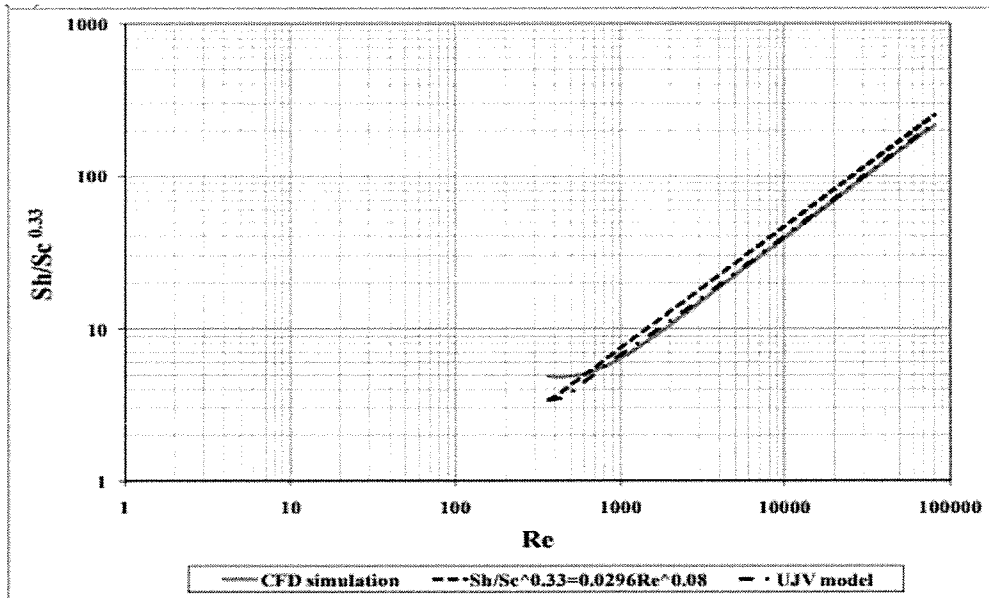Similar results were obtained by Saraireh (2012), as shown in Figure A.9.

Figure A.9: Change in Sherwood number as Reynolds number changed

The convection heat transfer from the flowing air was also governed by additional dimensionless parameters: the Grashof number and the Nusselt number.

For heat transfer at the surface within a fluid (which is humid air in this study), the Nusselt number is a dimensionless parameter that defines the ratio of convective to conductive heat transfer across the surface. It provides an indication of the heat transfer rate in convection. When the value of this parameter is high, then the flow is more active convection, with turbulent flow normally in the range of 100–1000.

The Grashof number is a dimensionless number calculated in fluid dynamics and heat transfer to indicate the value of the ratio of the buoyancy to the viscous force exerted on a fluid. It often increases in the study of cases containing natural convection and is analogous to the Reynolds number.

Because the force convection takes place because of fluid density changes owing to changes in temperature, the density often decreases because of a temperature increase, which causes the fluid to rise. The buoyancy force is responsible for this

113

motion of fluid. The main force that withstands the motion of the fluid is the viscous force, so the Grashof number is used to measure these opposing forces.

Figure A.10 presents the surface-averaged Nusselt number along the hot source, which is a function of the Grashof number. There is a linear relation between these two numbers. For lower values of the Grashof number, a slight increase in the average Nusselt number was observed owing to the low thermal gradients and predominance of the conduction regime. With increasing values of Gr, a brief increase in the Nusselt number was observed until it reached a maximum value of 2.224.
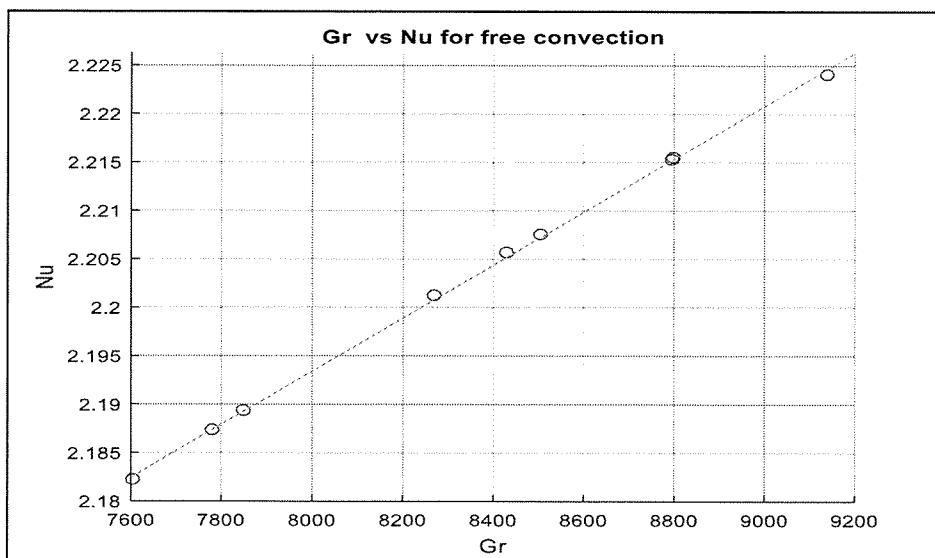

Figure A.10: Surface-averaged Nusselt number along hot source, which is a function of Grashof number

Figure A.11 shows the Nusselt number for forced convection as a function of the Reynolds number. From the Figure, there is a linear relation between the two dimensionless numbers, where the Nusselt number increases as Reynolds number increases. This means that the Nusselt number for turbulent flow is greater than that for laminar flow.
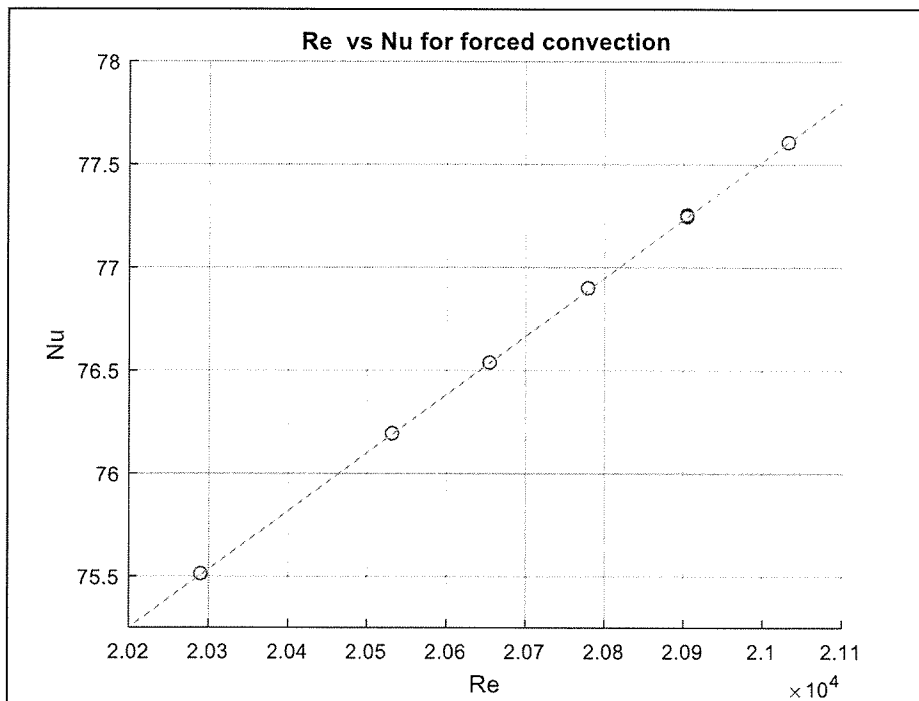
Figure A.11: Nusselt number for forced convection as a function of Reynolds number

Figure A.12 in the theoretical analysis shows the relation between the Nusselt number and Reynolds number for mixed convection. From the Figure, there is a linear relation between the two numbers. A maximum Nusselt number of 79.7 was observed at a Reynolds number of 2.104.
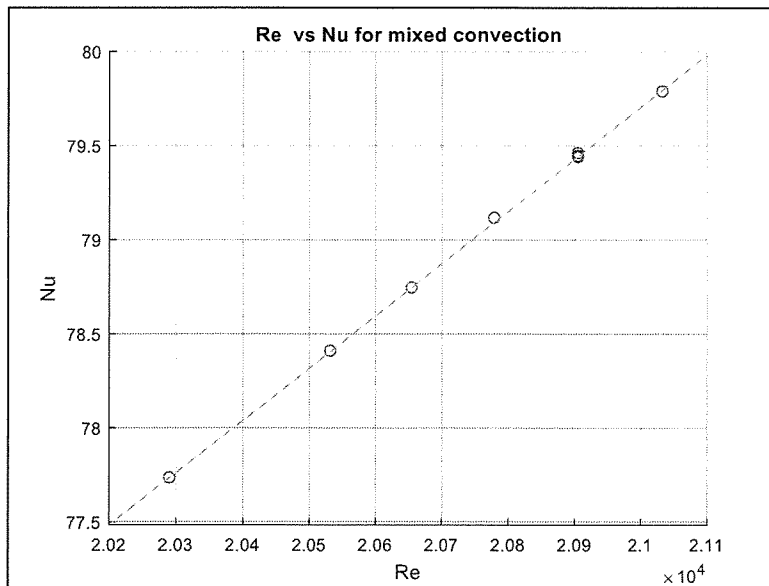
Figure A.12: Nusselt number as a function of Reynolds number for mixed convection

Similar results were obtained by Saraireh (2012) in his study, as shown in Figure A.13. These results were obtained by three different methods.
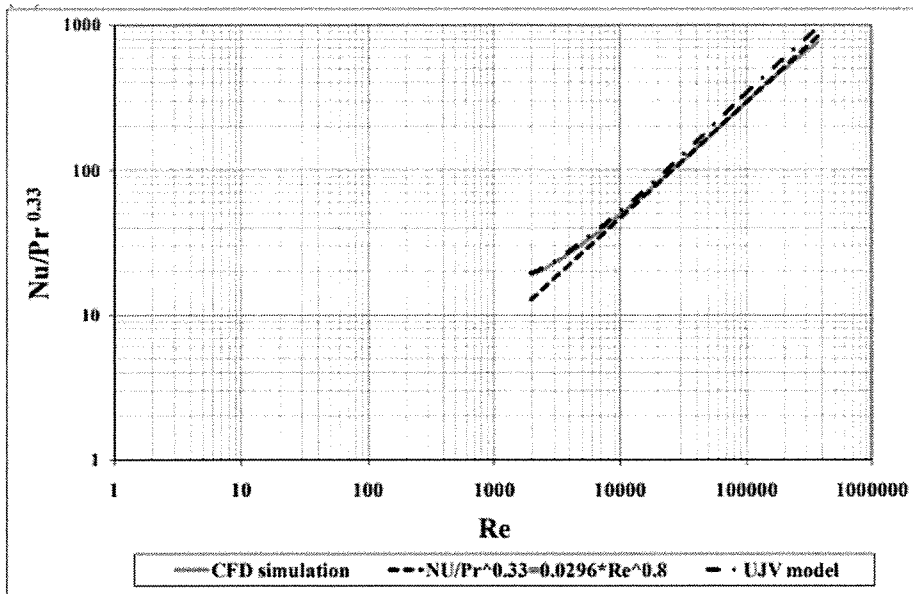
Figure A.13: Results obtained by Saraireh (2012) for two heat transfer cases

Latent heat is defined as follows: When latent heat is supplied to or removed from air, this results in a variation in its moisture content without changing the air temperature. The value of this heat refers to the amount required to convert the humid air from the vapor phase to the liquid phase. Figure A.14 shows the relation between the RH of air and the latent heat, it is clear that as the RH of air increased, more latent heat was required to convert the water vapor to liquid water. When the RH of air reached its maximum limit of 94%, the maximum latent heat required was approximately 33 W. This value decreased if the RH of air was reduced.
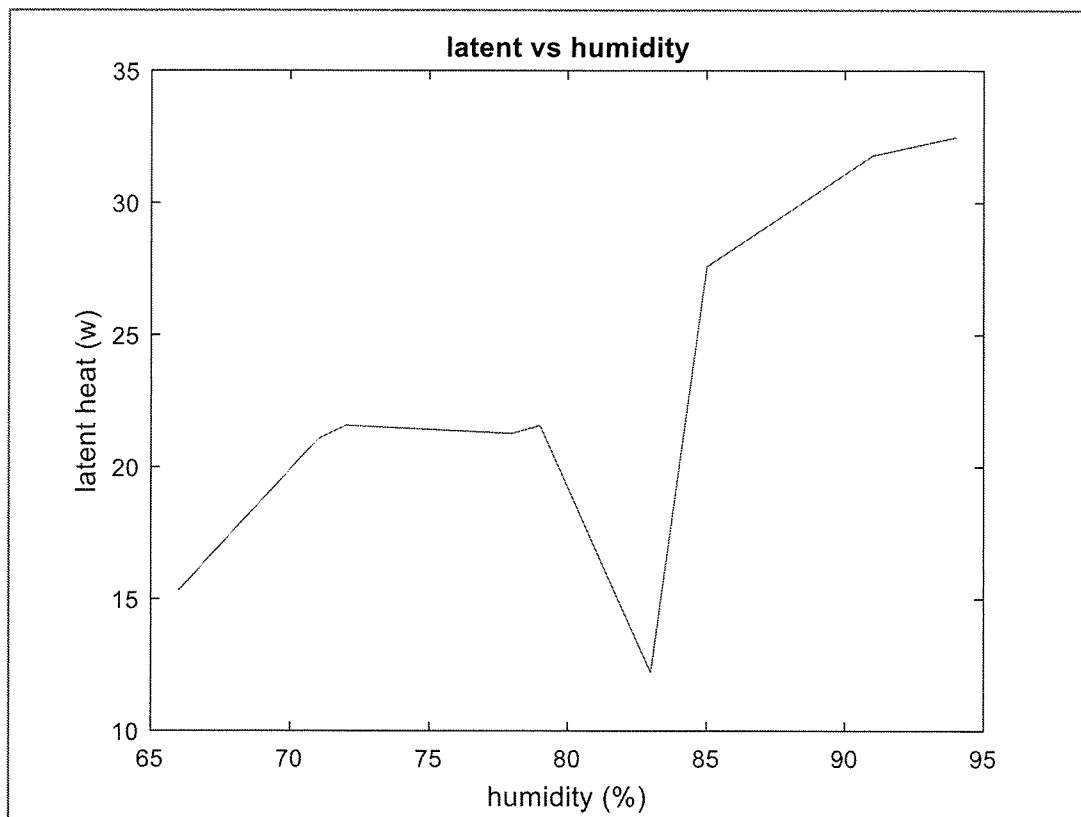
117

Figure A.14: Relation between RH of air and latent heat

The next plot shows the relation between the sensible heat and the RH of air. From the plot, the sensible energy (which refers to the amount of heat that changes the air temperature with no phase change) decreased as the RH of air increased. This is because the same amount of water vapor was still in the air, but at a higher temperature, its vapor pressure (which is related to the maximum amount of water that air at that temperature can hold) increased. Since the RH is the ratio of the actual partial pressure of the water vapor (which was kept the same throughout heating or cooling because the same amount of water vapor was present) to the vapor pressure at that temperature (which increased), this ratio and the RH both decreased.
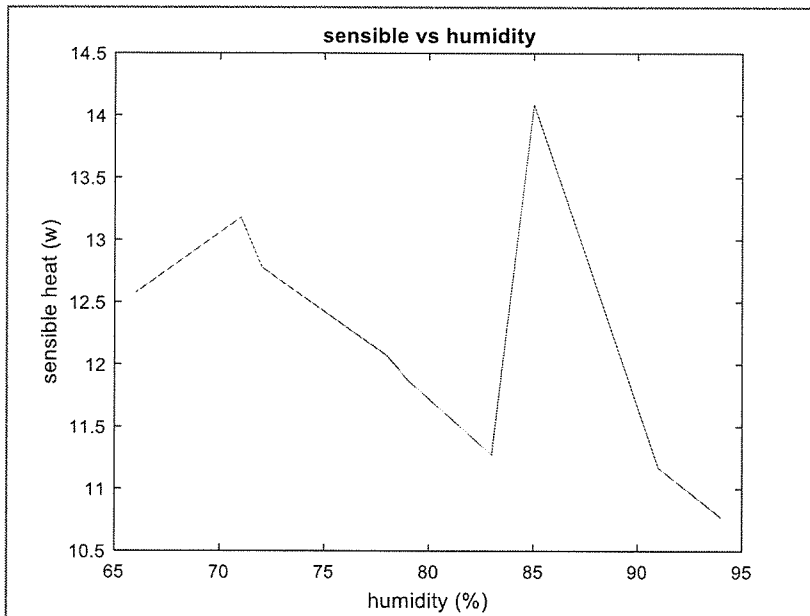
Figure A.15: Relation between RH and sensible heat

In this part of the discussion, additional plots were created to compare the results discussed above. Figure A.16 compares the relation between the Sherwood number and the Reynolds number for free and mixed convection, in both modes of convective heat transfer, there is a linear relation between the two dimensionless parameters but with different values. A higher Sherwood number was observed for the mixed convection mode with a maximum value of 22.72, while a lower value was observed for free convection with a maximum value of 1.742. Both maximum values were obtained at a Reynolds number of 2.104×10^4.
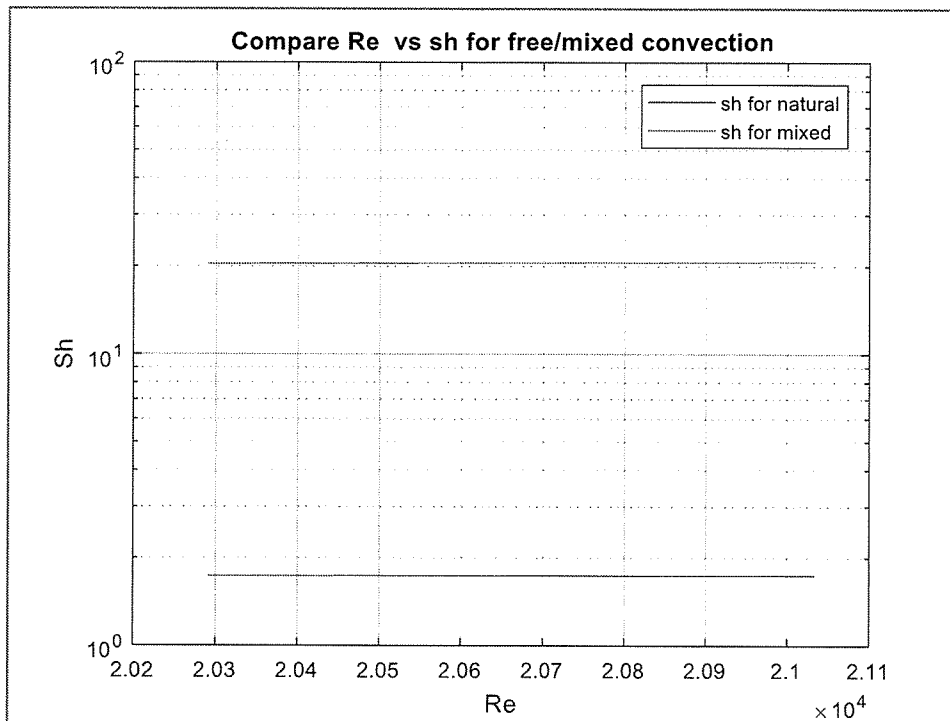
Figure A.16: Comparison between Sherwood number and Reynolds number for free and mixed convection

Figure A.17 compares the relation between the Nusselt number and the Reynolds number for natural and mixed convection. For mixed convection (indicated by a red line), the Nusselt number increased linearly as the Reynolds number increased. A maximum Nusselt number of 79.7 was observed at a Reynolds number of 2.104×10^4. Lower values were obtained for natural convection at the same Reynolds number.
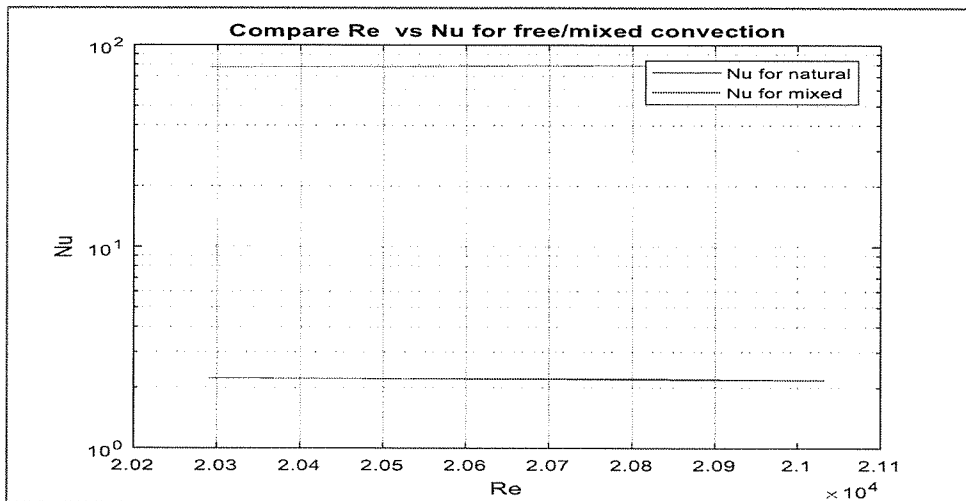
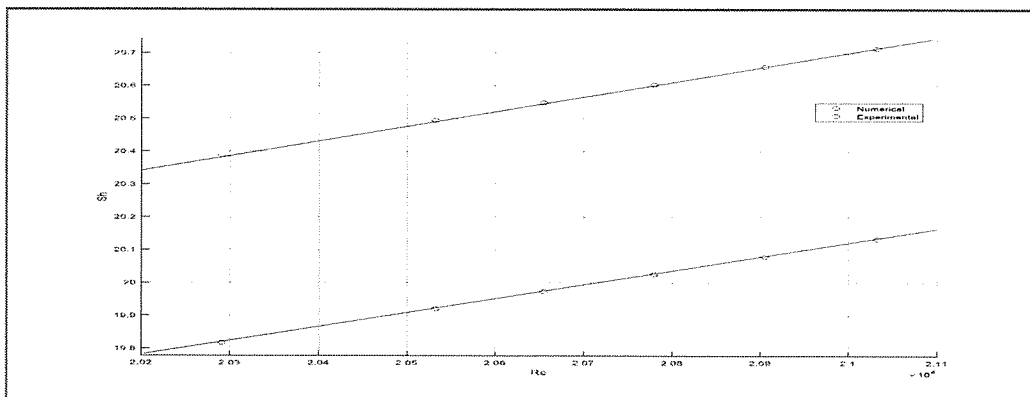Figure A.17: Comparison between Nusselt number and Reynolds number for free and mixed convection

Figure A.18: Comparison of experimental and numerical results of Sherwood number vs. Reynolds number

121

Appendix A   Appendix B: Numerical analyses

B.1: Materials selection

For the prepared model in SolidWorks software, a suitable material was required. For this purpose, Cambridge Engineering Selector (CES) software was used.

CES is a software package that was produced to help answer these questions. Developed over several years by Mike Ashby and David Cebon, CES is now being marketed by their company, Granta Design. The selector uses an extensive database of information and can be linked to a company's own database for specific applications. In addition, web links are provided to search other relevant sites. CES is a unique tool for the rational selection of engineering materials (metals, ceramics, polymers, and composites) and manufacturing processes (shaping, finishing, joining, and surface treatment). The software is easy to install and use on a PC. It combines a database of materials and process properties with software tools to

Browse and search the information in the materials property database,

Create highly visual and interactive material property charts that enable the inspection and comparison of materials, and

Apply this information using a systematic materials selection method to identify and rank the best materials for a particular engineering application.

Figure A.19 presents the first screen observed after opening the CES software. From this screen, the level-three advanced option was selected.

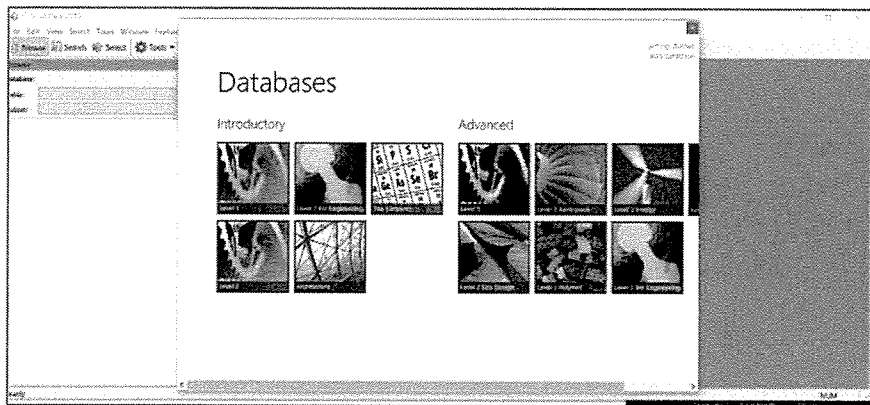Figure A.19: Select level three advanced

The details of the material selection are shown in Appendix B.1. The results of limiting the materials' thermal conductivity is graphically presented in Figure A.20. From the Figure, the material that combined the two properties of low price and high thermal conductivity was related to the aluminum family.
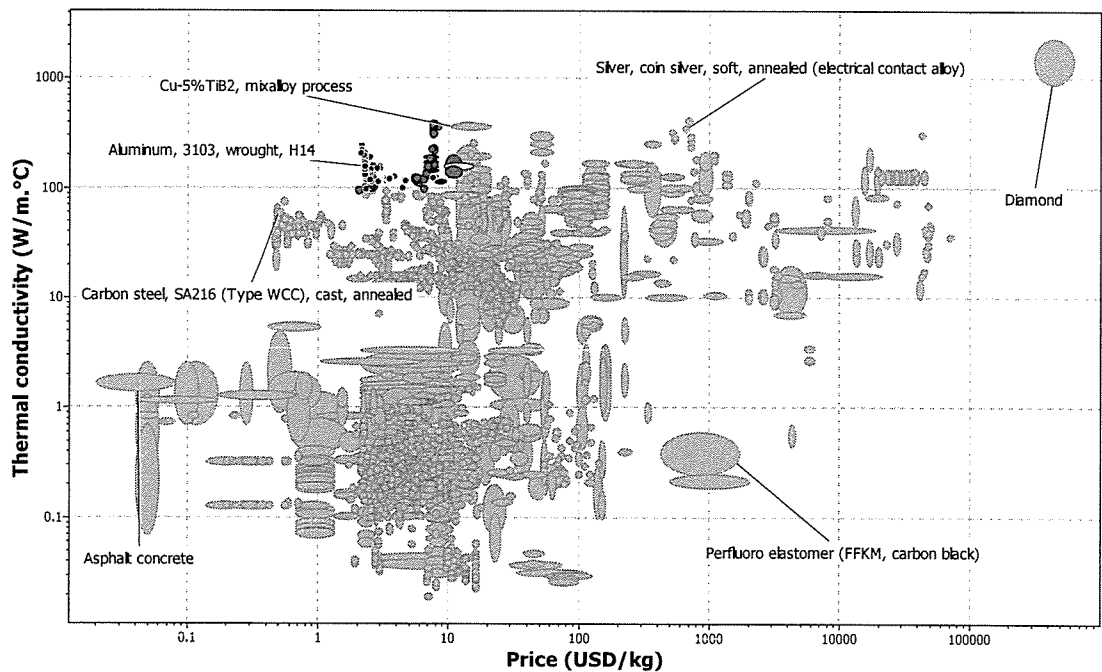

Figure A.20: Selection based on thermal conductivity

As previously mentioned, the remaining materials were aluminum-based. The above Figures show more than 10 materials related to this family, and in Figure A.21 shows the aluminum materials that have both low price and high thermal conductivity. Among these materials, the best material for the condensation model is aluminum, commercial purity, 1-0, wrought. The physical, chemical, mechanical, and thermal properties of this material are presented in Appendix B.2.
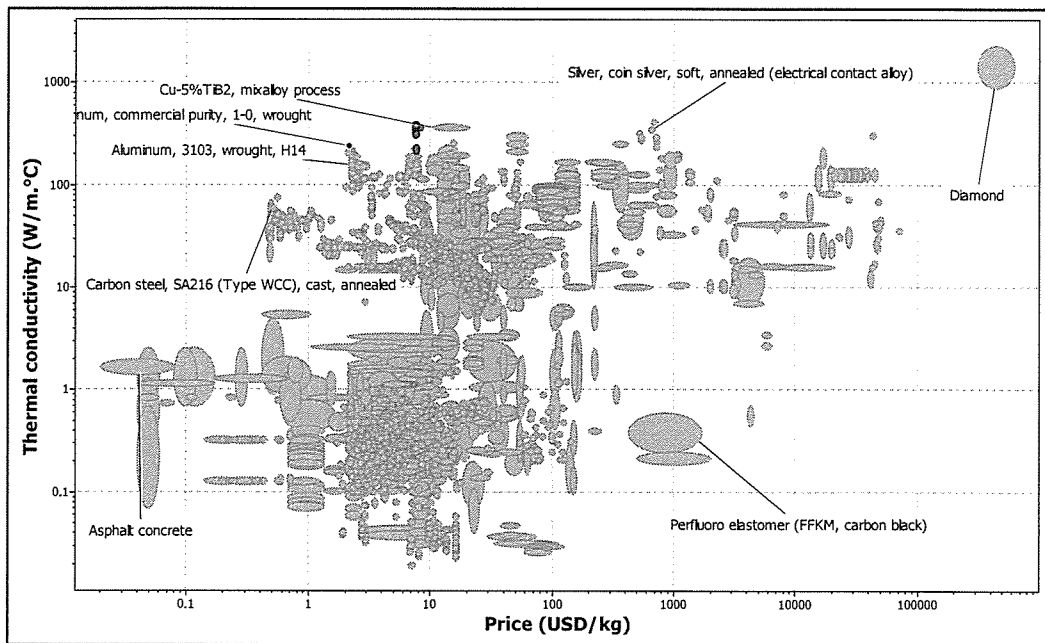
Figure A.21: Selection of aluminium, commercial purity, 1-0, wrought

The selected material of aluminum, commercial purity, 1-0, wrought was applied to the prepared model of humid air condensation when defining its properties so that the desired simulation could be applied.

After that, the type of material from which the model would be made was selected. As shown in Figure A.22, a search for the best material was conducted on all types of materials available in the CES material universe.
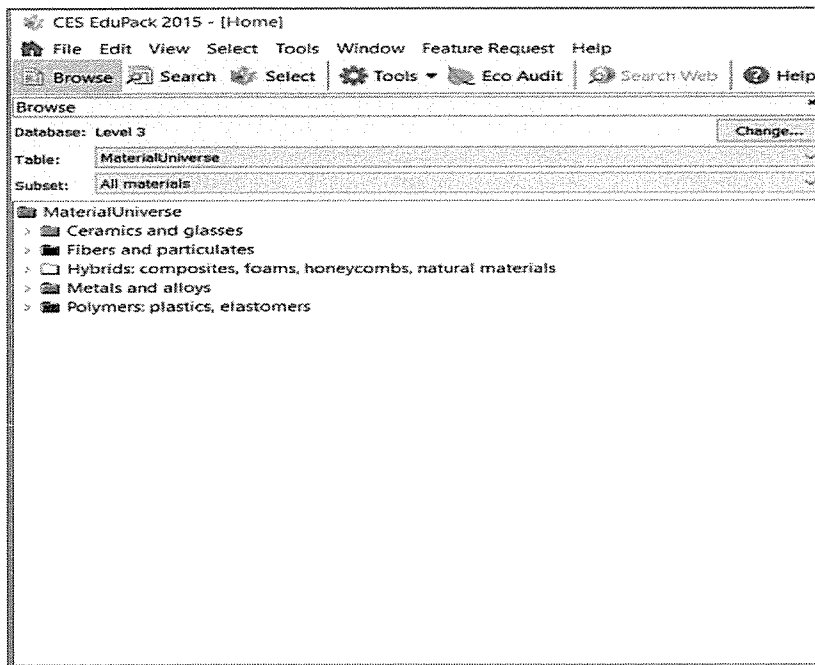
Figure A.22: Material universe selection

Different properties can be defined on the y-axis. The selection of one type of property depends on the type of analysis to be carried out. Because this study depends on the heat transfer mechanism, the thermal properties of the materials are the key factors. Figure A.23 shows the selection step for thermal properties in CES.
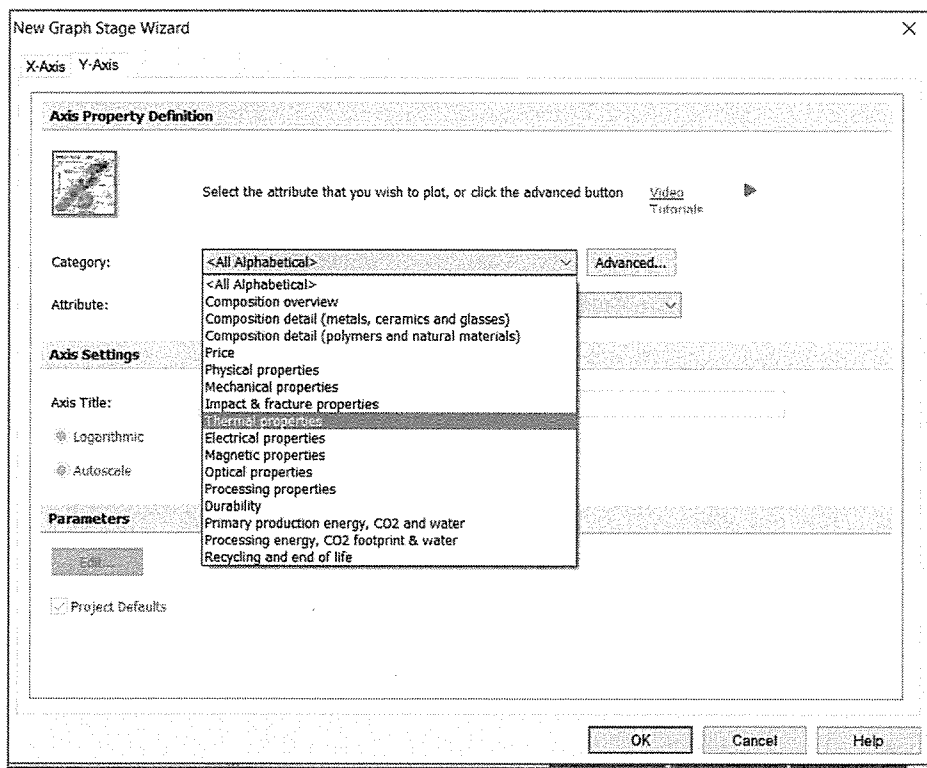
Figure A.23: Thermal properties selection

There was a wide range of thermal properties to be compared in this study. Figure A.24 shows the selection of thermal conductivity to be listed on the y-axis.
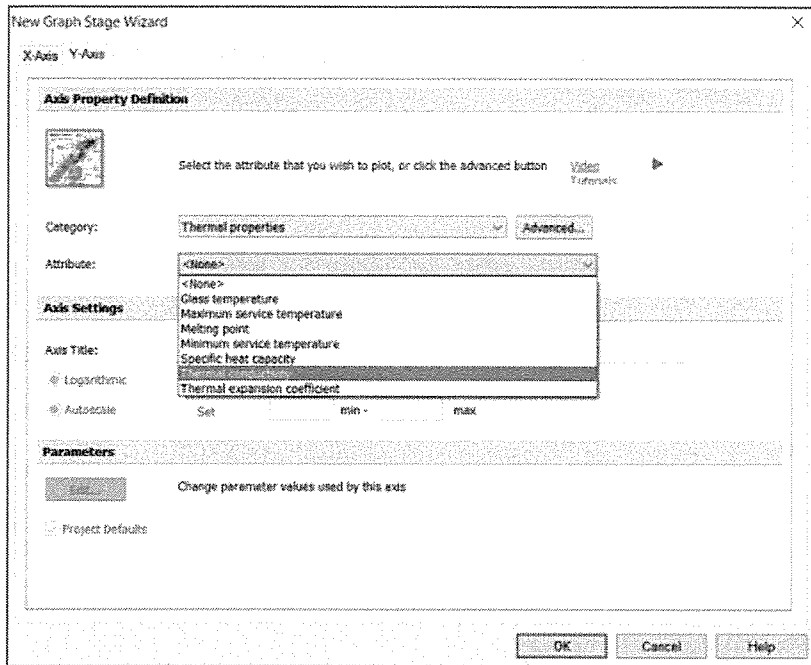
Figure A.24: Defining thermal conductivity on y-axis

After choosing OK, a plot was generated for the relation between the thermal conductivity and price for all materials available in the CES library. This plot is shown in Figure A.25. A wide range of materials is presented in this plot, some of which have very low thermal conductivity, while others have very high thermal conductivity. The selection of one material from this plot is somewhat difficult and required the setting of a limit on the selected properties of price and thermal conductivity to reduce the number of materials in the plot.
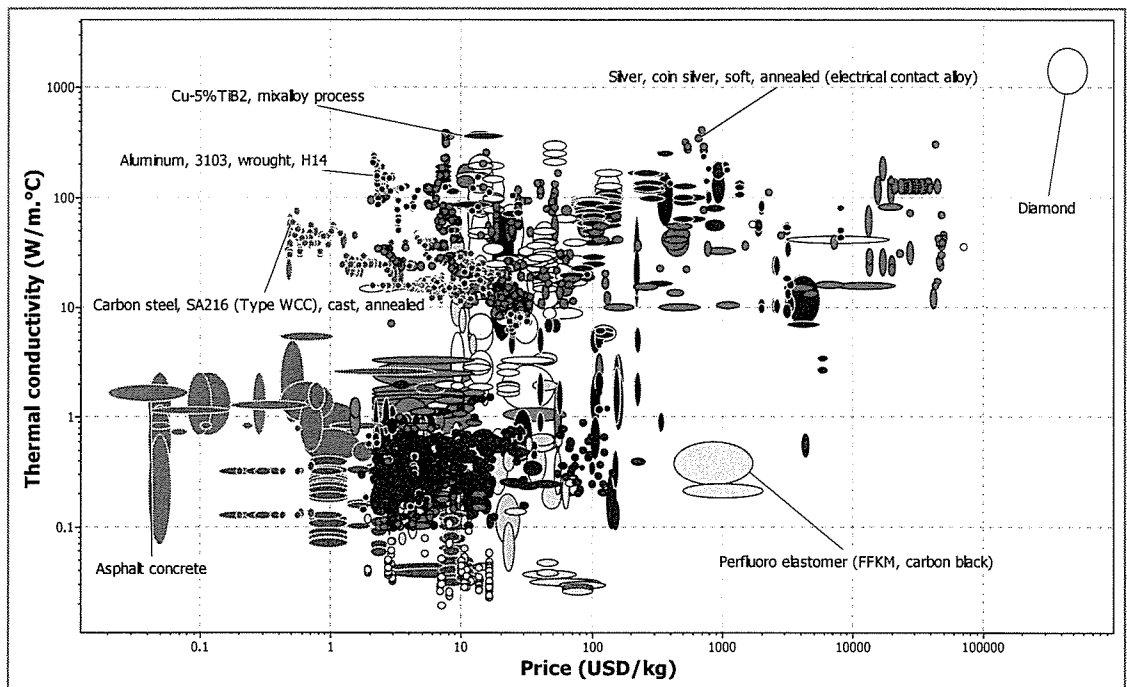
Figure A.25: Thermal conductivity vs. price for all materials in CES

The first property (price) was limited, as shown in Figure A.25. From the Figure, the best material for the model should have a maximum price of $10 USD per kilogram of material. This means that any material with a price of $10 USD/kg or lower is suitable.
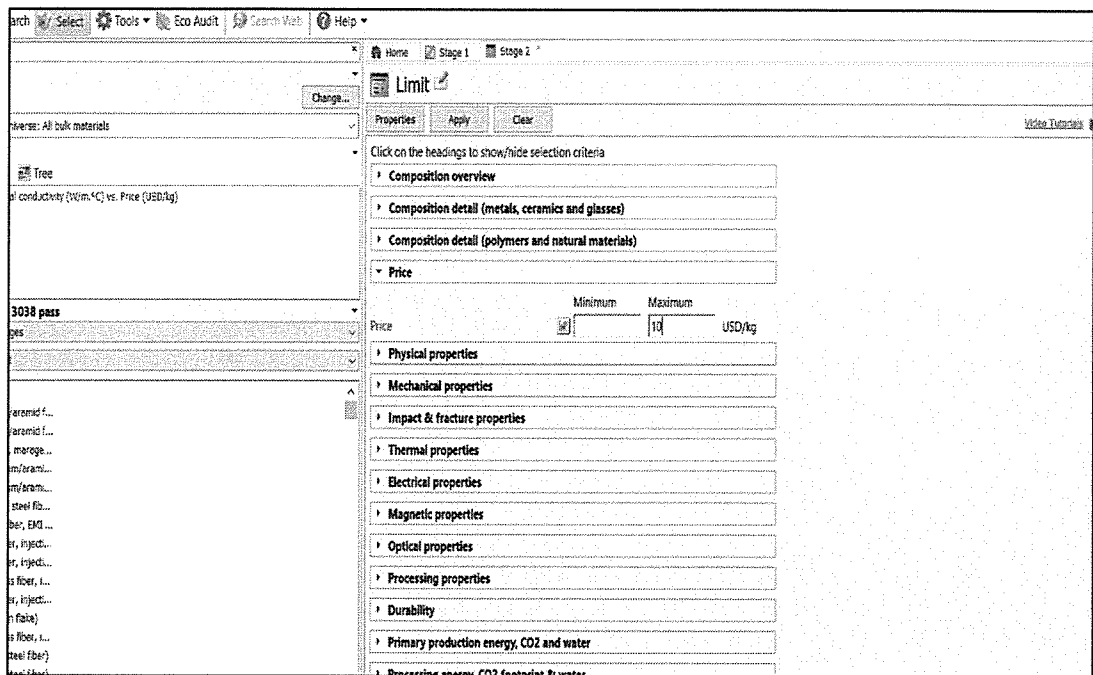
Figure A.26: Limiting material price

The results of limiting the price are presented graphically in Figure A.26. From the Figure, it is clear that there are a wide range of materials that have a price of $10 USD/kg or lower, such as aluminum (3103, wrought, H14), carbon steel (SA216, type WCC, cast, annealed), and asphalt concrete. To select one of these materials, an additional limit should be applied.
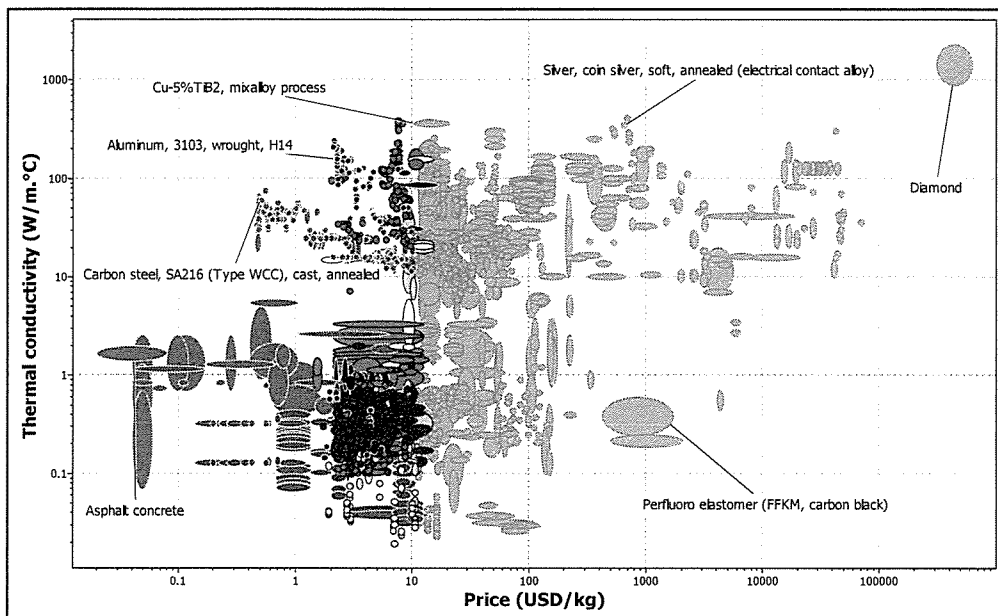
Figure A.27: Results of limiting materials price

The additional limit involved the thermal conductivity of these materials, where the best material for the prepared model should have a thermal conductivity greater than 100 W/m·°C. This limit is presented in Figure A.27.

Figure A.28: Limiting thermal conductivity of remaining materials

B.2: Selected material properties

Aluminum, commercial purity, 1-0, wrought

General information

Designation
1-0
Typical uses
Highest quality reflectors.

Composition overview

Compositional summary
Al100 / Other0.01

Material family	Metal (non-ferrous)
Base material	Al (Aluminum)

Composition detail (metals, ceramics and glasses)

Al (Aluminum)	100			%
Other	0	–	0.01	%

Price

Price	* 2	–	2.2	USD/kg

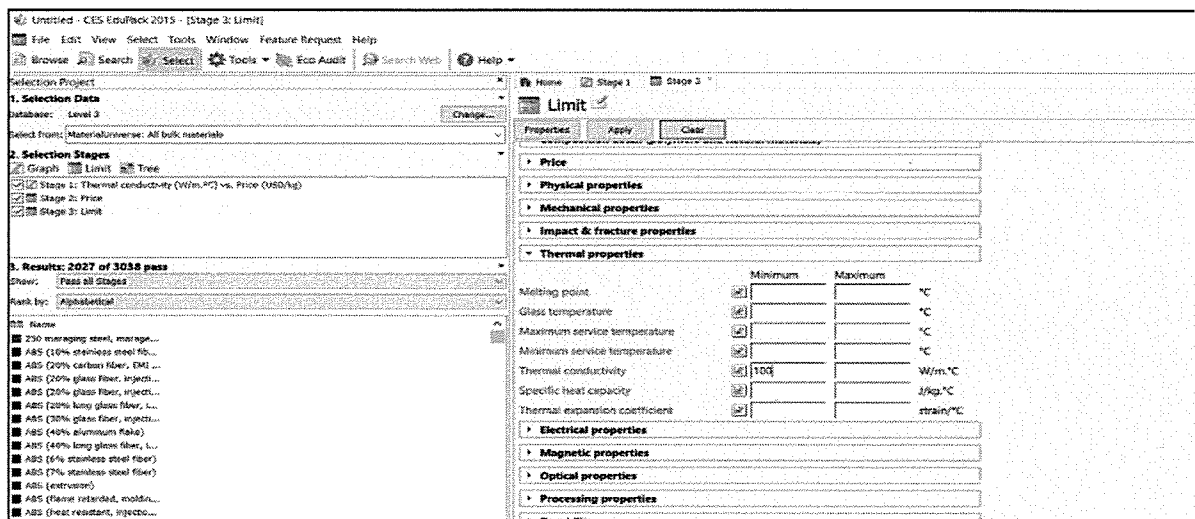## Physical properties

Density	2.67e3	–	2.73e3	kg/m^3

Mechanical properties

Young's modulus	6.9e10	–	7.2e10	Pa
Yield strength (elastic limit)	2.4e7	–	2.6e7	Pa
Tensile strength	5.5e7	–	6.1e7	Pa
Elongation	0.37	–	0.43	strain
Compressive strength	* 2.4e7	–	2.6e7	Pa
Flexural modulus	* 6.9e10	–	7.2e10	Pa
Flexural strength (modulus of rupture)	2.4e7	–	2.6e7	Pa
Shear modulus	2.5e10	–	2.7e10	Pa
Bulk modulus	6.2e10	–	8.4e10	Pa
Poisson's ratio	0.32	–	0.36	
Shape factor	42			
Hardness – Vickers	1.4e8	–	1.55e8	Pa
Fatigue strength at 10^7 cycles	* 2.65e7	–	2.87e7	Pa
Fatigue strength model (stress range)	* 1.72e7	–	2.03e7	Pa

Parameters: Stress Ratio = 0, Number of Cycles = 1e7cycles

Mechanical loss coefficient (tan delta)	* 1e-4	–	0.002	

Impact & fracture properties

Fracture toughness	* 3.2e7	–	3.5e7	Pa.m^0.5

Thermal properties

Melting point	645	–	675	°C
Maximum service temperature	80	–	100	°C
Minimum service temperature	-273			°C
Thermal conductivity	239	–	249	W/m.°C
Specific heat capacity	* 910	–	960	J/kg.
Thermal expansion coefficient	2.29e-5	–	2.41e-5	strain/°C
Latent heat of fusion	3.84e5	–	3.93e5	J/kg

Electrical properties

Electrical resistivity	2.6e-8	–	2.8e-8	ohm.m
Temperature dependence of resistivity	3.9	–	4.1	/°C
Galvanic potential	* -0.79	–	-0.71	V

Optical properties

Transparency	Opaque

Processing properties

Metal casting	Unsuitable
Metal cold forming	Excellent
Metal hot forming	Excellent
Metal press forming	Excellent
Metal deep drawing	Excellent

Durability

Water (fresh)	Excellent
Water (salt)	Acceptable
Weak acids	Excellent
Strong acids	Excellent
Weak alkalis	Acceptable
Strong alkalis	Unacceptable
Organic solvents	Excellent
Oxidation at 500C	Unacceptable
UV radiation (sunlight)	Excellent
Flammability	Non-flammable

Primary production energy, CO2 and water

Embodied energy, primary production	1.9e8	-	2.09e8	J/kg

Sources
183 MJ/kg (Institute for Prospective Technological Studies, 2005); 187 MJ/kg (Hekkert, 2000); 211 MJ/kg (Norgate, Jahanshahi, Rankin, 2007); 218 MJ/kg (Hammond and Jones, 2008)

CO2 footprint, primary production	12.3	-	13.6	kg/kg

Sources
12.8 kg/kg (Hammond and Jones, 2008); 13.1 kg/kg (Voet, van der and Oers, van, 2003)

Water usage	* 1.14	-	1.26	m^3/kg

Processing energy, CO2 footprint & water

Rough rolling, forging energy	* 8.71e5	-	9.63e5	J/kg
Rough rolling, forging CO2	* 0.0653	-	0.0722	kg/kg
Rough rolling, forging water	* 0.00192	-	0.00289	m^3/kg
Extrusion, foil rolling energy	* 1.46e6	-	1.61e6	J/kg
Extrusion, foil rolling CO2	* 0.109	-	0.121	kg/kg
Extrusion, foil rolling water	* 0.00217	-	0.00326	m^3/kg
Wire drawing energy	* 4.68e6	-	5.17e6	J/kg
Wire drawing CO2	* 0.351	-	0.388	kg/kg
Wire drawing water	* 0.00176	-	0.00265	m^3/kg
Metal powder forming energy	* 2.46e7	-	2.71e7	J/kg
Metal powder forming CO2	* 1.96	-	2.17	kg/kg
Metal powder forming water	* 0.0268	-	0.0402	m^3/kg
Vapourization energy	* 1.55e10	-	1.71e10	J/kg
Vapourization CO2	* 1.16e3	-	1.28e3	kg/kg
Vapourization water	* 6.46	-	9.69	m^3/kg
Coarse machining energy (per unit wt removed)	* 5.63e5	-	6.22e5	J/kg
Coarse machining CO2 (per unit wt removed)	* 0.0422	-	0.0467	kg/kg
Fine machining energy (per unit wt removed)	* 1.35e6	-	1.5e6	J/kg
Fine machining CO2 (per unit wt removed)	* 0.102	-	0.112	kg/kg
Grinding energy (per unit wt removed)	* 2.23e6	-	2.47e6	J/kg
Grinding CO2 (per unit wt removed)	* 0.167	-	0.185	kg/kg
Non-conventional machining energy (per unit wt removed)	* 1.55e8	-	1.71e8	J/kg
Non-conventional machining CO2 (per unit wt removed)	* 11.6	-	12.8	kg/kg

Recycling and end of life

Recycle	True			
Embodied energy, recycling	* 3.23e7	-	3.57e7	J/kg
CO2 footprint, recycling	* 2.54	-	2.8	kg/kg
Recycle fraction in current supply	52.3	-	57.8	%
Downcycle	True			

132

Appendix C: Psychrometric chart

ASHRAE PSYCHROMETRIC CHART NO. 1
NORMAL TEMPERATURE   SEA LEVEL
BAROMETRIC PRESSURE   101.325 kPa.

COPYRIGHT 1992
AMERICAN SOCIETY OF HEATING, REFRIGERATING AND AIR CONDITIONING ENGINEERS, INC.